

Disruption of large-scale neuronal activity patterns in Alzheimer's disease models

Claire Wu

A dissertation submitted in partial fulfillment
of the requirements for the degree of
Doctor of Philosophy
of
University College London.

Institute of Neurology
University College London

November 13, 2019

I, Claire Wu, confirm that the work presented in this thesis is my own. Where information has been derived from other sources, I confirm that this has been indicated in the work.

Abstract

The overexpression and aggregation of tau is observed in a class of neurodegenerative diseases termed tauopathies. Individuals with tauopathy, and animal models of tauopathy, show a loss of behavioural and cognitive function, but the neural underpinnings of these symptoms are poorly understood. We investigated changes in neural function in the Tg4510 model of tauopathy in primary visual cortex (V1) - an area where the relationship between stimulus features, single unit responses, and the circuits and mechanisms underlying them, is relatively well characterised - and in CA1.

We conducted chronic awake head-fixed recordings in V1 of 5-6.5 month old mice, presenting a variety of visual stimuli, including drifting grating stimuli that varied across feature dimensions such as orientation, contrast, or size. Mice were also trained to run in a virtual reality environment, either closed loop, open loop (playback) or in the dark.

Tau+ and Tau- mice displayed clear differences in the oscillatory local field potentials in V1 and CA1, notably Tau+ mice showed a large decrease in high frequency power as well as minor changes in stimulus-evoked power and power in relation to running speed. Single unit responses in V1 of Tau+ mice were also altered. Tau+ mice showed greater orientation selectivity and suppression following orientation adaptation, and improved contrast tuning, but worse selectivity in response to sparse noise stimuli. Responses to other stimulus features, such as spatial frequency and size, were unchanged between the two groups.

In conclusion, tauopathy in the Tg4510 mouse shows clear effects on information processing in the visual cortex and in CA1. This was not through a non-

selective decrease in responsiveness, but instead enhanced some types of processing, such as orientation selectivity, while disrupting others such as responses to sparse noise. These selective effects on neural function may reflect selective patterns of tauopathy on different cell classes or brain areas.

Impact statement

Alzheimer's disease is a brain disorder that affects a huge number of people worldwide. Patients with Alzheimer's disease show changes in behaviour such as forgetting their family's names and faces, forgetting how to get to familiar places or getting lost going to the shops or on their way home. In post-mortem examinations of the brains of people with Alzheimer's disease, the brain is vastly reduced in size and accumulation of two specific proteins, tau and amyloid- β , can be seen.

Alzheimer's disease can be modelled in mice by genetically manipulating mice to accumulate the same tau and amyloid- β proteins that accumulate in Alzheimer's disease patients.

In my project, I show how information processing in the brain changes in a mouse model of Alzheimer's disease, at a stage where tau protein is beginning to accumulate, but the brain has not yet shrunk in size. I observe some disruptions of information processing, but also some enhancements where certain functions of specific brain areas actually improve.

This research can be used in two important ways. First, the profile of changes I have observed in this mouse can be used as a marker for drug development, where drugs can be tested on whether they reverse this profile of changes to normal function or not. Secondly, as my findings are from an early stage of pathology, it might be possible in the future to use this profile of changes as a diagnostic marker in patients. This would allow researchers and doctors to identify Alzheimer's disease before cognitive symptoms such as memory loss are detected, and to treat the condition earlier.

Acknowledgements

I could not have completed this thesis without the help of so many people. The greatest thanks must of course go to my three supervisors, Aman Saleem, Kenneth Harris and Keith Phillips, who have provided constant guidance and reassurance throughout this project.

There have also been many people who have helped me at various points in my research. Special thanks goes to Tony Blockeel, not only performed all the surgeries for my head-fixed mice but also carried out all the unblinding protocols while I was conducting blinded analyses. Thank you also to Sam Solomon, Amalia Papanikolaou, Nick Steinmetz, Marius Pachitariu, Julien Fournier, Louisa Appel, Shahram Shahabi for help with analysis, mouse handling and all the other small things that need to get done for a project like this to succeed. I must also thank the Lilly animal facility staff for taking charge of dosing my mice with doxycycline so that I remained blinded to mouse group identity during the course of my experiments.

I am also deeply grateful to the MRC for funding this work, and to Eli Lilly for not only supplying funding but also all the mice and experimental equipment (from automated T-mazes to probes to a completely new virtual reality rig) I used in the course of my research.

Contents

1	Introduction	14
1.1	A brief overview of Alzheimer's disease	14
1.1.1	$A\beta$ pathology	15
1.1.2	Tau pathology	17
1.1.3	Risk factors for Alzheimer's disease	18
1.1.4	Modelling Alzheimer's disease using transgenic mice	19
1.1.5	The J20 mouse	23
1.1.6	The Tg4510 mouse	24
1.2	Changes in neural activity in Alzheimer's disease	25
1.2.1	Changes in field potential and synchrony	25
1.2.2	Changes in the spiking activity of single neurons	28
1.3	Brain areas of interest	30
1.3.1	Hippocampus	30
1.3.2	Primary visual cortex	32
1.4	Experimental paradigms	34
1.4.1	Delayed alternation T maze	34
1.4.2	Rodent virtual reality	37
1.5	Outline of thesis	38
2	Comparing a tau and amyloid model of Alzheimer's disease	40
2.1	Introduction	40
2.1.1	LFP in T maze	40
2.1.2	Aims and hypotheses	40

2.2	Methods	41
2.2.1	Surgery	42
2.2.2	Behaviour	43
2.2.3	Recording	44
2.3	Results	45
2.3.1	Behaviour	45
2.3.2	Power spectra and other LFP analyses	50
2.4	Comparative data from Tg4510 mice	51
2.5	Summary and choice of model	54
3	Experimental protocol and methods	56
3.1	Dox assignment	56
3.2	Surgery	59
3.3	Recording	59
3.4	Visual protocols	61
3.5	VR protocols	62
3.6	Histology and tau burden confirmation	65
4	Effects of tauopathy on local field potential activity	66
4.1	Introduction	66
4.1.1	LFP power spectrum changes in Tg4510 mice	66
4.1.2	V1 gamma	67
4.1.3	CA1 theta	67
4.2	Methods	68
4.2.1	Preprocessing	68
4.2.2	Analysis methods	73
4.3	Results: Power spectra differences in Tg4510	74
4.3.1	Basic differences in power spectra	75
4.3.2	Relationship between power and speed for V1 narrowband gamma and CA1 theta	76
4.3.3	Power changes over time	82

4.4	Results: Stimulus evoked potentials	82
4.4.1	ERP to a full screen flash stimulus	82
4.4.2	Stimulus-triggered power changes	84
4.5	Discussion	89
4.5.1	Power spectra changes in closed loop VR in Tau+ mice	89
4.5.2	Speed/power relationships in closed loop, open loop and in the dark	90
4.5.3	Power spectra at different ages	91
4.5.4	Changes in stimulus-evoked V1 narrowband gamma	92
4.6	Summary and conclusions	93
5	Effect of tauopathy on receptive field properties of V1	95
5.1	Introduction	95
5.1.1	Feature tuning and underlying mechanisms in primary vi- sual cortex	95
5.1.2	What is known about information processing by single units in the Tg4510 mouse	97
5.2	Methods	98
5.2.1	Spike sorting	98
5.2.2	Mean firing rates	98
5.2.3	Modelling tuning curves	99
5.3	Results	104
5.3.1	Mean firing rates	104
5.3.2	Spatial receptive fields	106
5.3.3	Orientation	108
5.3.4	Orientation adaptation	111
5.3.5	Contrast	115
5.3.6	Size	118
5.3.7	Spatial frequency	120
5.4	Discussion	120
5.4.1	Firing rate reduction in Tau+ mice	120

5.4.2	Deficits in response to sparse noise in Tau+ mice	123
5.4.3	Normal size tuning in Tau+ mice	124
5.4.4	Contrast enhancement in Tau+ mice	125
5.4.5	Orientation selectivity enhancement in Tau+ mice	126
5.4.6	Enhanced orientation adaptation effects in Tau+ mice	127
5.5	Summary and conclusions	128
6	General Conclusions	130
6.1	Selecting the Tg4510 mouse	130
6.2	Changes in the local field potential at an early stage of tauopathy . .	131
6.3	Changes in V1 population feature tuning at an early stage of tauopathy	132
6.4	Application of this project towards Alzheimer's disease	133
6.5	Conclusion	136
	Bibliography	138

List of Figures

2.1	Performance on the T maze by age in the single delay paradigm . . .	46
2.2	T maze performance in the variable delay paradigm.	48
2.3	Behaviour by training day in the single delay paradigm.	49
2.4	J20 results on the single delay alternating T-maze task	52
2.5	Tg4510 results on the single delay alternating T-maze task	53
3.1	Overview of experimental schedule and recording protocols	57
3.2	Dox and Non-Dox group assignment	58
3.3	Confirmation of histology and electrode placement	60
4.1	Identification of L4 in V1 and cell layer in CA1	69
4.2	Tau+ mice show differences in power across multiple frequency bands	77
4.3	Power spectra at different running speeds in closed loop condition .	79
4.4	CA1 theta and V1 narrowband gamma relationships with mouse running speed in closed loop, open loop and dark conditions	81
4.5	Tau+ and Tau- groups have similar changes in power due to age . .	83
4.6	VEP amplitude is elevated in CA1 of Tau+ mice	84
4.7	Tau+ mice do not show a decrease in narrowband gamma power with increasing contrast	87
4.8	Size evoked narrowband gamma in V1	88
5.1	Tau+ mice have reduced firing rates before and during stimulus pre- sentation	105
5.2	Tau+ mice have noisier spatial receptive fields	109
5.3	Dynamic range of firing during sparse noise is reduced in Tau+ mice	110

5.4	V1 populations in Tau+ mice are more well tuned for orientation . .	112
5.5	Orientation tuning is enhanced during adaptation in Tau+ mice . . .	114
5.6	Tau+ mice show greater suppression due to adaptation than Tau- mice	116
5.7	Contrast tuning is enhanced in Tau+ mice	117
5.8	Size tuning is not changed in Tau+ mice	119
5.9	Spatial frequency tuning is not changed in Tau+ mice	121

List of Tables

3.1	Details of all drifting grating visual protocols	63
4.1	R^2 values for linear fits	89

Chapter 1

Introduction

1.1 A brief overview of Alzheimer's disease

Alzheimer's disease (AD) is a neurodegenerative disease characterised by amyloid-beta ($A\beta$) and tau pathology (Braak and Braak, 1991) and behavioural symptoms including memory loss, disorientation and confusion (McKhann et al., 2011). It is also the most common form of dementia (Barker et al., 2002). The increasing incidence of Alzheimer's disease due to ageing populations presents a number of pressing problems: as well as being a significant economic burden in the form of long-term healthcare and caregiver costs, AD also has a significant personal and emotional impact on the friends and families of patients as well as the patients themselves (Alzheimer's Association, 2015). There are also currently no disease-modifying treatments for AD, and until treatments which either halt or drastically slow neurodegenerative pathology in AD are developed, the detrimental societal impact of AD will continue.

Understanding how pathology relates to changes in behaviour in Alzheimer's disease is the ultimate motivation for my project. I address this by looking at the smaller question of what changes in information processing by neural populations in transgenic mouse models of AD, at an early stage of pathology. While behavioural symptoms are used to make a diagnosis of AD during a patient's life, the presence of amyloid plaques and neurofibrillary tangles (NFT) in the post-mortem brain is the definitive criterion for diagnosis (The National Institute on Aging and Reagan

Institute Working Group on Diagnostic Criteria for the Neuropathological Assessment of Alzheimer's Disease, 1997; Braak and Braak, 1991). $A\beta$ and tau pathology also precede behavioural symptoms in Alzheimer's disease by many years, although pathology is usually not detected in the pre-clinical stage due to the lack of clear behavioural changes (Jack et al., 2010, 2013). Furthermore, the presence of tau and $A\beta$ not only differentiates patients with Alzheimer's disease from unaffected controls, but also indicates patients with mild cognitive impairment (MCI) that will go on to develop Alzheimer's disease, from patients with MCI who do not develop Alzheimer's and remain at a stable level of impairment (Olsson et al., 2016).

In the following sections, I describe the two main types of pathology observed in Alzheimer's disease, $A\beta$ and tau pathology. I will also discuss risk factors for Alzheimer's disease and summarise the use of mouse models in understanding Alzheimer's disease. I also describe the mouse models (J20 and Tg4510) of Alzheimer's disease that I have used in my project.

1.1.1 $A\beta$ pathology

Amyloid plaques are aggregated forms of amyloid- β , which is formed when the amyloid precursor protein (APP) is cleaved by the enzymes β -secretase and γ -secretase (Hardy and Selkoe, 2002). APP is a large protein which is usually broken down by α -secretase and γ -secretase into smaller proteins which do not have any toxic effects in the brain. However when β -secretase breaks down APP instead of α -secretase and the remaining chunk is further processed by γ -secretase, amyloid- β is formed (O'Brien and Wong, 2011). For many years, the 'amyloid hypothesis' has been the most popular explanation of how Alzheimer's disease arises (Hardy and Selkoe, 2002). Briefly, the amyloid hypothesis states that the accumulation of amyloid- β is the primary cause of Alzheimer's disease, and other changes such as tau accumulation and synaptic changes are later consequences of amyloid- β accumulating in the brain.

The strongest argument for the amyloid hypothesis is that the vast majority of genetic mutations that predispose people to Alzheimer's disease affect the breakdown of APP into the amyloid- β form (Bekris et al., 2010). In early studies of

Alzheimer's disease, it was found that people with Down's syndrome always go on to develop Alzheimer's disease (Olson and Shaw, 1969). Down's syndrome patients have an extra copy of chromosome 21 - which is also the location of the genes encoding for APP (Kang et al., 1987). Studies of genetic mutations responsible for familial autosomal dominant Alzheimer's disease, where patients who have the mutation inevitably develop Alzheimer's, also showed that the mutations responsible were all involved in the processing of APP (Bekris et al., 2010). For example, the 'Swedish' mutation, identified in two Swedish families suffering from Alzheimer's disease, increases production of amyloid- β (Mullan et al., 1992; Citron et al., 1992), and the 'Indiana' mutation, identified by a team working at Indiana University, increases the ratio of A- β 42 - the form that aggregates and is associated with toxic effects in the brain - compared to A- β 40, the normal product of APP breakdown that does not have toxic effects (Murrell et al., 1991; Tamaoka et al., 1994). Changes in genes that are not directly in the region coding for APP can also lead to Alzheimer's disease. For example, mutations in genes that are responsible for producing the proteins presenilin 1 and presenilin 2, which affect how γ -secretase cleaves APP, also cause familial Alzheimer's disease (Scheuner et al., 1996).

As well as being involved in familial AD, amyloid- β processing has also been linked to sporadic AD through genetic studies. In sporadic AD, there is no one clear genetic mutation that inevitably leads to the disease, as in familial AD, but instead there are a variety of risk factors that make it more likely for the patient to develop AD and it is not possible to identify a single cause of the disease onset. Most notably, the type 4 allele of apolipoprotein E (ApoE- ϵ 4) has been identified as a major risk factor for AD (Strittmatter et al., 1993), with changes in neural activity and navigational behaviour evident in ApoE- ϵ 4 carriers many decades before the typical age for disease onset (Kunz et al., 2015b). It is unclear how exactly the ApoE- ϵ 4 allele contributes to AD but it appears to have an effect on the amount of amyloid in the brain. For example patients with AD that also have the ApoE- ϵ 4 allele have more amyloid plaques than patients who have AD but do not have the ApoE- ϵ 4 allele (Drzezga et al., 2009). People who carry the ApoE- ϵ 4 allele but do

not have AD also have higher amyloid-beta deposition compared to people who do not have the ApoE- ϵ 4 allele (Morris et al., 2010).

While the plaque form of amyloid- β has long been used as a diagnostic marker for AD, soluble forms are now thought to be more causally relevant for neurodegeneration than plaques (Haass and Selkoe, 2007). For example, acute administration of soluble amyloid- β isolated from human brain tissue impairs long term potentiation (LTP) in hippocampal slices, whereas application of amyloid plaques does not (Shankar et al., 2008). However, the exact causal role of amyloid- β in the neurodegenerative cascade is still unclear (e.g. Benilova et al., 2012). Furthermore, plaques cannot be dismissed as a causal contributor to neurodegeneration - for example, Busche et al. (2008) found using in vivo calcium imaging in an amyloid model of AD (APP23xPS45) that hyperactive neurons are only found close to amyloid plaques in frontal cortex.

Because of all the genetic work supporting the amyloid hypothesis as well as the effects of amyloid- β on the brain, it was used extensively as the basis for drug development for Alzheimer's disease. However, despite the huge amount of money and effort that has been invested in developing 'anti-amyloid' drugs, no treatment for Alzheimer's has been found. Even if amyloid- β is successfully cleared by the drug, cognitive symptoms do not improve. Therefore following the late-stage failures of many 'anti-amyloid' drugs, attention has now turned to other aspects of Alzheimer's disease in the search for an effective treatment (Mehta et al., 2017). In particular there is interest in the role of tau in Alzheimer's disease as well as trying to stop the disease process at an earlier timepoint rather than trying to clear amyloid- β from the brain once it has already accumulated.

1.1.2 Tau pathology

Tau is a protein found in the brain, and occurs in healthy brains as well as those affected by Alzheimer's disease. In the non-diseased brain, tau stabilises microtubules, contributing to axonal transport and neuronal stability. (Weingarten et al., 1975). In Alzheimer's disease, tau hyperphosphorylates - i.e. undergoes a change in shape, causing it to stop performing its microtubule binding function (Bramblett

et al., 1993), eventually accumulating into neurofibrillary tangles (NFT) (Grundke-Iqbal et al., 1986; Mondragón-Rodríguez et al., 2008). Tau accumulation leads to problems such as neuronal death and gross atrophy as well as changes in synaptic density and function (Frost et al., 2015; Hoover et al., 2010; Jackson et al., 2017). These tau-driven symptoms are also found in patients with Alzheimer's disease (Scheff et al., 2007). However, like research on A β there is a lack of clarity on what exactly the functional consequences are for tau pathology in the living brain. For example, Kuchibhotla et al. (2014) found that neurons in a tauopathy mouse model of Alzheimer's disease can have normal orientation and direction tuning, even when those neurons contain NFTs.

Tau pathology is not only present in Alzheimer's disease, but also occurs in other neurodegenerative diseases as well. In fact, genetic mutations leading to tau pathology do not result in Alzheimer's disease, but are found in frontotemporal dementia, in a variant known as FTDP-17 (Wszolek et al., 2006). FTDP patients show personality changes, parkinsonism and symptoms of cognitive decline as well as tau pathology.

Although changes in the tau gene do not cause Alzheimer's disease in the same way that gene mutations linked to amyloid-beta processing in familial AD do, tau clearly plays an important role in the disease. In addition to the gross atrophy and synaptic changes described above, tau burden has also been found to correlate with cognitive decline better than amyloid-beta levels, in both patients and mouse models (Bejanin et al., 2017; Huber et al., 2018; Giannakopoulos et al., 2003).

1.1.3 Risk factors for Alzheimer's disease

Recently, genome-wide association studies (GWAS) have identified additional risk factors for Alzheimer's disease. Genome-wide association studies allow researchers to look across the entire genome to identify any gene that is linked to a disease, without having any pre-specified genes of interest. Using GWAS, ApoE was confirmed as the gene with the greatest contribution to developing sporadic AD (Coon et al., 2007), and several other genes have also been identified that are associated with AD (Lambert et al., 2013). Although how exactly these genes confer susceptibility

to AD is not known, it is clear from these studies that even 'sporadic' Alzheimer's disease has an important genetic component. Future research on these genetic contributions to AD will hopefully help us to understand what exactly the key events and processes are that lead to full-blown AD.

1.1.4 Modelling Alzheimer's disease using transgenic mice

Transgenic mouse models have been used extensively in investigating AD, both in basic research and in drug development. There is no single model that encompasses all aspects of the disease, rather, there are a wide variety of models in use, each with its own profile of pathological, functional and behavioural changes. Alzforum lists over 150 AD mouse models in their disease model database. (<http://www.alzforum.org>).

Using mouse models allows researchers to isolate specific aspects of Alzheimer's disease for investigation - for example the effect of amyloid- β pathology on network activity in vivo - while being sure that there are no complications from other disease processes - for example tau pathology. Using mouse models also allows for the use of many methods which are not feasible or ethical in humans, such as sacrificing mice at different timepoints to look at pathology, or using invasive or chronic recording techniques on living mice. Thus, using mouse models allows us to understand the processes taking place in Alzheimer's disease in greater depth in a model where we can observe and control various parameters such as the amount of pathology, stage of the disease, etc.

The two major categories of mouse model for Alzheimer's disease are mice which show amyloid- β pathology, and mice which show tau pathology. In the following paragraphs I will provide a broad overview of the types of AD mouse models currently in use.

Most amyloid mouse models of Alzheimer's disease overexpress human amyloid precursor protein (hAPP). This is achieved by inserting mutations found in patients with familial AD, such as the Swedish and Indiana mutations described above, into mice through use of a promoter. The choice of promoter affects which brain areas show pathology and whether expression is restricted to neurons only or

occurs in different cell types as well (Hall and Roberson, 2012, see table 2). Expression levels are also determined by which mutations have been used in the model. Mucke et al. (2000) generated different hAPP mouse models using the same promoter together with either different familial AD mutations or wildtype hAPP, and compared amyloid- β levels and plaque loads across the different models. Not only did the amount of amyloid- β and plaque load differ depending on the mutations used, but the speed of progression (i.e. the age at which plaques appeared) was also different between mouse lines. Thus, promoter and mutations combine to produce different levels of expression, locations of expression and speeds of progression in each different mouse model.

hAPP mouse models also show cognitive deficits in Morris Water Maze tasks which get worse with the progression of pathology, and these deficits can generally be reversed by anti-amyloid treatments (Van Dam et al., 2003; Hartman et al., 2005). The Morris Water Maze is the most widely used test of spatial reference memory, but it may not be the most sensitive - a comprehensive review of studies in one hAPP mouse model, the Tg2576 mouse, by Stewart et al. (2011) found that a T-maze alternation task showed greater differences between Tg2576 mice and control mice than the Morris Water Maze task and a variety of other spatial reference memory tasks. Spatial reference memory tasks are the most common type of task used in assessing AD models as they provide a behavioural measure of hippocampal function, which is known to be reduced in AD patients.

Amyloid models are very useful mouse models in Alzheimer's disease research because they are generated using mutations actually found in human patients with Alzheimer's disease, and they develop amyloid plaques and soluble amyloid- β , just like patients. Like patients, they also have progressive changes in memory performance. However, there are important aspects of Alzheimer's disease that they do not show, particularly tau-related changes such as neurofibrillary tangles. Another worry is that because they are generated from mutations that are present in familial Alzheimer's disease, results from these mice might not be applicable to patients with sporadic Alzheimer's disease. Amyloid mouse models have been widely used

in drug development as well as basic research, but despite the discovery of many compounds which clear amyloid- β and reverse memory impairments in the mouse model, none of the mouse results have been able to translate into alleviating symptoms in human patients (Mehta et al., 2017). It is not clear whether this is due to general differences between humans and mice, or because these amyloid models in particular are not modelling some necessary, important aspects of the disease process.

Some interesting variations on hAPP mouse models are mice with additional mutations inserted. Presenilin mutations in mouse models, for example, appear to have an exacerbatory effect but do not do much on their own. Mice that only have the presenilin mutation, with no other familial AD mutations inserted, do not develop plaques and do not show any memory deficits (Huang et al., 2003). However, when another hAPP mutation is added to a presenilin mouse model, these mice go on to develop more amyloid plaques than mice that only have the hAPP mutation, and also show greater cognitive deficits in memory tasks (Savonenko et al., 2005). A presenilin model, the 5XFAD model, which also expresses five different familial AD mutations, is also one of the amyloid models that shows neuronal loss in addition to amyloid pathology (Oakley et al., 2006).

To try to create mice which follow the Alzheimer's disease process as closely as possible, hAPP models have also been developed which have tau mutations inserted in order to create models that have both amyloid and tau pathology, and show neuronal loss and other characteristics of Alzheimer's disease absent in purely hAPP models (e.g. Lewis et al., 2001; Oddo et al., 2003). In some of these mouse models, for example the TAPP mouse, tau levels are elevated compared to in mice that only have the tau mutation (Bolmont et al., 2007), suggesting that amyloid and tau may interact to produce more aggressive pathology together than they do on their own.

Since hAPP models based on familial AD do not develop tau pathology without further intervention, tau models of Alzheimer's disease have also been created that specifically show tau pathology without amyloid pathology, so that the effects and progression of tau pathology can be studied in isolation. While tau models

are not directly based on mutations present in AD patients, they show many aspects of Alzheimer's disease that are also found in patients such as neurofibrillary tangles, large-scale neuronal loss and brain atrophy, and synaptic changes (Ramsden et al., 2005; Jackson et al., 2017). The development of these separate amyloid and tau mouse models has allowed researchers to understand which symptoms of Alzheimer's disease are linked to tau pathology and which to amyloid- β pathology.

To generate tau pathology in mouse models, mutations found in patients with frontotemporal dementia are inserted - for example, the JNPL3 and Tg4510 mouse both express the P301L mutation, the most common mutation in frontotemporal dementia (Lewis et al., 2000; SantaCruz et al., 2005). In JNPL3 mice, expression of tau was tied to the mouse prion promoter6 (MoPrP), leading to tau expression in areas such as brainstem and spinal cord in addition to hippocampus and cortex. This led to severe motor deficits in the mice which make cognitive tests, which in mice are usually highly dependent on movement, hard to run and interpret (Lewis et al., 2000). In contrast the Tg4510 mouse uses a promoter which limits tau expression to forebrain areas and mice do not show severe motor deficits, so they are able to complete tasks such as the Morris Water Maze or T-maze tasks successfully, and any deficits in performance can be attributed to cognitive rather than movement factors.

Another interesting class of tau models are 'seeding' models, where instead of tau pathology being driven by expression through a promoter, tau extracts from another mouse model of tau or from human brains are injected into the brain of the mouse (Clavaguera et al., 2013, 2009). Tau pathology spreads from the original injection site to other areas transsynaptically, forming neurofibrillary tangles and leading to synaptic changes and neuronal loss (de Calignon et al., 2010; De Calignon et al., 2012; Liu et al., 2012). Because of the way in which tau spreads from the initial 'seed', these models can recapitulate the pattern of progression of tau pathology in Alzheimer's patients, whereas in tau models where pathology is driven by a promoter, onset and progression of tau pathology in different areas is not the same as in patients. In contrast, tau models using promoters are still useful for understanding how different levels of tau pathology affect the function of a brain area at various

stages of progression.

The mouse models I use in my project are the J20 mouse and the Tg4510 mouse. In this project, I wanted to understand how the processing capabilities of neural populations change in Alzheimer's disease, and so it made sense to start by understanding how one out of amyloid- β or tau affected information processing individually, rather than using a more complex mouse model expressing both where the effects of either type of pathology could not be clearly dissociated.

1.1.5 The J20 mouse

The J20 mouse, an amyloid model of Alzheimer's disease, has the Swedish and Indiana mutations inserted in the APP gene, and expression is driven by the platelet-derived growth factor β chain promoter, with human amyloid precursor protein present in cortical and subcortical brain regions, but with more expression in neocortex and hippocampus (Mucke et al., 2000). The J20 is an aggressive model, with amyloid pathology including both plaques and oligomers starting to appear by 5-6 months in hippocampus (Mucke et al., 2000; Shankar et al., 2009).

J20 mice show specific deficits in a variety of spatial memory tasks. They are impaired compared to controls in the Morris Water Maze (MWM) by 6 months (Palop et al., 2003), and are also impaired in the 'cheeseboard' task, another test of spatial reference memory (Karl et al., 2012). J20 mice are also impaired at a spatial reference version of the radial arm maze (Wright et al., 2013). In contrast, they do not show any deficits in other tests which do not assess spatial reference memory, such as the novel object recognition task, a Y-maze task assessing short-term memory, or fear conditioning tasks (Karl et al., 2012; Wright et al., 2013).

J20 mice also have well documented abnormalities in neural activity in vivo, namely epileptiform activity and reduced gamma activity in EEG, as well as changes in dentate gyrus and CA1 observed in hippocampal slice (Palop et al., 2007; Verret et al., 2012). However local field potentials (LFP) and unit activity have not yet been recorded in this model while the mouse is actively engaged in a task.

1.1.6 The Tg4510 mouse

The Tg4510 mouse is an aggressive model of tauopathy that expresses the P301L mutation form of human tau, and displays classic signs of tauopathy such as neurofibrillary tangles and neuronal loss (Ramsden et al., 2005). Expression is driven by a Ca^{2+} calmodulin kinase II (CamKII) promoter so that tau is present primarily in forebrain areas with very minimal expression in subcortical structures such as thalamus. Synaptic changes - both in spine turnover and synaptic density - have also been observed prior to large scale neuronal loss in the Tg4510 mouse (Jackson et al., 2017; Kopeikina et al., 2012).

The most useful feature of the Tg4510 mouse is that tau expression can be reliably 'turned off' (i.e. greatly reduced) at any time by administration of doxycycline, and doxycycline administration prevents further behavioural as well as pathological decline (SantaCruz et al., 2005; Blackmore et al., 2017). This allows Tg4510 mice that have been fed doxycycline and are no longer expressing tau (Dox mice) to be used as the control for Tg4510 mice that have not been fed doxycycline and are still expressing tau (Non-Dox mice), rather than wildtype littermate controls. By using Dox mice as controls in experiments using the Tg4510 mouse, genetic and developmental effects of tau expression that are unrelated to disease progression can be equated in the control and experimental group. This makes it easier to isolate the effects of disease-relevant tauopathy on neural function and other changes of interest.

The Tg4510 mouse shows deficits in spatial reference memory tasks such as the Morris Water Maze from an early age (Ramsden et al., 2005), which can be prevented with doxycycline administration to reduce tau expression (SantaCruz et al., 2005). Performance in other spatial tasks, such as an alternating T-maze task and spatial preference Y-maze tasks also correlate strongly with tau burden in this mouse model (Blackmore et al., 2017). The Tg4510 mouse is also prone to excessive locomotor activity and hyperactivity levels are strongly correlated with tau burden in both hippocampus and cortex, with more hyperactive mice also having a greater tau burden (Blackmore et al., 2017).

1.2 Changes in neural activity in Alzheimer's disease

Changes in neural activity have been observed in AD patients and people at risk for Alzheimer's disease (e.g. Uhlhaas and Singer, 2006; Polich et al., 1990; Kunz et al., 2015a) but the spatial resolution of non-invasive techniques limits the utility of patient data for understanding information processing in AD. Although work with AD models involving in vivo recording of neural activity in behaving animals is not quite as widespread as the use of other techniques such as slice electrophysiology, there are a few studies of interest that relate neural function to performance or pathology in mouse models of AD using either implanted electrodes or calcium imaging to record neural activity, which I describe in the following sections.

Neural activity is clearly disrupted by amyloid pathology, for example LTP and synaptic transmission are disrupted in many APP models (Selkoe, 2002) and the J20 mouse also has increased epileptiform activity and disrupted oscillatory activity, including coherence (Palop and Mucke, 2010; Busche et al., 2015).

No single change in neural activity has been identified as being characteristic of AD, but rather there are a range of changes, from population-wide co-ordination to single neuron activity, that have been reported in a variety of different mouse models. I will outline some of these findings below.

1.2.1 Changes in field potential and synchrony

The local field potential (LFP) is an electrical signal measured from the extracellular space around neurons, (Destexhe and Bedard, 2013). Any kind of electrical activity by neurons can contribute to the LFP signal, but the major component of the signal is the summation of synchronous post-synaptic activity from many neurons around the extracellular space sampled by the recording electrode (Buzsáki et al., 2012). Synchronous spiking activity can also contribute to the high-frequency components of the LFP signal. The key feature of these strongest and most easily identifiable changes - whether spike-driven or synaptic - in the LFP signal is that the activity is synchronous, so that many neurons are involved in generating the signal at one time. This makes the LFP signal an excellent measure of the activity of local populations of neurons. Changes in the LFP signal are also more translatable to

human research, as similar population signals can be measured using EEG, whereas multi-unit firing cannot be recorded from humans without invasive techniques. An excellent review of the components contributing to the LFP signal can be found in Buzsáki et al. (2012).

Perhaps the most important type of synchronous activity in the LFP signal are oscillations. Oscillations occur at a wide range of different frequencies in different brain areas (Colgin, 2016), and oscillatory activity can also be observed using EEG and MEG in humans (Uhlhaas and Singer, 2006). However, with these non-invasive techniques the signals cannot be localised as well as when implanted probes are used. In a very general sense, oscillations in the brain are often thought to be related to function because they dynamically co-ordinate large-scale population activity, and hence might represent the creation of functional populations on-the-fly through co-activation, enabling both local and inter-areal communication between distinct neural populations.

From what we know about changes in Alzheimer's disease, we should expect that Alzheimer's disease leads to changes in the local field potential. For example, synapse loss can be observed in AD patients as well as in patients with mild cognitive impairment (Scheff et al., 2007). Synapse loss is likely to result in a reduction of synchronous activity and oscillations in the LFP signal. In fact, there have been a few studies that suggest neural synchrony is altered in AD patients (Delbeuck et al., 2003; Uhlhaas and Singer, 2006). However, changes in the LFP signal are not limited to oscillatory activity alone. One of the more robust changes is that Alzheimer's patients show decreases in evoked potential in response to an auditory stimulus (e.g. Polich et al., 1990; Clair et al., 1985; Buchwald et al., 1989). This also suggests that there is a decrease in co-ordinated population activity in Alzheimer's patients.

Patients with Alzheimer's disease also display very specific types of changes in functional synchrony and connectivity. Initial AD pathology occurs in the entorhinal cortex, an area that acts as the gateway between the hippocampus and cortex (e.g. see Fig. 2 in Braak and Braak, 1996), which has led to the idea that AD could be characterised as a 'disconnection syndrome' where the hippocampus is cut off

from the cortex (Delbeuck et al., 2003). Another indication that synchrony changes in AD is that AD patients are also more likely than the general population to have seizures - which are driven by epileptic (i.e. abnormally hypersynchronous) activity (reviewed in Palop and Mucke, 2009). A number of studies using EEG recordings in the J20 mouse have demonstrated that this mouse is also prone to epileptiform activity with non-convulsive seizures (Palop et al., 2007; Roberson et al., 2011). Epileptiform spike activity in this model appears to be dependent on the presence of amyloid- β , as suggested by a study where J20 mice treated with bexarotene, a drug that increases the clearance of amyloid plaques and oligomers, showed reduced spike frequency (Bomben et al., 2014). Furthermore, there appears to be a causal link between changes in the gamma band (20-80Hz) of the LFP and epileptiform spiking in the J20 such that both reflect altered parvalbumin (PV) cell activity. Verret et al. (2012), also using EEG, found that J20 mice show increased spiking mainly in periods of reduced gamma activity (20-80Hz). By applying both pharmacological and genetic manipulations that affect PV cell function, they found that manipulations that increase spiking activity also decrease gamma intensity, and vice versa. The reduction in gamma appears to represent a decrease in the effectiveness of inhibition from PV cells in J20 mice, and hence the lack of inhibition allows the runaway epileptiform activity to emerge Verret et al. (2012).

Apart from local hypersynchrony, there may also be a reduction of synchrony between brain areas in AD. For example, APP23xPS45 mice show reductions in coherence compared to wildtypes in both cortical and hippocampal brain areas (Busche et al., 2015). This was assessed using calcium imaging of a very large region of cortex encompassing both hemispheres, as well as LFP. Interestingly, Busche et al. (2015) suggest that the global breakdown of synchrony is due to a decrease in the effectiveness of inhibitory interneurons, although unlike Verret et al. (2012) they did not pinpoint a specific interneuron type as responsible for the deficits.

Tau models of Alzheimer's also show changes in LFP power, which also appear to be linked to changes in inhibition, although the relationship of LFP changes to

inhibitory dysfunction is less clear than in the J20 mouse. For example, Witton et al. (2014) found that sharp wave ripple power in CA1 is reduced in Tg4510 mice, and that this appears to be driven by a failure of inhibition, where inhibitory neurons had worse temporal and phase locking to sharp wave ripples in Tg4510 mice compared to wildtypes, but pyramidal neuron temporal and phase locking was normal. Tg4510 mice also display a broad decrease in power across all frequencies as neurodegeneration progresses, as observed in entorhinal cortex by Booth et al. (2016).

In this thesis I investigate how changes in synchrony and other measures of the local field potential relate to behavioural performance. Previous research in mouse models of other brain disorders has demonstrated that behavioural symptoms are sometimes accompanied by observable changes in the LFP. For example, in a mouse model of schizophrenia, prefrontal-hippocampal coherence correlated with behavioural performance, and was decreased in transgenic compared to wildtype mice when the mice reached the decision point in a T-maze (Sigurdsson et al., 2010). We might expect that the clear spatial memory problems displayed by mouse models of Alzheimer's disease, for example in the Morris Water Maze, a standard test of spatial memory (Cissé et al., 2011; Palop et al., 2003; Ramsden et al., 2005), would also be reflected in some aspect of their neural activity such as some of the measures discussed above.

1.2.2 Changes in the spiking activity of single neurons

Another kind of altered activity that may be related to function is spiking hyperactivity, which has been observed in a series of studies in the APP23xPS45 mouse in single neurons in prefrontal and visual cortex and also in the hippocampus (Busche et al., 2012, 2008; Grienberger et al., 2012). Not only does hyperactivity drive amyloid- β production (Cirrito et al., 2005), it also appears to be driven by amyloid- β levels in the living brain. Hyperactive neurons tended to occur near plaques (Busche et al., 2008), and hyperactivity could also be induced in wildtype mice by acute application of soluble amyloid- β , and reduced in the AD model by amyloid- β clearance (Busche et al., 2012). Furthermore, hyperactive firing across neurons was

relatively synchronous (Busche et al., 2008), which suggests it could form the basis of the epileptiform activity discussed above. The number of hyperactive neurons also increased with disease progression (Grienberger et al., 2012). However, the exact functional consequences of this hyperactivity are unclear. Grienberger et al. (2012) found, using anaesthetised APP23xPS45 mice, that orientation selectivity and direction selectivity was reduced in neurons in visual cortex in AD model mice over the age of 4 months, and that hyperactive neurons appeared to have especially low orientation selectivity. However, a later study using awake mice found no differences in orientation and direction selectivity between the transgenic and wildtype mice (Liebscher et al., 2016), even though the mice were 10-11 months old, an age at which mice in the other study showed a large difference. It is unclear whether this difference in results is due to differences in the awake versus anaesthetised state or something else.

All of these studies also found increased numbers of hypoactive or silent neurons in the APP23xPS45 mice compared to wildtypes. The proportion of hypoactive neurons also increased with disease progression (Grienberger et al., 2012), however, proportion of hypoactive neurons was not linked with plaque distance (Busche et al., 2008). Hypoactive neurons in the AD model also showed no visual responses even when treated with a GABA receptor antagonist despite the treatment restoring spontaneous activity. In contrast, some hypoactive wildtype neurons were visually responsive with similar orientation selectivity and direction selectivity to normally firing neurons (Grienberger et al., 2012).

Hypoactive neurons have also been observed in the Tg4510 tauopathy model of Alzheimer's disease. Menkes-Caspi et al. (2015) found reduced firing in the prefrontal cortex of Tg4510 mice, which was accompanied by longer down states and lower firing during up states. Jackson et al. (2017) also observed reduced firing rates in barrel cortex in response to whisker stimulation. However, results in this model are less clear cut - for example Kuchibhotla et al. (2014) found normal levels of activity, measured by calcium imaging, in the visual cortex of Tg4510 mice. This was the case even in NFT-bearing neurons in the Tg4510 mice. Crimins et al. (2012)

also observed hyperactivity rather than hypoactivity in frontal cortical neurons, but these results were in slice.

Overall, it appears that some type of disruption of neuronal firing is a common feature of many Alzheimer's models, but the conditions that drive this change in activity - both immediate environmental, area, and behavioural state differences, and the link between activity and pathology - is not completely clear.

1.3 Brain areas of interest

In this section, I describe the function of two brain areas that I investigate in my project - the hippocampus (specifically CA1) and the primary visual cortex. I have focused on the hippocampus because of the well-known changes that occur in this area during Alzheimer's disease, leading to memory and navigational impairments, and I have focused on primary visual cortex because of what this area can tell us about changes in information processing due to pathology.

1.3.1 Hippocampus

The hippocampus has been the focus of intense research for many decades. Starting with patient H.M., who showed profound amnesia but otherwise normal cognitive function after bilateral hippocampal removal (Scoville and Milner, 1957; Corkin, 2002), the hippocampus has been known as a key area for memory formation and retrieval. The hippocampus also enables spatial processing - one of the key early findings was the discovery of place cells in the hippocampus, which fire when an animal is in a specific location (O'Keefe and Dostrovsky, 1971).

The hippocampus is a structure which sits below the cortex and is widely connected to other brain areas. Internally, the most studied connectivity within the hippocampus is the 'trisynaptic loop' - the circuit running from entorhinal cortex to dentate gyrus (the perforant path), dentate gyrus to CA3 (mossy fibres) and CA3 to CA1 (Schaffer collaterals), from where output is sent to many different brain regions. Beyond this, hippocampal circuitry and connectivity is in fact far more complicated - a recent comprehensive review of hippocampal function and connectivity by Hunsaker and Kesner (2018) describe a large number of different connec-

tions both internal and external to hippocampus which underlie the various types of function known to be subserved by the hippocampus.

One of the most famous signatures of hippocampal activity is long term potentiation (LTP), first described by Bliss and Lømo (1973) in the rabbit. When the perforant path was stimulated, initially, the magnitude of the response recorded in the dentate gyrus was small. However, following repeated stimulation, the magnitude of the response in the dentate gyrus greatly increased. LTP, as a clear demonstration of long-lasting change in synaptic strength in a structure already known to be important for memory, is widely thought to be the basis for memory formation in the hippocampus (Bliss and Collingridge, 1993). Due to the association between LTP and memory, function, LTP has been used widely in Alzheimer's disease models as a measure of synaptic and hippocampal function (Hoover et al., 2010; Saganich et al., 2006; Larson et al., 1999).

The hippocampus is a key region in Alzheimer's disease, not just because of pathological findings, but also because of the symptoms of AD, which align with deficits also known to occur in patients or animals with hippocampal damage. Memory impairment is the most common cognitive symptom of AD, although other cognitive deficits, for example in navigation, executive function, and language, often co-occur with memory problems (McKhann et al., 2011). Cognitive symptoms increase in severity as the disease progresses, and are also apparent in preclinical stages. For example, people who go on to develop AD show decreased performance on a variety of different memory tests up to 9 years before diagnosis (Amieva et al., 2005). While memory deficits, in particular episodic memory (Bäckman et al., 2001, 2005), are the most obvious cognitive deficits in the prodromal stage, measures of spatial function are also affected in the preclinical stages. Not only do patients with MCI (mild cognitive impairment) show navigation deficits, the extent of the deficit is predictive of which patients will later develop AD (Hort et al., 2007; Laczó et al., 2009).

In fact, changes in the processing of spatial information accompany hippocampal degeneration in Alzheimer's patients. Hippocampal volume, in addition to be-

ing reduced in late stage AD (Braak and Braak, 1991), is predictive of conversion to AD from MCI (Jack et al., 1999), and in both AD and MCI patients, hippocampal volume is reduced in participants with poor memory and spatial performance (de Toledo-Morrell et al., 2000; Laakso et al., 1995; Nedelska et al., 2012). Furthermore, the relationship between spatial function and hippocampus that has been observed in humans is also present in rodents - and using rodents allows researchers to not only record from place cells but to quantify the quality of spatial information that is contained in single neurons or populations of neurons (O'Keefe and Dostrovsky, 1971; Skaggs et al., 1993). This allows spatial function in the presence of Alzheimer's pathology to be investigated using mouse models. In fact, both amyloid and tau mouse models of Alzheimer's have also been shown to have spatial information deficits (Cheng and Ji, 2013; Cacucci et al., 2008).

Therefore, understanding changes in hippocampal function, specifically in relation to spatial function, is key in understanding the functional changes that take place in Alzheimer's disease. Many of the measures used to assess mouse models of Alzheimer's disease, such as the Morris water maze or LTP protocols in slice, already focus on the hippocampus, and hippocampal changes in Alzheimer's models are already quite widely studied. While changes in hippocampal function are undoubtedly important, I will make the argument that primary visual cortex, rather than hippocampus, is a better choice of area to use in understanding how Alzheimer's pathology affects neural function.

1.3.2 Primary visual cortex

The primary visual cortex (V1) is the first cortical area in the visual pathway. After visual information is encoded and processed by the retina and lateral geniculate nucleus (LGN), thalamocortical neurons from the LGN carry visual information to V1 - this basic pathway is the same in many model systems including mouse, cat, monkey and human (Seabrook et al., 2017). Although primary visual cortex is not traditionally an area of interest in AD research, it could be a useful area to look at in regard to the problem of information processing in AD. There are some indications that the early visual system is affected relatively early in AD, even if it is

not specifically targeted by AD pathology. Braak and Braak (1991) identify occipital cortex as one of the first areas to show amyloid pathology, and there has also been interest in using retinal abnormalities as an early or even preclinical marker of Alzheimer's disease, as changes in retina thickness have been found in mild AD and also MCI patients (Paquet et al., 2007; Krantic and Torriglia, 2014; Berisha et al., 2007). However, AD pathology does not appear to be selective for primary visual cortex. For example, primary visual cortex and visual association cortices in post-mortem AD brains had a similar level of plaque load, and primary visual cortex actually had less tangles than nearby association cortex (Lewis et al., 1987).

The main reason why looking at V1 might be useful for AD research is that we have a comparatively more advanced understanding of what computations primary visual cortex is performing and the kind of information it receives as input and sends as output (reviewed in Carandini et al., 2005) compared to other brain areas that are more commonly studied in AD research such as the entorhinal cortex or hippocampus proper. For example, models and measures of V1 function can draw on very specific features of the environment such as the position of a stimulus in the visual field, the size, contrast and luminance of stimuli, the speed of visual flow, and relate these directly to V1 activity.

Early studies in the primary visual cortex by Hubel and Wiesel and the cat and primate showed that 'simple' V1 neurons displayed orientation selective responses, with a centre-surround structure to their receptive field (Hubel and Wiesel, 1962, 1968). While most vision research has historically been carried out in the cat or monkey, mice have begun to take a larger role in vision research. Although mice do not have orientation maps in V1, unlike cats and primates (Ohki and Reid, 2007), mice show many similarities in V1 neuron properties to humans and other mammals, for example orientation selectivity, direction selectivity, contrast sensitivity and sensitivity to spatial frequency (Niell and Stryker, 2008). V1 neurons in mouse also have a centre-surround receptive field structure similar to cats and primates (Van den Bergh et al., 2010). This receptive field structure has been shown to arise from local inhibition within V1 (Adesnik et al., 2012). Mice also show interesting

feedback processing in V1 - for example, mouse running speed affects surround suppression (Ayaz et al., 2013). The use of mice in vision research has also opened up a huge range of techniques including the use of transgenic mice, which is particularly relevant to my own project as it is now possible to look at visual cortical activity in AD models. As discussed above, the studies of primary visual cortex function in AD models by Grienberger et al., Liebscher et al. and Kuchibhotla et al. have not been particularly conclusive, so I hope that my own project will make some useful contributions to this area of research.

Investigating V1 function gives us more precise tools to understand how exactly processing is changing in response to neurodegeneration, by quantifying changes in terms of parameters of a response model fitted to a neuron's actual response to a stimulus. This makes V1 a more advantageous area to understand changes in information processing compared to, for example, CA1. Although CA1 is more affected by pathology, single unit responses in CA1 cannot be as precisely modelled, and the range of stimuli for which responses are clearly defined in CA1 (primarily mouse location) is small compared to the wide variety of visual stimuli for which V1 response models exist.

1.4 Experimental paradigms

In this section I review the two main experimental paradigms I use in the course of my project - the delayed alternation T maze and rodent virtual reality.

1.4.1 Delayed alternation T maze

The delayed alternation T maze is a popular and sensitive test of spatial working memory in rodents, and perhaps also long term memory if the delay is long enough (a standard protocol and some details are outlined in Deacon and Rawlins, 2006). The task is essentially a delayed non-match-to-sample task, with a spatial component to make it more ethological for rodents, although of course this spatial component affects what functions and circuits the task assesses. Successful T-maze performance depends on hippocampal function. Total hippocampal lesions disrupt T-maze performance (Bannerman et al., 1999), and specifically the dorsal part of the

hippocampus is required, as ventral lesions have no effect on performance (Bannerman et al., 2002). While hippocampus appears to be the key region involved in T-maze performance, performance in the alternating T maze task is also impaired by lesions of the entorhinal cortex (Ramirez and Stein, 1984) and the fornix, but performance does not change if the perirhinal cortex is lesioned (Bussey et al., 2000). Other regions involved in T maze performance are the prefrontal cortex (Sigurdsson et al., 2010) and many subcortical regions including the basal ganglia and various thalamic nuclei (reviewed in Lalonde, 2002).

As well as being sensitive to hippocampal lesions and more subtle types of hippocampal dysfunction in both its rewarded and continuous types (Reisel et al., 2002; Gerlai, 1998), the delayed alternation T maze may also be particularly sensitive at detecting spatial dysfunction in AD mice. A review by Stewart et al. (2011) of a range of studies using different tasks to assess spatial function in the Tg2576 mouse (an APP model) found that the alternation T maze task was most sensitive at detecting deficits in spatial function in this model, even more than the Morris Water Maze. T-maze performance also correlates with a measure of LTP in Tg2576 mice (Chapman et al., 1999). In the Tg4510 mouse, T-maze performance correlates strongly with tau burden in the cortex and hippocampus, and it also correlates strongly with the level of cortical and hippocampal atrophy in individual mice (Blackmore et al., 2017).

In the delayed alternation T maze task, the mouse is placed in a start box and runs up the centre arm. At the end of the centre arm it is presented with a sample phase where only one out of the right and left arms of the maze is left open, the other being blocked by a door. After reaching the end of the sample arm, the mouse returns to the start box, either by being carried by an experimenter or by running there itself if the design of the maze allows it, and is held in the start box for a delay length specified by the experiment. After the delay, the door between the start box and the centre arm is opened and the mouse is presented with the choice phase, where both left and right arms are open and it must choose the non-match-to-sample arm i.e. the one that was not blocked in the previous forced phase. This task has

both spontaneous and rewarded variants. As mice like to explore novel areas, their tendency to spontaneously alternate the arm they explore can be used as to assess how good their memory is for previously visited locations - if they forget which arm they previously visited, they are less likely to alternate as they do not remember which arm is familiar and which is novel. Although spontaneous alternation can be done with no training, mice do not explore the areas very quickly so each session can take a long time. With the rewarded version, mice are encouraged to display alternation behaviour through food reward when they make a correct choice in the choice phase.

One potential problem with automated T mazes is that continuous alternation mazes have been shown to be less sensitive to hippocampal dysfunction than discrete mazes. Typically in a continuous alternation maze, the maze only has three arms (known as a Y maze) and the mice must return to the start box by going back down the choice arm and then back down the centre arm. Performance in continuous alternation mazes of this type has been shown to correlate less well with hippocampal dysfunction (Blackmore et al., 2017).

In contrast, the mazes I used have a dedicated return arm on each side which connects the reward zone to the start box. Once mice reach the reward zone, the door between the choice arm and centre arm is closed so they cannot return via the centre arm but must use the return arm instead. Therefore, as the mice cannot return via the choice arm, the continuous nature of my T mazes should not pose a problem for assessing spatial dysfunction in my mice.

In fact, using this continuous version is also beneficial due to the lack of handling during the task. Firstly, the mice are likely to be less anxious and stressed when experimenter handling is minimised. By using automated T-mazes, I only handle the mice when putting them in the maze, and taking them out again at the end of the session, rather than handling them in between each trial phase as is required with a discrete T maze. Secondly, the lack of experimenter handling will hopefully allow the mice to perform better as they are not be be distracted by experimenter actions and interference. Thirdly, by only handling the mice at the

beginning and end of the sessions, introduction of experimenter bias, such as either consciously or unconsciously using different types of handling for transgenic versus wildtype mice, can be avoided.

1.4.2 Rodent virtual reality

Rodent virtual reality is a relatively new type of experimental setup that allows for recording from awake head-fixed mice or rats while they run on a treadmill. It has been used successfully to elicit spatial behaviour and place cell activity (Aronov and Tank, 2014; Harvey et al., 2009; Youngstrom and Strowbridge, 2012; Chen et al., 2013; Ravassard et al., 2013). In my experiments, I use a vision-centric virtual reality setup, where the mouse's movements on a cylindrical treadmill drive changing visual input, which is presented to the mouse on screens surrounding the treadmill. The visual environment is designed to look like a plausible real world spatial environment (a linear track) with different visual cues in the forms of gratings or plaids on the virtual walls. A version using a spherical treadmill is described in Saleem et al. (2013). The main benefit of rodent virtual reality over real world tasks when used in conjunction with electrophysiological recording techniques is the amount of control of the environment that virtual reality provides compared to the real world, especially when the virtual reality is treated as a spatial environment.

Firstly, virtual reality environments can restrict spatially informative cues to only the modalities of interest, in this case vision. Whereas in real world environments, olfactory, auditory, tactile and self-motion cues can all provide an animal with information about its location, in virtual reality it is possible to decouple these from virtual location. While the animal is head-fixed on the treadmill and occupies a static position in real space, auditory and olfactory cues will remain the same. The utility of self-motion cues as well as other features of the treadmill such as varying treadmill texture can also be dissociated from virtual location by varying the gain between treadmill speed and the speed at which the visual virtual environment moves (visual speed) on a trial-by-trial basis. Hence, the only modality that provides information about virtual location to the mouse would be vision.

A second benefit of virtual reality environments is that environments can be

altered on a very fast timescale, with the limiting factor being the time it takes for the computer to generate the new virtual environment display i.e. tens of milliseconds compared to the much longer time it would take an experimenter to switch out cues in the real world. It is also possible to have a much greater range of environmental cues than in the real world, for example gratings of many varying contrasts, because the cues only need to be displayed on a computer rather than manufactured as would be the case in a real world maze.

A final important aspect of control in virtual reality is head fixation. By fixing the mouse's head and tracking its eye position, we can be a lot more certain about what it is seeing at any moment. While a mouse in the real world can move nearer or further away from a visual stimulus, making the size of the stimulus' retinal image bigger or smaller, or could turn its head so that the cue falls in a different part of the visual field, a head-fixed mouse is unable to make large movements towards or away from the stimulus and can only move its eyes. Comparatively speaking, eye movements can only make small changes to the position or size of a stimulus in the visual field. Hence we can be relatively sure that if we present the same visual stimulus to a head-fixed mouse on multiple trials, or indeed the same stimulus to two different head-fixed mice placed in the same apparatus, the mice will see almost the same stimulus on repeated presentations. This makes virtual reality particularly useful for characterising information processing problems, as changes in neural response between trials of repeated stimulus presentations, or between different mice when shown the same stimulus, can be attributed to differences in how the sensory information is processed by the brain, rather than differences in the stimulus itself.

1.5 Outline of thesis

The main aim of this thesis is to characterise functional changes in information processing in a mouse model of Alzheimer's, using measures of neural activity that are as precise as possible.

In Chapter 2, I assess changes in LFP power and synchrony in the J20 mouse in

a T-maze task, and compare these results with similar experiments by my colleagues using Tg4510 mice. The aim of these experiments was to decide which mouse model to use for the more complex head-fixed experiments, where measurements of neural activity would be more stimulus-specific - for example, looking at single unit responses to different types of visual stimulus - than in the T-maze. Following these experiments, I decided to use the Tg4510 mouse.

In Chapter 3, I outline the experimental protocol and methods used for the head-fixed experiments.

In Chapter 4, I explore changes in LFP power in various experimental protocols, specifically exploring how LFP power changes in response to different kinds of information, including both visual and self-motion information.

In Chapter 5, I investigate changes in the response of single units in V1 to various types of visual stimulus, and assess how different kinds of processing change in tau-expressing Tg4510 mice. These include changes in spatial receptive field, changes in orientation and adaptation effects.

Chapter 2

Comparing a tau and amyloid model of Alzheimer's disease

2.1 Introduction

2.1.1 LFP in T maze

As described in Chapter 1, the delayed alternation T maze is a popular standard task for assessing spatial abilities, memory and hippocampal function which has been used in a variety of different mouse models with different task parameters. Hence, a lot is known about what factors affect performance in the task and the possible interpretations of behaviour if an impairment is found. Moreover, it is a relatively simple task to learn, even for mice affected by AD pathology (Stewart et al., 2011), in that deficits occur primarily in memory performance rather than inability to learn the task.

2.1.2 Aims and hypotheses

My aim in these T-maze experiments was to achieve a relatively simple comparative characterisation of functional decline using measures and an experimental protocol that were already widely used (Sigurdsson et al., 2010, and many other model characterisations run by my collaborators at Eli Lilly). By assessing behavioural changes, and understanding to what extent the behavioural changes were associated with functional changes in power, phase-amplitude coupling or coherence, I could decide which mouse model would be best for the far more complex and time

consuming head-fixed experiments that I was in the process of setting up.

Larger changes in power etc in one model versus another, particularly changes that grew larger as neurodegeneration progressed, would indicate that this model would be more likely to show changes in my later head-fixed experiments. If, on the other hand, one of the models showed few changes in power and other measures despite showing behavioural change, it would be a poor candidate for head-fixed experiments.

We looked at the 5-6 month timepoint and the 10-11 month timepoint to understand power changes and behaviour changes when amyloid-beta levels are moderate (5-6 months) and severe (10-11 months). At the 5-6 month timepoint, J20 mice should show elevated levels of soluble amyloid-beta as well as some oligomeric forms, but no plaques, whereas at the later timepoint the mice should have a substantial plaque load in addition to increased soluble and oligomeric amyloid-beta (Wright et al., 2013). J20 mice should also reliably show deficits in spatial tasks at both timepoints, as well as progressive decline in performance as pathology increases (Wright et al., 2013; Cheng et al., 2007).

2.2 Methods

During these experiments I was not blinded to the group identity (J20 or WT) of the mice. This was because the rules of the animal facility where the mice were housed required that the mouse genotype (J20 Het or J20 WT) should be displayed on the cage cards. This may have introduced bias while handling the mice for experiments, performing food deprivation or analysing the neural data. Bias from running the experiments unblinded was minimised as follows: as the T-mazes were fully automated, my handling was limited to putting the mouse in the maze at the beginning and taking it out at the end. To minimise bias during food deprivation I used clear criteria - maintaining weight at $\geq 85\%$ ad libitum weight, optimally around 90%. Analysis decisions, such as which channels to use, were also made on the basis of pre-defined criteria which were applied to all mice. Nevertheless there may have still been unconscious differences in how the J20 and WT mice were

treated.

2.2.1 Surgery

All surgeries were performed by my colleagues at Lilly.

11 wildtype (WT) and 9 J20 mice were implanted with custom fixed dual shank probes with one shank in the hippocampus (-1.94mm, +1.25mm from bregma) and one in prefrontal cortex (+1.7, +0.35 from Bregma). Mice were anaesthetised using an induction box at 3% isoflurane. The head was shaved and the mouse secured in the surgical apparatus using earbars and a tooth holder and isoflurane was reduced to 2%.

The mouse was injected subcutaneously with 0.5ml of Hartman's and Lacrilube and eye shields were applied to its eyes. The skin was cleaned using Hibiscrub and alternating application of iodine and alcohol. After cleaning an incision was made in the skin down the length of the skull and the skin was held back from the skull using sutures. Tissue was cleaned from the skull using alternating hydrogen peroxide and saline wash. Following this, bregma and the position for both exposure holes was measured using a stereotax and marked with a cauteriser. Skull screws were placed in each bone plate and the exposure holes were made with a powered drill. The probe was placed in the stereotax and position relative to bregma was double checked before lowering the probe to the surface of the brain. When the probe reached the brain surface, it was slowly lowered to the desired depth (2mm) over about a minute. After applying a protective surrounding layer of Vaseline using tweezers and a cauteriser, the probe connector body was secured to all except the cerebellar skull screw using dental cement. The ground wires were also encased in the dental cement and the ends of the wires stripped and attached to the cerebellar screw and coated with silver paint. The cerebellar screw was then also covered in dental cement and the stay sutures were removed. Loose skin around the implant was drawn together using dissolvable sutures and the mouse was given another 0.5ml of Hartman's and an antibiotic and analgesic (Rimadyl and Convenia).

The mouse was then removed from the surgery area and allowed to recover in a

heated box. The mouse was monitored for two hours post-op to check that it was recovering appropriately. After the monitoring period it was returned to its homecage with DietGel and other food supplements (sugar pellets and gummy treats) and daily post-op checks continued for two weeks before the mice were used in any experiment.

Two mice (1 WT and 1 J20) had broken hippocampal shanks so only the pre-frontal shank was implanted.

2.2.2 Behaviour

2.2.2.1 Timepoint 1 (5-6 months)

Following recovery from surgery (at least two weeks), mice were food deprived and food intake adjusted for each individual mouse to maintain its weight at $\geq 85\%$ of its ad libitum weight, with ideal weight being between 90 and 95% of ad libitum weight.

After a week of acclimatisation to food deprivation, mice were habituated in an automated continuous T-maze on a forced alternation paradigm lasting 2 sessions where they were rewarded with automatically dispensed sugar pellets (12mg), receiving 1 pellet for reaching the reward zone and 1 pellet for returning to the start box. During forced alternation, one randomly selected arm would be blocked on the sample phase, and the opposite arm would be blocked on the choice phase, so mice were unable to make an incorrect choice. Each session lasted a maximum of 40 minutes with a maximum of 20 trials. If mice reached the maximum number of trials before the time limit was reached, they were returned to the home cage. Conversely, if they reached the time limit before they reached the maximum number of trials, they were removed from the maze and returned to the home cage when the time limit was reached.

After habituation, a single delayed alternation paradigm was used where mice were presented on each trial with a sample phase where one arm was blocked, followed by a 5s delay where they were held in the start box. Once the delay ended, the mice were presented with a choice phase where both arms were open. Mice received 1 pellet in the reward zone and 1 in the start box if they chose the correct

arm (opposite to the sample) in the choice phase. However if they chose the wrong arm, they received no reward in either location. The mice ran six sessions each of this paradigm, with a maximum time of 40 minutes and a maximum trial number of 10 trials.

Finally, the mice were given a variable delayed alternation paradigm, where the delay could be either 5s or 120s. The delay type was randomised. The phases in each trial were the same as described above for the single delayed alternation. On the first session, mice were given a maximum time limit of 60 minutes and a maximum trial number of 40 trials. However, because no mice completed the maximum number of trials in the given time, in the second session the maximum number of trials was reduced to 20 and the time limit was kept the same.

12 WT and 9 J20 started the first timepoint but only 11 WT and 7 J20 mice completed the whole timepoint due to 1 early death in the J20s and two mice (1 WT and 1 J20) being culled due to reaching a humane endpoint.

After completing the first timepoint, mice were returned to ad libitum feeding.

2.2.2.2 Timepoint 2 (10-11 months)

Approximately 3 months after the first timepoint, surviving mice (10 WT, 4 J20) were run in the T-maze again. Habituation was not used at this timepoint due to the mice's previous experience with the maze, and after being put back onto food deprivation the mice began on the single delayed alternation paradigm. Mice ran for 5 sessions with a maximum time limit of 60 minutes and a maximum trial number of 20. The mice were then put on the variable delayed alternation paradigm using the same delays as before of 5s and 120s for two sessions with a maximum time limit of 60 minutes and a maximum trial number of 20.

There were no deaths during the second timepoint, so all mice that started the second timepoint also completed it.

2.2.3 Recording

The fixed probes had 8 sites on each shank, vertically arranged and spaced 150 microns apart. While the mice were on the T-maze or in sleep sessions in the home

cage, we recorded from all 16 sites at 2000Hz using TBSI wireless headstages and Spike2 software.

2.3 Results

2.3.1 Behaviour

Performance in the single delay paradigm was compared across the two timepoints by pooling results from all five or six sessions for a single mouse to get an overall measure of percentage of trials correct at each timepoint. The J20 mice had poorer performance than the wildtype mice (main effect of genotype: $F(1, 12) = 20.16$, $p = 0.000739$, $\eta_p^2 = 0.302$, J20 $M = 75.89$, $SD = 5.64$, $n = 4$ WT $M = 81.92$, $SD = 3.85$, $n = 10$) and performance worsened with age (main effect of timepoint $F(1, 12) = 6.25$, $p = 0.0279$, $\eta_p^2 = 0.205$, 5-6 months $M = 82.02$, $SD = 5.2$, $n = 14$ 10-11 months $M = 75.61$, $SD = 10.08$, $n = 14$, Fig. 2.1b). Somewhat surprisingly, there was no interaction effect ($F(1, 12) = 1.7$ $p = 0.217$), even though looking at mice individually, it appears that all of the J20s that survived to the second timepoint showed a decrease in performance, whereas the WT mice were more varied, with some showing decreased performance and some remaining stable (Figure 2.1a).

One potential problem with this timepoint analysis is that the 4 J20 mice that died due to genotype-related mortality before the start of Timepoint 2 had to be excluded. It might have been the case that the mice that had early mortality were also more impaired on the task. However, an independent samples t-test showed no difference in performance at Timepoint 1 between the J20 mice that survived to the later timepoint and the J20 mice that suffered early mortality ($t(6) = -0.560$, $p = 0.5961$ surviving J20s: $M = 78.3$, $SD = 3.85$, $n = 4$, non-surviving J20s: $M = 80.0$, $SD = 4.31$, $n = 4$).

I then assessed the mice's performance in the variable delay paradigm. If the 5s delay used in the single delay paradigm was too easy for the J20 mice, they could still perform well despite having a cognitive deficit, but with the more taxing 120s delay, differences in performance might emerge. However, again while there were

main effects of genotype (5-6 months: $F(1, 16) = 8.54$, $p = 0.00995$, $\eta_p^2 = 0.185$ J20 $M = 67.69$, $SD = 10.05$, $n = 7$ WT $M = 79.52$, $SD = 9.43$, $n = 11$) and delay (5-6 months: $F(1, 16) = 34.66$, $p = 2.29 \times 10^{-5}$, $\eta_p^2 = 0.475$ 5s delay $M = 82.50$, $SD = 8.16$, 120s delay $M = 67.34$, $SD = 14.12$, 10- 11 months: $F(1, 12) = 9.32$, $p = 0.0100$, $\eta_p^2 = 0.365$, 5s delay $M = 74.29$, $SD = 13.57$, 120s delay $M = 56.93$, $SD = 13.95$) at both 5-6 months and 10-11 months, there were no interaction effects (5-6months: $F(1, 16) = 2.18$, $p = 0.159$, 10-11 months: $F(1, 12) = 0.102$ $p = 0.75$), showing that the J20s did not appear to have a specific impairment at longer delays (Figure 2.2).

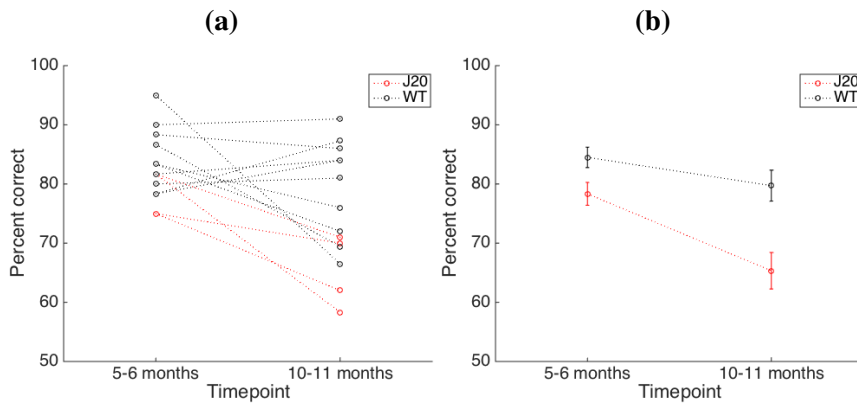


Figure 2.1: Performance on the T maze by age in the single delay paradigm. Only mice that had completed both timepoints (10 WT, 4 J20) were included in this analysis. Performance was measured using the percentage of correct choices (percent correct) made in a single session. All single delay paradigm sessions completed at a single timepoint were averaged for each mouse to give a mean percent correct at each timepoint. **(a):** Paired plots showing performance trajectories of individual mice by age. **(b):** Summary of performance by age for J20 and wildtype mice. Error bars are SEM.

2.3.1.1 Learning

To look at whether the J20s showed any differences in learning from WT mice, I examined whether various behavioural measures changed over training days in the single delay paradigm. The single delay paradigm was used because the mice completed 6 daily sessions (max 10 trials per session) of this paradigm at the 5-6 month timepoint and 5 sessions (max 20 trials per session) at the 10-11 month timepoint, compared to the 2 sessions completed at each timepoint in the variable delay paradigm.

As shown in Figure 2.3 mice did not show an improvement over time in their performance (no effect of training day at both 5-6 months, $F(5,85) = 1.42$, $p = 0.226$ and at 10-11 months, $F(4,48) = 2.04$, $p = 0.103$). This might be because the mice were already familiar with the task due to the forced alternation habituation sessions at 5-6 months, and perhaps memory of their previous experience of the maze at the 10-11 months timepoint. Mice also like to spontaneously alternate even when untrained so this might also contribute to the lack of improvement in performance, if their starting performance was already good.

As expected from the pooled results shown above, J20s performed worse than WT mice (main effect of genotype at both 5-6 months: $F(1,17) = 4.93$, $p = 0.0402$, $\eta_p^2 = 0.0300$, J20 $M = 79.14$, $SD = 3.88$, $n = 8$ WT $M = 94.09$, $SD = 5.34$, $n = 11$) and at 10-11 months: $F(1,12) = 10.19$, $p = 0.00775$, $\eta_p^2 = 0.0896$ J20 $M = 68.25$, $SD = 4.19$, $n = 4$ WT $M = 81.67$, $SD = 7.48$, $n = 10$). There were no interaction effects on percent correct (5-6 months $F(5,85) = 0.516$, $p = 0.764$, 10-11 months $F(4,48) = 1.26$, $p = 0.298$).

We also collected information on how fast the mice completed both individual trials and the whole session through three different measures: overall time on the maze, running speed in the centre arm, and choice latency (the time between the mouse starting the forced phase of the trial and leaving the start box on the choice phase of the trial). In contrast to performance measured by percent correct, all of these measures showed effects of training day at both timepoints (covered in Figure 2.3), with an interaction in centre arm running speed at 5-6 months ($F(1,85) = 2.38$, $p = 0.0456$, $\eta_p^2 = 0.0209$), but no effects of genotype emerged (see Fig. 2.3). Hence, both J20 and WT mice get faster at doing the task, which could be considered a kind of task learning as the mice become more efficient, even if the proportion of correct choices does not improve.

The lack of effect in proportion of correct choices might be due to the forced alternation habituation they received before this paradigm at timepoint 1, and possibly memories of the T-maze task at timepoint 2. Mice also like to spontaneously alternate even when untrained so this might also contribute to the lack of improve-

ment in performance, if their starting performance was already good.

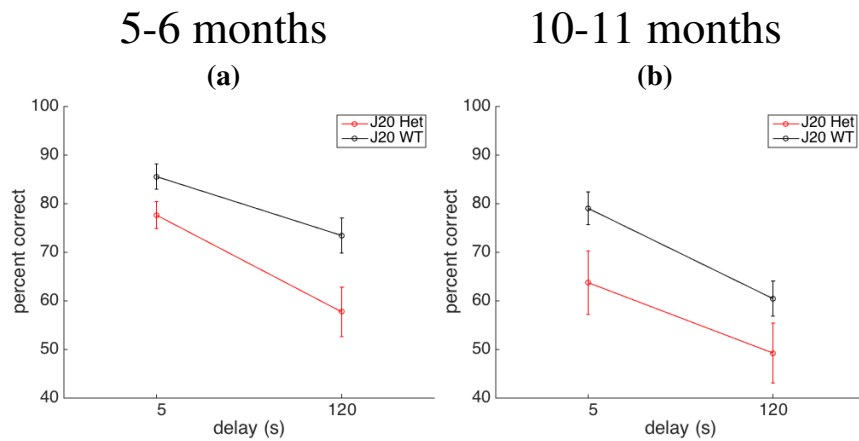


Figure 2.2: T maze performance in the variable delay paradigm.. Error bars are SEM. (a): 7 J20 and 11 WT completed the 5-6 months timepoint. (b): 4 J20 and 10 WT completed the 10-11 months timepoint.

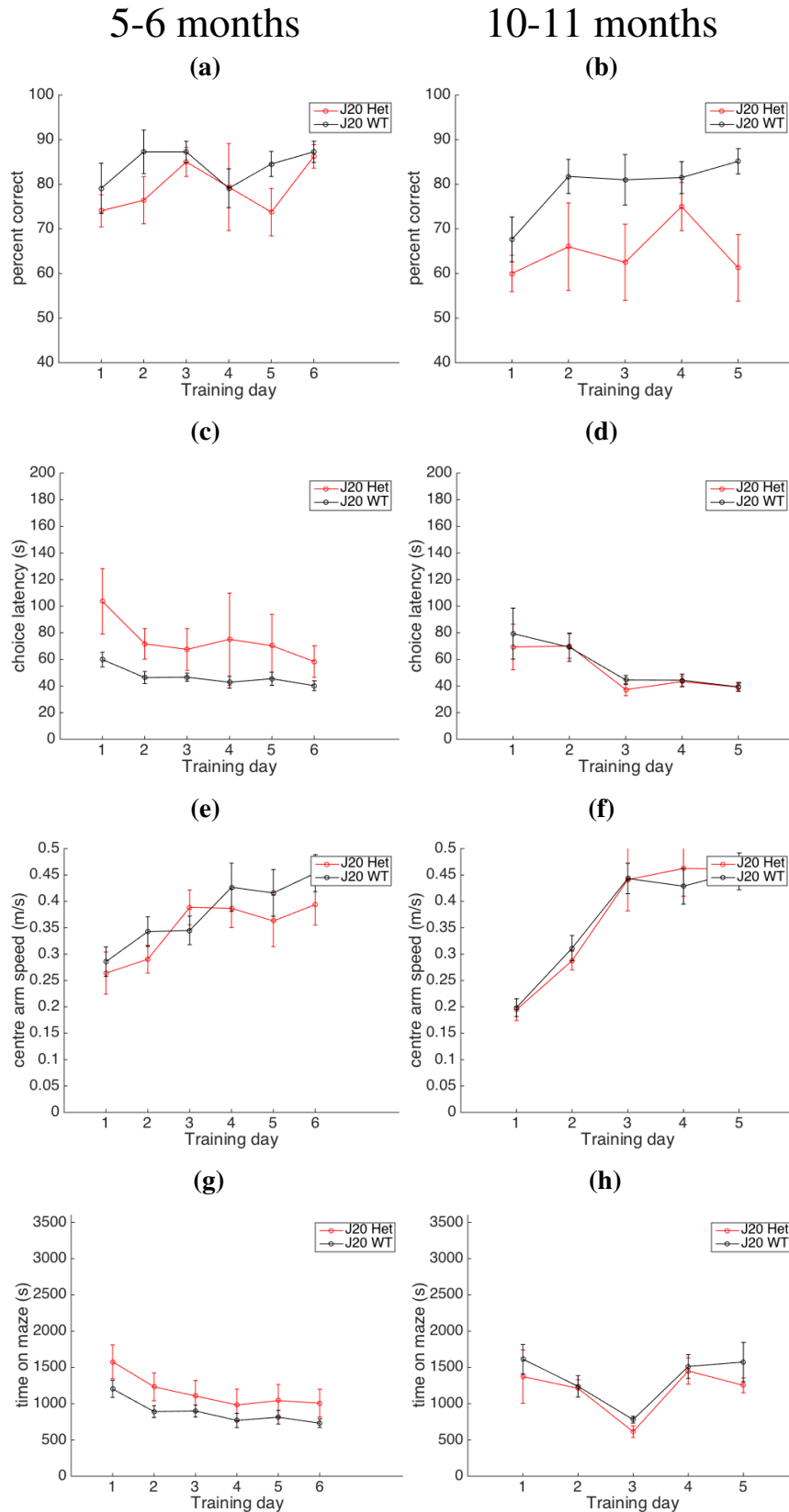


Figure 2.3: Behaviour by training day in the single delay paradigm.. Results from the 5-6 months timepoint are shown in (a), (c), (e) and (g), and results from the 10-11 month timepoint are shown in (b), (d), (f) and (h). Panels (a) and (b) show percent correct, (c) and (d) show choice latency (the time elapsed between exiting the start box on the forced phase and reaching the choice point in the choice phase), (e) and (f) show running speed on the centre arm averaged across both forced and choice runs, and (g) and (h) show overall time spent on the maze - i.e. how long it took for the mouse to complete the session. All error bars are SEM.

2.3.2 Power spectra and other LFP analyses

In order to understand whether changes in neural activity accompanied changes in performance, as has been previously observed in a schizophrenia model (Sigurdsson et al., 2010), I looked at power spectra, coherence and phase-amplitude coupling (PAC) of LFP at each timepoint. The single delay paradigm (5s) was used for all LFP analyses. LFP analyses were calculated from a 3s bin around the choice point of the maze (2s pre, 1s post) in choice but not forced runs.

Power spectra and coherence were calculated using the Chronux toolbox (<http://chronux.org>, Mitra, 2007) using the multitaper method and theta phase-amplitude coupling in CA1 was calculated using code and the cross-frequency coupling measure from Onslow et al. (2011).

Power spectra results were summarised by comparing mean power in specific frequency bands, which were delta (2-4Hz), theta (6-12Hz), beta (15-30Hz), low gamma (30-60Hz), high gamma (60-120Hz) and high frequency or ripple band (120-200Hz).

Phase-amplitude coupling (PAC) results were summarised by comparing theta-gamma coupling in the low gamma range, again taking the mean of PAC values within the low gamma range. Coherence results were summarised by comparing CA1-PFC coherence, again taking the mean value in the theta range.

I chose the CA1 channel for analysis by looking for ripples in the raw traces of the sleep session taken after the first variable delay session. I used a semi-automated ripple detection method (described in more detail in Chapter 4) where ripple events were detected by looking for threshold crossings in the z-scored Hilbert transform, with some further automated event rejection based on spectral properties. Ripple power is greatest in the stratum pyramidale (cell body layer of CA1), so after confirming that the ripple events that I found using my ripple detection method were true ripples and not noise artefacts, I selected the channel with the highest ripple amplitude as the CA1 channel. The CA1 channel was confirmed by checking for theta phase reversal (using the maze session LFP) at the selected channel. The prefrontal channel was chosen based on which channel showed the least noise.

There were no significant differences between groups in CA1 power at any measured frequency (beta, delta, theta, low gamma, high gamma, or ripple) at either timepoint between J20 and WT mice (Fig. 2.4a and 2.4b). In prefrontal cortex, power was significantly different between groups at 5-6 months in the high gamma ($t(18) = 2.25$, $p = 0.0375$ J20 $M = 3.2145$, $SD = 2.3030$, $n = 8$ WT $M = 6.0132$, $SD = 2.9694$, $n = 12$) and high frequency bands ($t(18) = 2.38$, $p = 0.02883$, J20: $M = 2.68$, $SD = 2.51$, $n = 8$, WT: $M = 5.88$, $SD = 3.2$, $n = 12$; see Fig. 2.4c and 2.4d, ripple band not shown in summary). However, there was no significant difference at any frequency at 10-11 months. For phase-amplitude coupling in CA1, theta-gamma coupling was significantly different at 5-6 months between groups ($t(14) = 2.25$, $p = 0.0414$ J20 $M = 0.4484$, $SD = 0.0741$, $n = 8$ WT $M = 0.5255$, $SD = 0.0619$, $n = 12$; Fig. 2.4e and 2.4f), but the difference went away at 10-11 months. CA1-PFC coherence, measured in the theta band, was significantly different at 5-6 months, with J20 mice having higher coherence than Wt mice ($t(14) = -2.28$, $p = 0.0385$, J20 $M = 0.8194$, $SD = 0.0794$, $n = 6$ WT $M = 0.7253$, $SD = 0.0800$, $n = 10$), but again was not different at 10-11 months (Fig. 2.4g and 2.4h).

2.4 Comparative data from Tg4510 mice

Similar experiments were run by James Butler and Anthony Blockeel (my collaborators at Eli Lilly) in female Tg4510 mice. For the 2 forced alternation habituation sessions, mice ran a maximum of 40 trials within 30 minutes, and mice were assessed at each timepoint using the 5s single delay paradigm, but were allowed to run 20 trials within 45 minutes for 5 sessions total, compared to my J20 mice which ran 10 trials within 40 minutes for 6 sessions. The mice were assessed at 3 different timepoints, 4, 6 and 8 months.

The Tg4510 mice showed a clear decline across the CA1 power spectrum (delta, theta and high gamma) at 6 months which increased at 8 months (Fig. 2.5b and 2.5c), but no changes or only minimal changes in PFC.

Phase amplitude coupling was also significantly decreased in Tau+ mice at 6

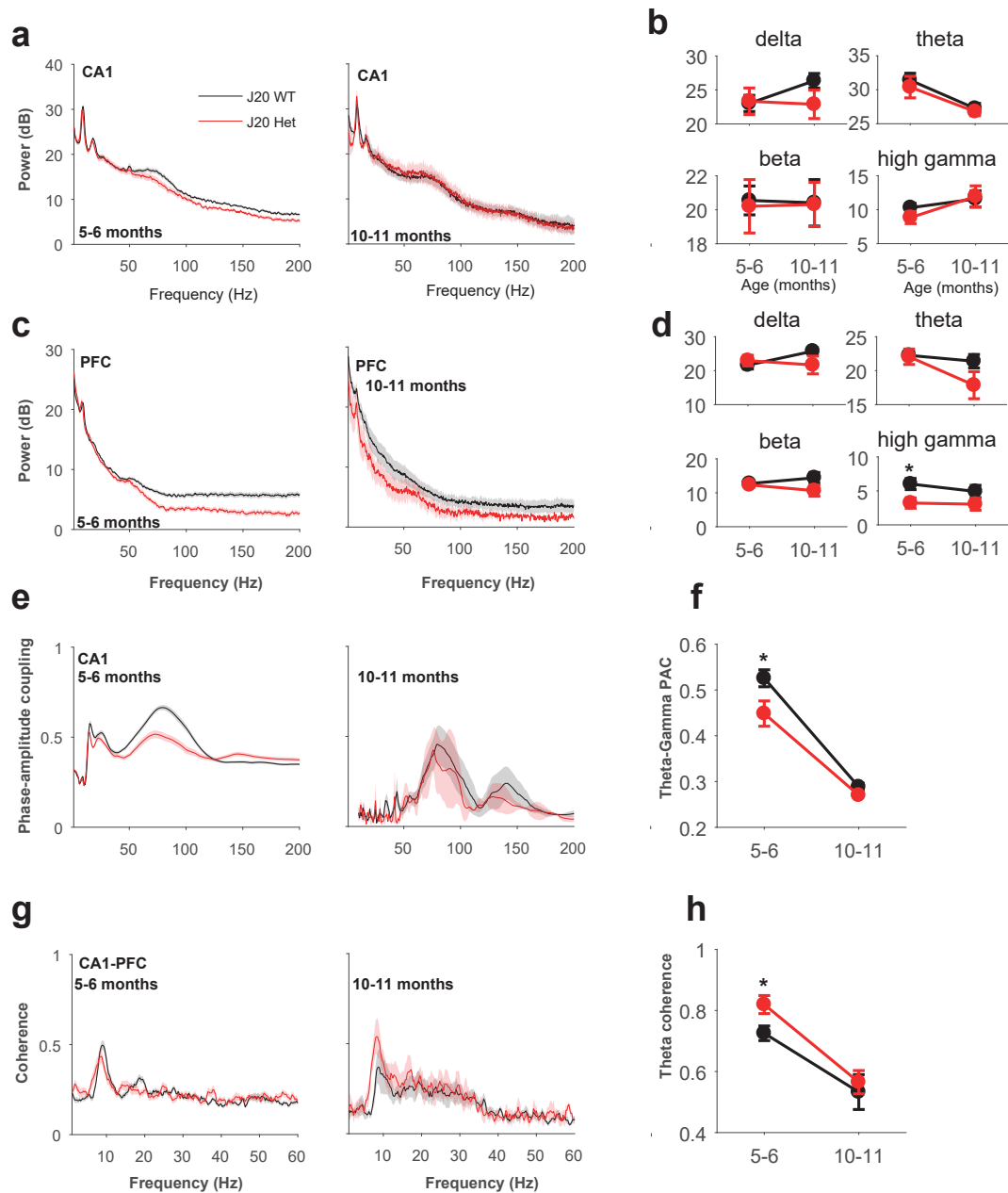


Figure 2.4: J20 results on the single delay alternating T-maze task. (a) CA1 power spectra from J20 and WT mice. (b) Comparison of CA1 power between groups at different timepoints in selected bands. (d) PFC power spectra from J20 and WT mice. (d) Comparison of PFC power between groups at different timepoints. (e) Phase-amplitude coupling in CA1 from J20 and WT mice (f) Comparison of phase-amplitude coupling at different timepoints. (g) CA1-PFC coherence from J20 and WT mice. (h) Comparison of CA1-PFC coherence at different timepoints.

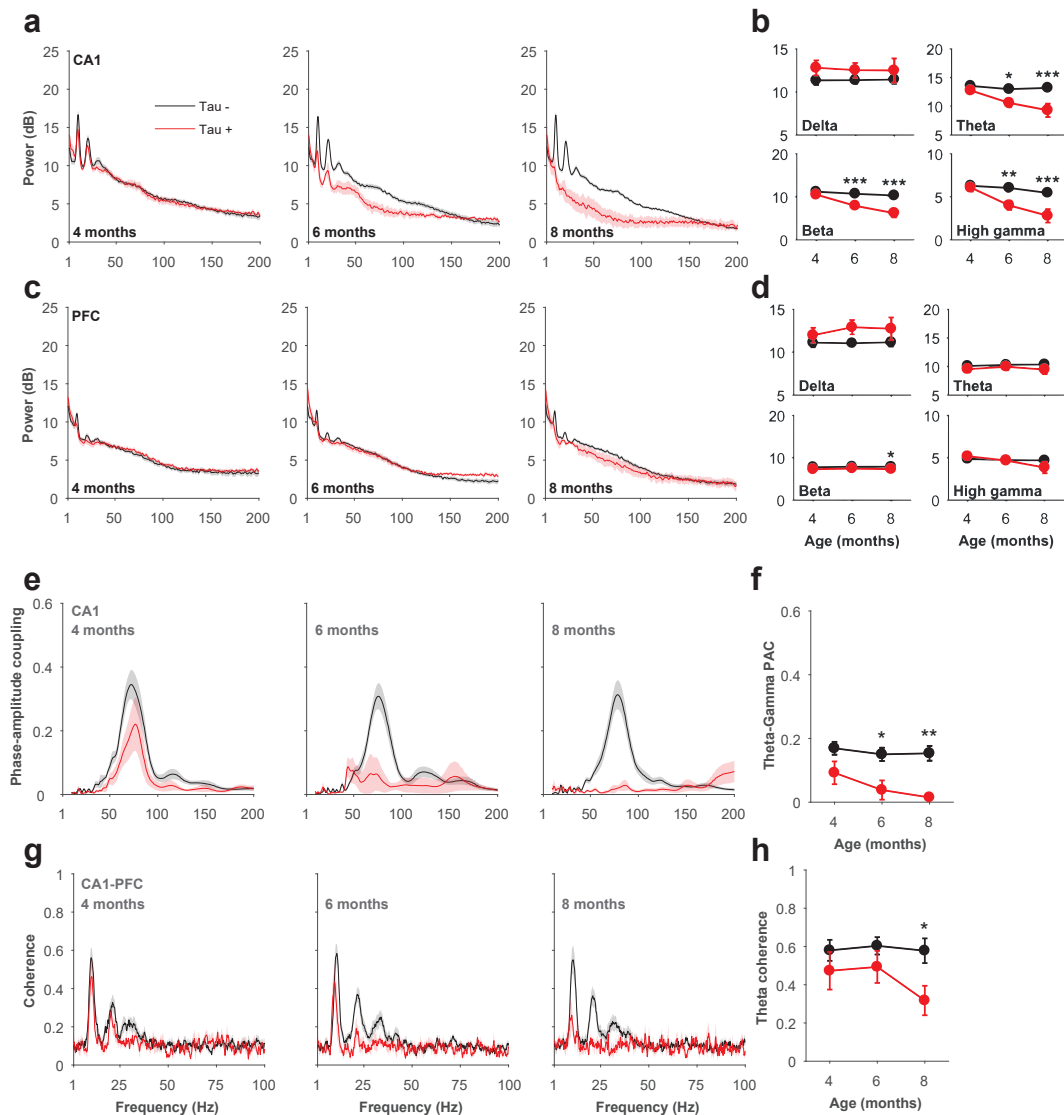


Figure 2.5: Tg4510 results on the single delay alternating T-maze task. (b) CA1 power spectra from Tau+ and Tau- mice from 3 timepoints (4 months, 6 months and 8 months). **(c)** Comparison of CA1 power between groups at different timepoints in selected bands. **(d)** PFC power spectra from Tau+ and Tau- mice. **(e)** Comparison of PFC power between groups at different timepoints. **(f)** Phase-amplitude coupling in CA1 in Tau+ and Tau- mice **(g)** Comparison of phase-amplitude coupling at different timepoints. **(h)** CA1-PFC coherence in Tau+ and Tau- mice. **(i)** Comparison of CA1-PFC coherence at different timepoints.

and 8 months (Fig. 2.5f and 2.5g), whereas changes in CA1-PFC coherence only emerged at 8 months (Fig. 2.5h and 2.5i). Auditory evoked potential amplitude (not pictured here) was also significantly reduced from 7 months onward.

2.5 Summary and choice of model

J20s generally performed worse than WT mice in the T-maze task, although the J20s did not show any specific impairments at older ages or longer delays, or over the course of learning. The J20 mice did not show any clear differences in CA1 power spectra, but power was reduced in PFC power spectra at higher frequencies. CA1 phase-amplitude coupling and CA1-PFC coherence. Despite these differences between the J20 and WT mice at the 5-6 month timepoint, there were no significant differences at the 9-10 month timepoint.

There are a few potential explanations for the lack of any age-related progression in our results. Firstly, it may be the case that neural changes in the J20 model do not correlate well with the progression of amyloid pathology. Although changes in neural activity have been previously observed in the J20 mouse (Verret et al., 2012; Palop et al., 2007), as well as behavioural deficits in tasks assessing spatial reference memory (Palop et al., 2003), these studies have not looked at the progression of changes in either neural activity or behavioural performance across different timepoints. In fact, a recent study that did assess J20 mice at different timepoints in a memory task (novel object recognition) found no decline of performance with age in the J20 mice (Ameen-Ali et al., 2018). However, it is not possible to know with our mice in particular whether amyloid pathology played a role, as dead mice were removed by facility staff before their brains could be taken for analysis.

A second possible explanation is that the J20 may be quite a variable model. For example, Mucke et al. (2000) showed that plaques are only present in 50% of J20 mice at 5-7 months, although as seen in the other lines they tested, this variability appears to be common to many amyloid models. If the speed of progression or severity of pathology varied between animals, and if neural changes are also correlated with amyloid pathology, the lack of differences in neural activity at 10-11 months might be due to less pathology in the mice that survived to this timepoint - unfortunately, the mice that died unexpectedly were removed by animal facility staff before their brains could be taken for histology, so it is not possible to confirm this explanation with certainty. However Mucke et al. (2000) also showed that by

10-11 months, 100% of J20 mice have amyloid plaques, so variability should not be an issue at this later timepoint - if anything, variability should be more obvious at the 5-7 month timepoint. Therefore variability in pathology in the J20 model is unlikely to explain our results.

An interesting question which probably does have some relevance to our 10-11 month timepoint results, however, is why J20 mice spontaneously die, and whether early death is related to any differences in neural activity (for example the elpileptiform activity widely studied in this model) or pathology. This spontaneous death has also been reported by Ameen-Ali et al. (2018).

In contrast, the Tg4510 mice showed clear differences between Tau+ and Tau- mice in CA1 power at 6 months, and in CA1 and PFC power at 8 months. There was also decreased phase-amplitude coupling in the Tau+ mice at 6 and 8 months, and decreased CA1-PFC coherence at 8 months. Progression of these effects at different timepoints was much clearer than in the J20s - for example, with CA1 power, phase-amplitude coupling and coherence, a very clear degradation can be seen across the entire spectrum, where power (and consequently PAC and coherence) decrease across time. Tg4510 mice also show a clear decline in T-maze performance over time, and performance correlates with tau burden (Blackmore et al., 2017). There was also no unexpected death in Tg4510 mice.

This clearer progressive change in LFP power and other measures in the Tg4510s, along with the fact that so many of the J20 mice died without warning, led me to decide to use Tg4510 mice for our head-fixed experiments.

Chapter 3

Experimental protocol and methods

In this chapter, I summarise methods used in my experiments with my Tg4510 mice, from initial assignment to Dox and Non-Dox groups to recording and protocol details. An outline of the experimental schedule is provided in Figure 3.1.

3.1 Dox assignment

I had several batches of Tg4510 mice, with each batch containing 6 mice, that had staggered birth dates and arrival times. Instead of randomly assigning mice to Dox and Non-Dox groups, I wanted to try to select mice for my recording experiments that were less likely to be hyperactive as excessive locomotor activity is known to occur in Non-Dox Tg4510 mice (Blackmore et al., 2017). As excessive locomotor activity is known to correlate with T-maze performance (Blackmore et al., 2017), I decided to use only mice with good T-maze performance.

Mice were assigned to either Dox or Non-Dox treatment at 3 months of age based on performance in a delayed alternation T-maze task (see Chapter 2 for more details of the experimental setup). For the T-maze sessions that were used for Dox assignment, mice were allowed to run a maximum of 40 trials within 60 minutes, and only 5s delays were used, unlike experiments in Chapter 2 where there was also a 120s delay.

Mice were then ranked within a batch based on T-maze performance (Fig. 3.2a) and of the top two performers, one was assigned to the Dox (Tau -) recording group and the other to the Non-Dox (Tau +) recording group. I was blinded to

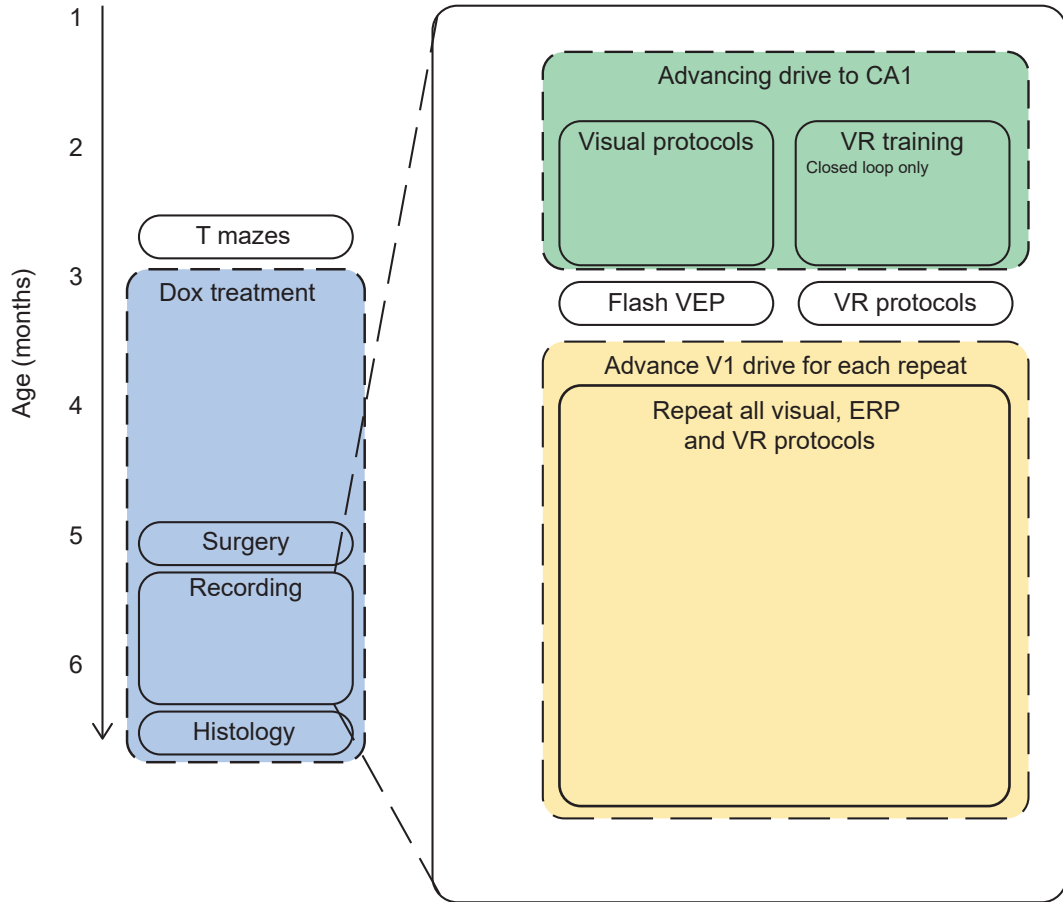


Figure 3.1: Overview of experimental schedule and recording protocols. An overview of the entire experimental schedule for mice involved in this study. Mice were assigned to Dox and Non-Dox groups at 3 months based on performance in a T-maze task. Around 5 months, probe implantation surgery was performed and recordings were taken over the next few weeks while running a series of visual and VR protocols. Mice were culled at 6.5 months and brains sectioned for histology.

the group identity of the mice and this ranking procedure was carried out by Anthony Blockeel, a postdoc at Eli Lilly, who also did all the probe implant surgeries later. The group that the top performer was assigned to (Dox or Non-Dox) alternated every batch so that performance was similar across the groups (percent correct $t(8) = -0.561$, $p = 0.5901$, Dox: $M = 84.4\%$, $n = 5$, Non-Dox: $M = 83.0\%$, $n = 5$ Fig. 3.2b).

The total number of trials completed was also similar across the groups ($t(8) = -0.244$, $p = 0.8133$, Dox: $M = 108$ trials, $n = 5$ Non-Dox: $M = 105$ trials, $n = 5$ Fig. 3.2c) as well as choice latency ($t(8) = 1.25$, $p = 0.2475$, Dox: $M = 27.6s$, $n = 5$,

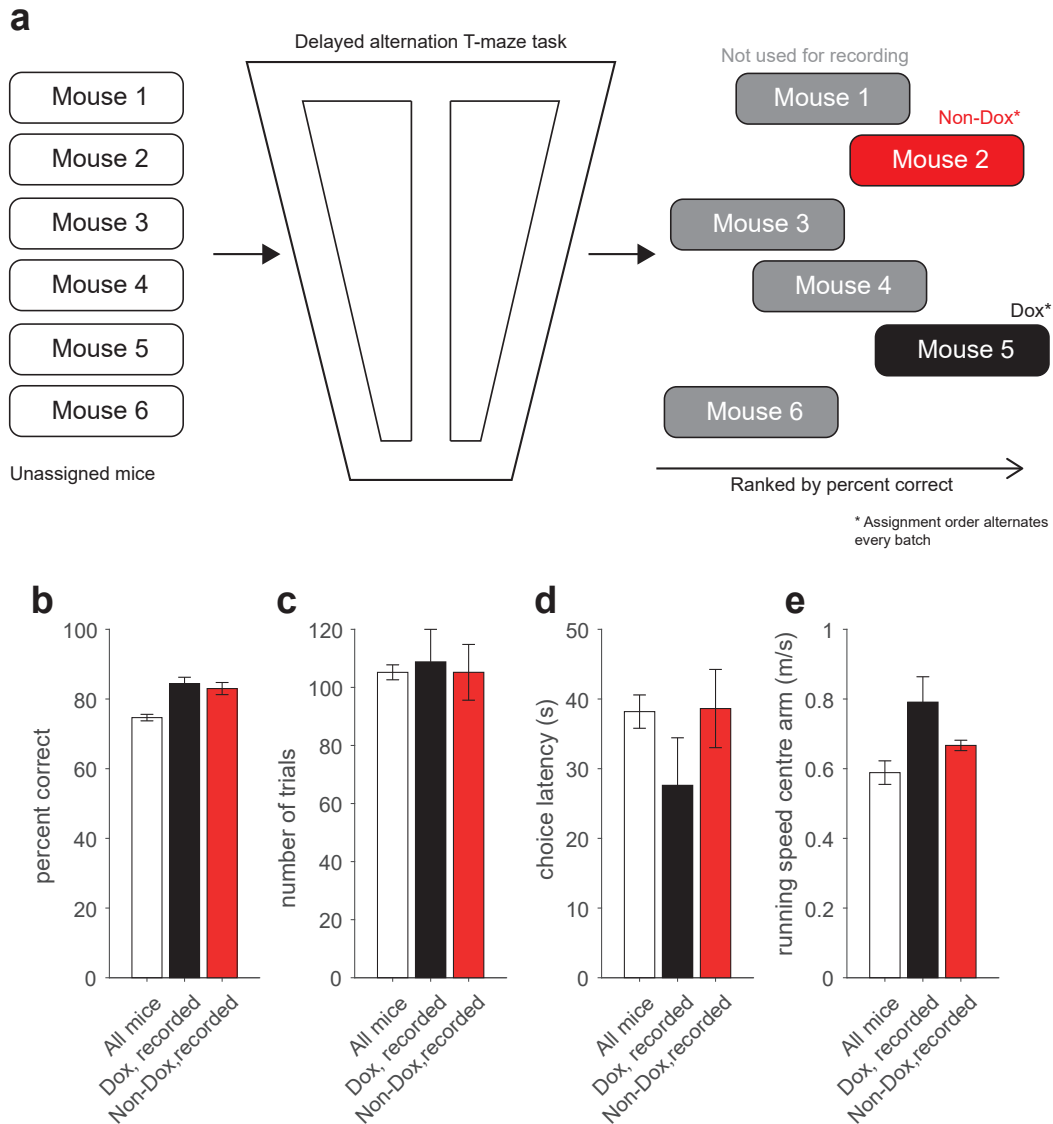


Figure 3.2: Dox and Non-Dox group assignment. (a) Mice were assigned to Dox and Non-Dox groups based on ranked performance in a delayed alternation T-maze task. (b) Group assignments were made to ensure performance was similar in Dox and Non-Dox groups (c) Number of trials completed by mice in each group (d) Choice latency (time to reach choice zone) in Dox and Non-Dox mice. (e) Running speeds on the T-maze in Dox and Non-Dox mice.

Non-Dox: $M=38.6s$, $n = 5$ Fig. 3.2d) and running speed ($t(8) = -1.67$, $p = 0.1330$, Dox: $M=0.794m/s$, $n = 5$, Non-Dox: $M=0.669m/s$, $n = 5$ Fig. 3.2e).

Following Dox assignment at 3 months, mice were kept in their home cages, housed with batch mates and with access to running wheels, without any further experiments until probe implantation surgery.

3.2 Surgery

The surgery protocol was similar to that outlined in Chapter 2, and surgeries were performed at approximately 5 months of age. All surgeries were performed by Anthony Blockeel. The probes were pre-mounted onto a 3d printed casing for the drives (CAD rendering can be seen in Fig. 3.3a). Figure 3.3b shows example electrode tracks.

The probe was implanted in V1 at 2.7mm lateral to and 0.5mm anterior to lambda and in CA1 at 2.0mm lateral 1.86mm anterior to lambda. The CA1 probes were implanted around 700-800 microns down and the V1 probes around 500-700 microns down - as the probes were pre-attached to the drive housing, placement could not always be exact. Probes were P-series probes provided by Cambridge Neurotech, with 16 sites on each shank arranged as seen in Figure 3.3a. Vertical spacing between sites was 25 microns, with a total span of 200 microns across the shank, and horizontal spacing was 22.5 microns. Shanks on the same probe were 250 microns apart.

Mice were singly housed following surgery due to the risk of the plastic drive housing and connector being chewed, but were given free access to running wheels.

Following post-surgery recovery with DietGel and gummy supplements, mice were food deprived to the same protocol as Ch. 2, i.e. maintenance of body weight at $\geq 85\%$ of ad libitum weight.

3.3 Recording

Recordings were carried out using Plexon acquisition equipment and software, which recorded wideband (40 000 Hz) and field potential (1000 Hz) signals separately.

The CA1 drive was advanced at a rate of 100 microns a day until ripples and cells were visible on the shank. Ripple detection methods can be seen in Chapter 4.

The mouse was head-fixed on a polystyrene running wheel surrounded by 3 square 19 inch screens (iiyama ProLite E1980SD), one on the centre and one on the left and right, with each screen approximately 32 cm away from the head fixation

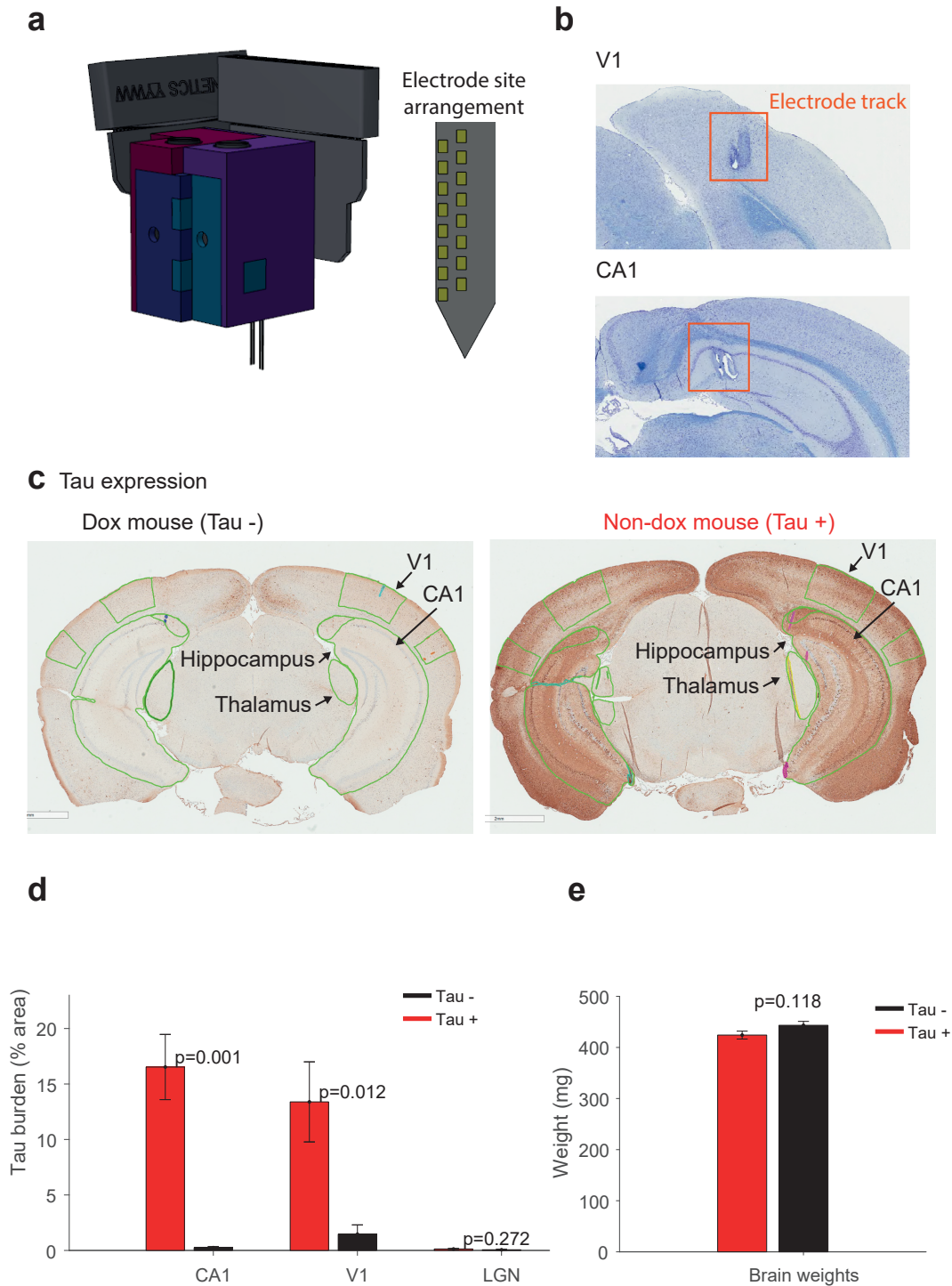


Figure 3.3: Confirmation of histology and electrode placement. (a) An illustration of the 3D-printed drive and probe housing constructed by Lilly Engineering (b) Example confirmation of electrode placement in V1 and CA1 (c) Tau expression was measured using PG-5 immunohistochemistry. All histology was performed by the Lilly histology department. (d) Tau burden (measured by % area with positive PG-5 staining) was significantly higher in CA1 and V1 in Non-Dox (Tau +) mice and lower in Dox (Tau - mice) with negligible tau expression in LGN. (e) Brain weights (in mg) were not significantly different at this timepoint.

point. The screen edges were touching so that excepting the screen bezels, the three screens made one continuous stimulus presentation zone. In total, the screens spanned approximately 200 degrees of visual angle horizontally and 60 degrees of visual angle vertically. Videos of the mouse's right eye were recorded using an infrared light and camera for future pupil size analysis. Each mouse was recorded from for a maximum of 3 hours per day.

There was also a lick detector and reward valve apparatus which was positioned by the mouse's mouth during closed loop running and running in the dark. During other experiments, this apparatus was moved out of the way.

The experimental area was darkened using blackout material surrounding the entire rig and covering all equipment lights so that the only light visible came from the screens on which the experiments were presented.

Occasionally, the sparse noise mapping on any given day would indicate that the V1 receptive field positions overlapped with the screen bezels rather than sitting squarely in the centre of one of the screens. If this was the case, the mouse and wheel apparatus was rotated so that its nose was facing the bezel of the leftmost and centre screen, which brought the receptive field position back onto a presentation screen.

All stimulus presentation code was written in MATLAB (Mathworks) and adapted from code used by Kenneth Harris and Matteo Carandini's lab.

3.4 Visual protocols

An overview of drifting grating visual protocols can be found in Table 3.1. All drifting gratings were presented on a gray screen background. Mice were also presented with a full screen flash stimulus lasting 1s with an ISI of 2s. For this protocol the screen was dark during the ISI.

A sparse noise movie was also presented which lasted 15 minutes in total and consisted of a 5 minute movie repeated 3 times. Black and white squares with side length of 8 degrees were presented in a random pattern (determined by a random seed) on the screen, with random onset times, and all other squares on the screen

were gray forming a uniform gray background. Each black or white square was on the screen for 10 frames - as the monitor refresh rate was 60Hz this was around 167ms. 98% of total presented squares during the entire movie were gray background squares.

Every day, for each mouse that was put on the wheel, the sparse noise movie was run first and receptive field mapping for the V1 LFP was run online, while the mouse was still on the wheel. Following this, the optimal location for stimulus presentation for that day was determined, and based on orientation preference of neurons that had been recorded from on the previous day on the same mouse, a preferred orientation was also selected for all the drifting grating stimuli. The orientation protocol was also run daily. After this, a selection of drifting grating protocols would be run until the mouse had completed all visual protocols. Once all protocols were complete, the V1 drive would be advanced slightly (100 microns) and all protocols would be repeated. Pre-adaptation, adaptation and post-adaptation blocks were always run together, with a 5 minute gray screen recovery period between the adaptation and post-adaptation block.

3.5 VR protocols

The VR environment was a 120cm long corridor which was repeated every trial. The walls, ceiling and floor had a white noise pattern with vertical grating patterns located at 20cm and 60cm, and plaid patterns at 40cm and 80cm. These vertical grating and plaid patterns were 8cm wide. Further details of the VR environment can be found in Saleem et al. (2013) and Saleem et al. (2018). The trial timed out if the mouse failed to complete it within 30s, and the mouse was limited to performing 120 trials maximum in a session.

Mice were acclimatised to VR protocols while the drive was advanced to CA1 by running them in the environment described above, in a closed loop condition where the mouse running speed determined the speed of their movement through the virtual environment. Mice were rewarded at random locations on the track with drops of Ribena delivered via a reward valve. I set the volume of the reward de-

Protocol	Stimulus duration (s)	ISI (s)	Repeats per stimulus	Contrast (%)	Outer Diameter (deg)	Inner Diameter (deg)	Orientation (deg)	Temporal Frequency (Hz)	Spatial frequency (cpd)	Adapt stimulus duration (s)
Orientation	1.5	2.5	10 (some-times 20)	100	35	0	[0:30:330]	2	0.04	-
Pre adaptation	1	4.4 (gray screen)	20	100	35	0	[0:30:330]	2	0.04	30
Adaptation	1	4.1 (adapt stim)	20	100	35	0	[0:30:330]	2	0.04	30
Post adaptation	1	4.4 (gray screen)	20	100	35	0	[0:30:330]	2	0.04	30
Size x temporal frequency	1	2.5	20	100	[0, 4, 12, 20, 28, 36, 44, 52]**	0	*	[1, 2, 4, 8]**	0.05	-
Temporal frequency	3	2.5	20	100	35	0	*	[0.5, 1, 2, 4, 8]	0.05	-
Contrast	1.5	2.7	20	[6, 12, 25, 50, 75, 100]	35	0	*	2	0.04	-
Spatial frequency	1.5	2.5	20	100	35	0	*	2	[0.01, 0.02, 0.04, 0.08, 0.16, 0.32]	-
Surround and Centre	1	1.3	100	100	[200, 500, 500]**	[0, 200]***	0, *	2	0.08	-
Size	1	1.3	20	100	[0, 2, 12, 20, 28, 36, 44, 52]	0	*	2	0.04	
Annulus Size	1	1.3	20	100	50	[0, 5, 10, 20, 30, 40]	*	2	0.08	

Table 3.1: Details of all drifting grating visual protocols.

* Orientation for these protocols was based on preferred orientation distributions from cells recorded on the previous day

** All combinations of size x temporal frequency parameters were presented in this protocol

*** For Surround and Centre protocol, 3 different stimuli were presented. The parameter values are for stimulus 1, 2, and 3 in order.

pending on the mouse, and during acclimatisation to VR, extra Ribena rewards were sometimes also given so the mouse might have more than one reward in a track. Training was considered complete when the mouse was able to run approximately one whole session (120 trials) within 20 minutes, although this was not a strict limit. Not all mice were motivated by the Ribena reward, but all of them successfully reached the training criterion.

When mice had completed training and the CA1 drive was in the cell layer, mice also ran the open loop and dark conditions. In the open loop condition, the VR environment was visually identical to what was described in the closed loop condition, but instead of movement in the virtual environment being controlled by mouse running speed, the virtual environment was a replay of one of the mouse's previous runs in closed loop, like viewing a movie. Therefore in open loop, the mouse running speed did not affect the virtual environment at all. The mouse was not given rewards in the open loop condition because reward was tied to position in the virtual environment rather than running speed, and having rewards while not moving sometimes confused them - when rewards were given in open loop, they stopped running as much not just in the open loop condition, but also in the closed loop and dark conditions. This lack of reward may have led to motivational or behavioural state differences in the mice in the open loop condition, but I judged that these were less important than ensuring that the mouse ran sufficient numbers of trials in all three conditions.

In the dark running condition, the same code was used to run the experiment as in the closed loop condition, so mice were still rewarded in random positions in each trial, but all computer screens were turned off and the mouse was in complete darkness.

VR sessions continued to be acquired as long as cells were still present on the CA1 probes.

3.6 Histology and tau burden confirmation

Mice were culled by perfusion at 6.5 months by a Lilly colleague and brains were removed for histology. Methods used were identical to Blackmore et al. (2017).

All histology was performed by the Lilly histology department. Mouse brains were sectioned and checked for electrode tracks (Fig. 3.3b) and tau pathology was assessed by PG-5 immunohistochemistry (Fig. 3.3c). Tau was significantly increased in CA1 and V1 (CA1: $t(8) = 5.54, p < 0.001$, Dox: $M = 0.2492$, $SD = 0.2133$, $n = 5$ Non-Dox: $M = 16.5298$, $SD = 6.5700$, $n = 5$. V1: $t(8) = 3.22$, $p = 0.0123$, Dox: $M = 1.4653$, $SD = 1.8741$, $n = 5$ Non-Dox: $M = 13.3873$, $SD = 8.0694$, $n = 5$.) with no difference in LGN ($t(8) = 1.18$, $p = 0.2718$, Dox: $M = 0.061$, $SD = 0.102$, $n = 5$, Non-Dox: $M = 0.133$, $SD = 0.090$, $n = 5$.) in Non-Dox mice, as expected (Fig. 3.3d). Brain weights were also unchanged (Fig. 3.3e, $t(8) = -1.75$, $p = 0.1176$, Dox: $M = 443\text{mg}$, $SD = 17.2\text{mg}$, $n = 5$, Non-Dox: $M = 424\text{mg}$, $SD = 17.3\text{mg}$, $n = 5$.). This histology analysis confirmed that Dox mice (called Tau - mice in the rest of the thesis) had minimal tau pathology and Non-Dox mice (called Tau + mice in the rest of the thesis) had elevated tau pathology in the expected forebrain areas.

Chapter 4

Effects of tauopathy on local field potential activity

4.1 Introduction

In this chapter, I focus on changes neural activity reflected in the local field potential (LFP) in CA1 and V1 of Tg4510 mice, primarily looking at changes in power spectra. In particular, I explore the basic power spectrum and investigate changes in LFP power in response to different cues, such as mouse running speed and visual stimuli. The aim of these analyses was to establish whether there were any evoked responses in the power spectrum which were more sensitive to early tauopathy than overall power spectrum changes.

4.1.1 LFP power spectrum changes in Tg4510 mice

As seen in Chapter 2, LFP power in Tg4510 mice decreases across the entire frequency spectrum as tauopathy progresses, in cortex and hippocampal areas. Reduced power has also been observed in entorhinal cortex (Booth et al., 2016), and in hippocampus, ripple power during sleep (Witton et al., 2014) and evoked theta in slice (Scott et al., 2016). However, most of these changes emerge only at a late stage of tauopathy (7+ months) where there has already been a significant amount of neuronal death and atrophy (Blackmore et al., 2017; Ramsden et al., 2005; Spires et al., 2006; SantaCruz et al., 2005). Given this, the power changes seen at later stages may reflect the downsized neural population rather than specific functional

changes.

As I investigated a slightly earlier timepoint, the changes in LFP in my analyses might reflect early functional changes related to tau accumulation, rather than late stage neuronal death. As previous work by my collaborators (see Ch. 2) have shown, changes in overall power can be observed around 6 months within CA1 in the beta, theta and high gamma ranges, but there are no changes in power in cortex. Menkes-Caspi et al. (2015) also observed a slight elevation of power at lower frequencies around this timepoint.

Other work by my collaborators (unpublished, from Lilly Pharmaceuticals) also found a decrease in the amplitude of auditory evoked potential components at late timepoints, mirroring similar ERP decreases in Alzheimer's patients (Polich et al., 1990). Again, I wanted to understand whether this was specific to late tauopathy or whether similar changes could be detected in my mice at an earlier timepoint in a primary sensory area relevant to the stimulus.

4.1.2 V1 gamma

Recent work by Saleem et al. (2017) has shown that there are two distinct types of gamma in V1, narrowband gamma ($\sim 60\text{Hz}$) which originates from LGN and retina, and broadband gamma (30-90Hz) which reflects local activity within the cortex. These two varieties of gamma have distinct responses to certain types of visual stimulus (changing contrast or size), where broadband gamma increases as contrast or size increases, and narrowband gamma decreases. Understanding how these types of gamma activity change in Tau+ mice would indicate broadly whether tauopathy in V1 affects primarily local inhibitory activity (broadband gamma) or input from other areas (narrowband gamma), or indeed both.

4.1.3 CA1 theta

Theta in CA1 is prominent when an animal is engaged in a task or active, particularly when running (Vanderwolf, 1969) and theta power has been shown to correlate with running speed (Wyble et al., 2004). This locomotion-related theta is driven by a disinhibitory septo-hippocampal circuit (Fuhrmann et al., 2015). CA1 theta is also

directly involved in controlling the running speed of the animal via a subcortical pathway (Bender et al., 2015).

Speed-related changes in theta oscillations, particularly in theta frequency, have been shown to be similar in closed loop virtual reality to real world running (Chen et al., 2018). Therefore, the power-speed relationship may be similar in closed loop VR to real world running. In open loop environments or running on a running wheel, where mouse speed and visual speed are dissociated, or when the mouse is running in the dark, the relationship between theta frequency and running speed is flattened, and theta power is somewhat reduced (Chen et al., 2013; Czurkó et al., 2001). In other work from our lab, a flattening of the theta power-speed relationship has also been observed in open loop and dark running (Saleem et al. unpublished). This suggests that CA1 theta does not encode running speed per se, but relies on integration of different kinds of sensory input, perhaps in order to create a spatial representation.

Given that spatial information is known to be disrupted in CA1 in Tg4510 mice (Cheng and Ji, 2013), I wanted to investigate whether related changes could be seen in the CA1 theta-speed relationship.

4.2 Methods

4.2.1 Preprocessing

Before comparing LFP characteristics between the groups, I first identified layer 4 in V1 and the cell layer in CA1. I did this because power in certain frequency bands can vary substantially depending on where the recording site is. For example in V1, narrowband gamma is higher in layer 4 than surrounding layers (Saleem et al., 2017), as is also seen in Figure 4.1d, and in CA1, theta power and ripple power are highest in the cell layer. We did not perform post-mortem lesions. Also, as the electrodes were thin, the electrode track were often not visible in the post-mortem histological slices. Therefore, we identified putative layer 4 in V1 and cell layer in CA1 based on their electrophysiological signatures.

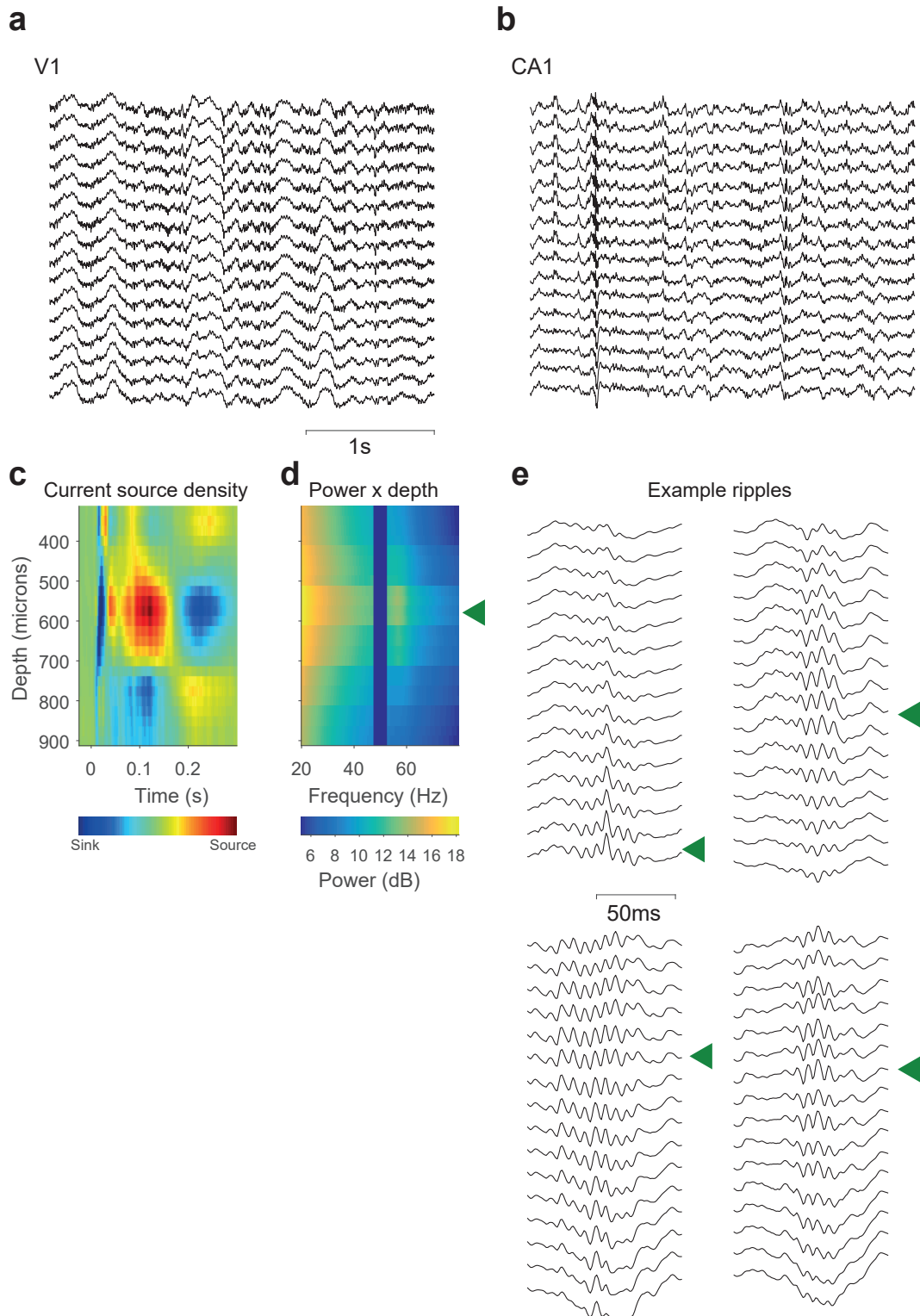


Figure 4.1: Identification of L4 in V1 and cell layer in CA1. Example raw traces from single shanks in V1 (a) and CA1 (b). (c) Layer 4 in V1 was identified by performing a current source density (CSD) analysis to find the location of the first current sink following onset of a full screen flash stimulus. Current source density was calculated separately for each side of each shank in V1. (d) As additional confirmation of L4 location, and to find L4 in mice where CSD based identification failed, L4 was also identified by finding the narrowband gamma peak in power spectra in V1 sorted by depth. (e) Cell layer in CA1 was identified by finding maximum ripple power in the raw traces during ripple events.

4.2.1.1 Finding layer 4 in V1

In V1, I identified L4 by using a combination of current source density (CSD) and plotting power by depth. Because the probes were moved through the different layers over time, and had different starting depths due to either the variability in initial implantation depth or brain movement following surgery, the probe was in L4 only in a subset of all recording sessions for each mouse.

CSD analysis was performed by first taking all full screen flash protocols (details in Chapter 3, under 'Visual protocols') run for a single mouse, and finding the event-related potential (ERP) for every channel on all V1 shanks during each recording. Approximate channel depth in microns for every electrode site was then calculated by combining depth information about the shank tip from surgical notes and drive movement history, with electrode spacing information (25 microns between each site on a single side of a shank). A depth profile of ERPs could then be constructed from the multiple full screen flash sessions, by taking the mean of all ERPs at a given depth, even when channels were recorded from during different sessions. Once the ERP depth profile had been constructed, I then calculated the CSD using the cubic spline method (Pettersen et al., 2006). Layer 4 could then be identified in the CSD by looking for the first current sink after stimulus onset (see Fig. 4.1c for an example).

Using CSD analysis, I was able to identify L4 successfully in 7/10 mice. 2 of the mice where L4 identification failed were mice for which I did not move the V1 drive enough to be able to create a depth profile spanning sufficient depth. This was due to these 2 mice being the first pair I was recording from as I made the decision to advance the V1 drive between full repeats of all protocols only after recording from these mice. The other mouse had not had full screen flash protocols run at all drive depths, as I had moved the V1 probe before CA1 drive movement in order to find V1 cells for unit recordings.

In order to get L4 identification for these remaining three mice, and to double check L4 position in the other mice where L4 identification had been successful using CSD, I also looked at power by depth. Power by depth profiles were calculated

from sparse noise sessions which were run daily. This gave me more sessions to analyse, and more depths to look at for the one mouse where the flash protocol had not been run at all V1 depths. Spectra were calculated from sparse noise sessions using the Chronux toolbox to generate power spectra for 3s chunks of data with a 1s overlap, with [5 9] tapers. Mean spectra for each depth were then calculated using the same method as described above for ERPs, and power could then be visualised across various depths in V1 (Saleem et al., 2017), as shown in Figure 4.1d. As narrowband gamma power is known to be higher in L4 compared to other layers of V1, I looked for a narrowband gamma peak in the power by depth profile.

Using this combination of methods, I was able to identify L4 in all 10 mice, although the quality of the identification differed quite substantially depending on the mouse. The two mice where identification was least reliable were again the first two mice I recorded from, as there was not enough drive movement to get a proper depth profile using either CSD or power by depth profiles. I decided to include these mice despite their poor L4 identification as, apart from the difference in narrowband gamma power, spectral properties are relatively similar across all layers of V1, so only analyses of narrowband gamma would be affected. Furthermore, narrowband gamma power is not necessarily entirely absent in other layers of V1, rather power is reduced. Thus, analyses which focused on changes in narrowband gamma power from a baseline (e.g. the stimulus-evoked changes in Fig. 4.7d and Fig. 4.8d), rather than overall changes in power, should not be affected by including these mice. Lastly, of the two mice with poor L4 identification, one was in the Tau+ group and one was in the Tau- group, so there was no group-dependent bias in bad L4 identification.

4.2.1.2 Finding the cell layer in CA1

When finding channels to use in CA1, I first excluded all days during which the drive was moving towards CA1. While I was recording from the mice, I assessed daily whether the probe had reached the cell layer by looking for signs of ripples, either in the raw trace during acquisition, or using the ripple detection method described below after finishing the recordings for that day. Once the drive had reached

the cell layer and the cell layer was positioned approximately in the middle of a shank, I then stopped moving the drive if CA1 units were present, but would move the drive a little if no units could be observed.

To find the cell layer in CA1, I used a ripple detection method similar but not identical to the method outlined in Sullivan et al. (2011). In the first stage of ripple detection, the raw LFP trace for each channel was band-pass filtered from 120Hz to 220Hz, and took the magnitude of the Hilbert transform of the band-pass filtered signal. This magnitude signal was then normalised by using z-score, and potential ripple events were identified as times when the z-score exceeded 1 (i.e. the instantaneous power was at least 1SD greater than the mean). Events were rejected if they were too short ($< 25\text{ms}$) or too long ($> 150\text{ms}$), or if the peak power during the event interval, as determined by the z-scored Hilbert transform described above, was less than 2 standard deviations greater than mean power.

In the second stage, I took a 100ms window around the peak instantaneous power of each event and calculated the power spectrum for this window for each event, using the original LFP signal high-pass filtered to $> 70\text{Hz}$. These power spectra were then smoothed using a Gaussian filter. The power spectrum for each event was then examined to ensure it met two conditions - first, that the peak in the power spectra was between 140Hz and 220Hz, and secondly, no value in the spectrum above 260Hz was greater than 0.5x the peak of the power spectrum. This helped to eliminate many non-ripple noise events, as power in the noise events was generally elevated across the spectrum rather than having a specific peak like ripple events.

I then manually checked the results of ripple detection to find the CA1 cell layer in each mouse. This was done by identifying the channel with the largest ripple amplitude during ripple events. The cell layer could be identified in 8/10 mice, and for the two mice where the cell layer could not be identified, I was also unable to find CA1 during the course of recording and drive movement. Most mice had a consistent cell layer location across all recording days, but some mice had different cell layer locations, as determined by ripple detection, across days or weeks, so I

selected the best electrode site for cell layer location on a day-by-day basis.

4.2.1.3 Finding best V1 channels for power over time analysis

To pick channels for the power over time analysis, I found the V1 cortical depth that occurred most often in sparse noise sessions, which were run daily, for each mouse individually. I did not look at CA1 channels for this analysis.

4.2.2 Analysis methods

4.2.2.1 Power spectra

To look at differences in power spectra between Tau+ and Tau- mice in virtual reality running, I took each VR session that had L4 identified in V1, divided the LFP signal for the L4 channel into 3s bins, with 1s overlap, and calculated the power spectrum for each bin using the multitaper spectrum from Chronux, using tapers [59]. I did the same for each VR session that had the cell layer identified in CA1. For the power over time analysis, I did the same multitaper spectra with 3s bins on sparse noise sessions, for channels picked to span the longest amount of time as described above.

For all power spectra, a noise band around 50Hz was excluded (47.5Hz - 52.5Hz), apart from normalised spectrograms for looking at stimulus-triggered changes, where the noise band used for exclusion was broader (45-55Hz).

4.2.2.2 Mouse running speed

For our VR sessions, I calculated mouse running speed from the rotary encoder measurements recorded by the Plexon acquisition system - from the diameter of the running wheel (17.78cm), and the number of rotary encoder pulses per full turn of the wheel (1024 pulses), I calculated the distance travelled by the mouse during each 3s bin, and hence its mean speed during the 3s bin.

4.2.2.3 Power over time

I used all running speeds (0-60cm/s) for the power over time analysis.

A mouse age category for each daily session was calculated by rounding actual age in days to the nearest 0.5 months, and the mean spectrum for each timepoint (5

months, 5.5 months and 6 months) was calculated by averaging all the spectra from sessions in that age category.

Changes in power were then calculated by dividing the spectra at 5.5 months and 6 months by the spectrum at 5 months for each mouse.

4.2.2.4 Visually evoked potential

The visually evoked potential (VEP) was calculated from flash protocol sessions (flash duration, 1s, ISI duration, 2s), using the previously identified V1 and CA1 channels as described above. VEP was calculated as the mean of the raw LFP within a window -0.5s prior to and 1s after the stimulus onset for all stimulus presentations across all sessions, for each mouse separately.

4.2.2.5 Stimulus-triggered changes

Spectrograms for each stimulus type within a session were obtained using a window size of 1s with a step of 0.05 seconds and tapers of [3 5]. The spectrogram was then normalised to the baseline period (-0.5s to stimulus onset) by calculating the mean power at each frequency during this baseline period from the spectrogram, and subtracting this mean baseline power from the entire spectrogram.

Broadband (20-90Hz, excluding narrowband range and noise range) and narrowband gamma power (55-65Hz) for each stimulus was calculated by taking the mean power across frequencies in that range during a response window of 0.5-1s after the stimulus was presented.

4.3 Results: Power spectra differences in Tg4510

I first wanted to understand whether there were basic differences in power spectra between Tau+ and Tau- mice, as has previously been described in the model. Previous work by other researchers at Eli Lilly (see Chapter 2) showed no difference in power between Tau+ and Tau- mice at any frequency at the 4 month timepoint in CA1. However at the 6 month timepoint they observed a significant decrease in power in Tau+ mice at beta (15-30Hz) and gamma (30-120Hz), a minor (but not significant) decrease in power in the theta (6-12Hz) band and no difference in the ripple band. As our mice were recorded from between 5-6.5 months, Tau+ mice

should display small, but not necessarily significant, decrease in power across a broad range of frequencies (6Hz-120Hz) in CA1.

The previous study by our collaborators did not investigate power in V1, but power in another cortical area, the prefrontal cortex, was not significantly different between the groups at 6 months and even at 8 months, where pathology is quite advanced, only very minor changes in the low gamma range (30-60Hz) were observed. This suggested that there should not be any significant power spectra changes in V1 of our Tau+ mice.

The aim of looking at power spectra in the Tau+ mice at this timepoint was therefore not only to understand whether there were any significant differences between the groups and whether these agreed with previous results, but also to go beyond the basic power spectrum that had been analysed in previous studies and explore the relationship between power and different behavioural and environmental factors - in my experiments the most interesting ones were running speed and visual stimulus features.

4.3.1 Basic differences in power spectra

As Tau+ mice are known to have elevated locomotor activity in real world running (Blackmore et al., 2017), I wanted to ensure power spectra differences between the groups were not driven by running speed. In order to do this, I categorised mouse running speed into four categories - stationary (0-5cm/s), low (5-15cm/s), medium (15-30cm/s) and high (30-50cm/s) speed (Fig. 4.2a). I then calculated individual mouse power spectra using only time bins during which the mouse was at medium speed during closed loop VR running, and calculated grouped mean spectra for V1 (Fig. 4.2b) and CA1 (Fig. 4.2c) from these selected time bins. Surprisingly, instead of the decrease in beta and gamma power found in previous work, I found that in CA1, power was decreased at high frequencies (> 147 Hz) only (t-test at every frequency, maximum $t: t(6) = 3.29$ and $p < 0.05$ for all t-tests above 147Hz, Tau+: $n = 4$, Tau-: $n = 4$). In fact at some lower frequencies, notably theta (6-12Hz) in CA1, Tau+ mice appeared to show a small increase in power (Fig 4.2e), but this was not significant (maximum $t: t(6) = -0.4438$ and $p > 0.15$ for all frequencies

between 6 and 12 Hz, Tau+: $n = 4$, Tau-: $n = 4$). In V1, there were no significant differences in power at any frequency, although Tau+ mice appeared to have a minor reduction in power at high frequencies, at a frequency range similar to the decrease in CA1. There was no significant difference (maximum t : $t(6) = 1.10$ and $p > 0.3$ for all frequencies between 55 and 65 Hz, Tau+: $n = 4$, Tau-: $n = 4$) in power in V1 narrowband gamma, our other frequency band of interest (Fig 4.2d).

4.3.2 Relationship between power and speed for V1 narrowband gamma and CA1 theta

Although there was not a difference in CA1 theta power (Fig 4.2c) or V1 narrowband gamma power (Fig 4.2b) when mice were running at a medium speed in closed loop, I wanted to understand whether there were differences between the groups in CA1 theta and V1 narrowband gamma power when the running speed of the mouse changed. An additional question with CA1 theta power was to understand whether the relationship between theta power and running speed changed in Tau+ mice when mouse running speed was decoupled from the visual environment. In such environments, for example wheel running, running in the dark, or open loop virtual reality environments, the relationship between CA1 theta and running speed should be somewhat different to closed loop running, which is more similar to real world scenarios (Czurkó et al., 2001; Chen et al., 2018, and Saleem et al., unpublished). As Tg4510 CA1 neurons contain less spatial information than WT neurons (Cheng and Ji, 2013), CA1 theta in the Tau+ mice might be less influenced by spatial information, and so the relationship between power and speed might be more similar between closed loop and non-navigable open loop and dark conditions.

Normal wildtype mice also show increased narrowband gamma power with running speed (Saleem et al., 2017). As the LGN (the source of V1 narrowband gamma) was not affected by tau pathology in my mice (Fig. 3.3d), Tau+ mice should not show any difference in this speed-power relationship. Furthermore, as narrowband gamma in V1 has been shown to be absent when mice are in the dark (Saleem et al., 2017), there should not be narrowband gamma in Tau+ mice in the dark condition regardless of running speed. However, I was not sure what to expect

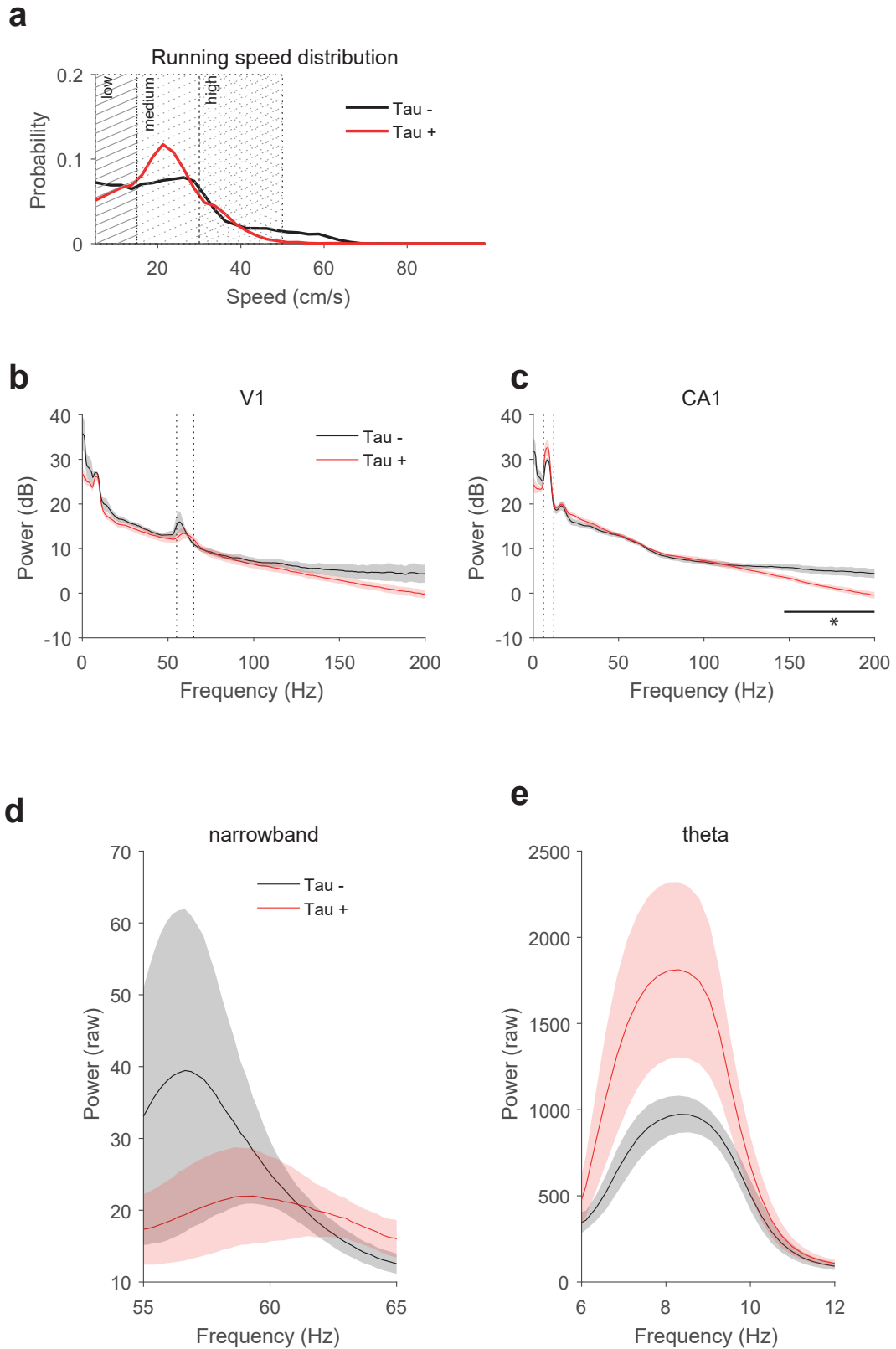


Figure 4.2: Tau+ mice show differences in power across multiple frequency bands. (a) Normalised running speed distributions for Tau+ and Tau- mice, from sessions with good CA1 cell layer identification and after VR training was complete. Running speed was slightly different across the groups. **(b) and (c)** Power spectra in Tau+ and Tau- groups was calculated from 3s bins during which the mice were running at a medium speed (15-30cm/s) in closed loop condition, to eliminate running speed dependent group differences. Power at high frequencies (> 147Hz) was reduced in Tau+ mice in CA1. **(d)** Zoom of narrowband gamma power in V1. **(e)** Zoom of theta power in CA1.

in V1 narrowband gamma in the open loop condition, but I ran a similar analysis to the one conducted for CA1 theta to explore any group differences.

4.3.2.1 V1 narrowband gamma power

I began by looking at mean group spectra during all running speeds - stationary, low, medium and high - in closed loop (Fig 4.3a), particularly focusing on narrowband gamma (Fig. 4.3b). To quantify differences between the groups, I looked at two measures: power when the mouse was stationary (Fig 4.4d) and the slope of the power/speed relationship (Fig. 4.4f), which was calculated individually for each mouse. Mean power-speed relationships for each group are shown in Figure 4.4e. In closed loop running, there was no significant difference between Tau+ and Tau- mice in either stationary power ($t(4) = -1.03$, $p = 0.3616$, Tau-: $M = 13.1$, $SD = 1.08$, $n = 2$, Tau+: $M = 21.2$, $SD = 10.5$, $n = 4$) or in the slope of the power/speed relationship ($t(6) = 0.518$, $p = 0.6229$, Tau-: $M = 23.7$, $SD = 11.6$, $n = 3$, Tau+: $M = 17.3$, $SD = 19.90$, $n = 5$).

Looking at the open loop and dark conditions, there was also no significant difference between Tau+ and Tau- mice for stationary narrowband power in open loop ($t(4) = -2.31$, $p = 0.0816$, Tau-: $M = 10.5$, $SD = 3.87$, $n = 3$ Tau+: $M = 18.8$, $SD = 4.78$, $n = 3$, again in Fig 4.4d) or speed-power slope for either open loop or dark running ($t(4) = -1.54$, $p = 0.1993$, Tau-: $M = 0.268$, $SD = 5.39$, $n = 3$, Tau+: $M = 8.33$, $SD = 7.31$, $n = 3$, $t(3) = -0.333$, $p = 0.7608$, Tau-: $M = 1.52$, $SD = 0.30$, $n = 2$, Tau+: $M = 4.40$, $SD = 11.6$, $n = 3$, again in Fig 4.4f). There was no group measurement for narrowband power while stationary in Tau+ mice because the mice were not stationary long enough to meet the minimum time requirements for inclusion in the analysis, but speed/power relationships could be calculated from remaining low, medium and high measurements.

There was also no significant difference between the closed and open loop conditions in either Tau+ mice (paired t-test: $t(2) = 1.01$, $p = 0.4199$, closed: $M = 20.4$, $SD = 26.2$, open: $M = 8.33$, $SD = 7.31$, mice $n = 3$) or Tau- mice ($t(2) = 3.36$, $p = 0.0781$, closed: $M = 23.7$, $SD = 11.6$, open: $M = 0.268$, $SD = 5.39$, mice $n = 3$), or between closed and dark (Tau+: $t(2) = 0.897$, $p = 0.4645$, closed: $M = 20.5$,

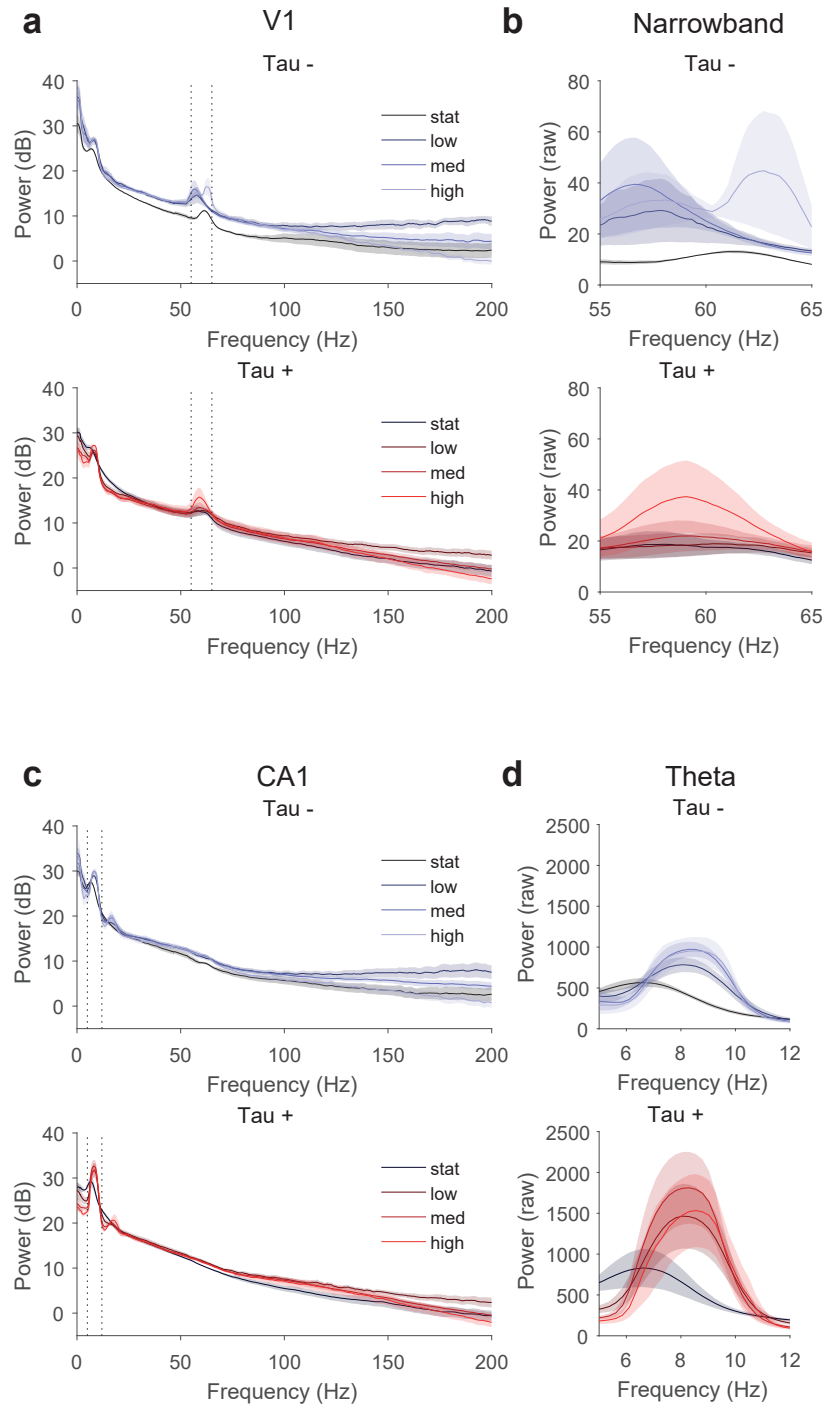


Figure 4.3: Power spectra at different running speeds in closed loop condition. (a) and (c) Tau+ and Tau- mean spectra at stationary (0-5cm/s), low (5-15cm/s), medium (15-30cm/s) and high (30-50cm/s) running speeds in closed loop. (b) Zoom on V1 narrowband gamma power showing all running speeds (d) Zoom on CA1 theta power showing all running speeds

$SD = 26.1$, dark: $M = 4.4$, $SD = 11.6$, mice $n = 3$, Tau-: $t(1) = 1.962$, $p = 0.3001$, closed: $M = 24.5$, $SD = 16.3$, dark: $M = 1.52$, $SD = 0.299$, mice $n = 2$).

In summary, there were no changes in narrowband gamma due to running speed in V1 of Tau+ mice. Tau+ and Tau- mice had similar narrowband gamma power in V1, and the relationship between running speed and V1 narrowband gamma power was the same in Tau+ groups.

4.3.2.2 CA1 theta power

I repeated the same analysis as above for CA1 theta power, starting again with the power spectra in closed loop running (Fig. 4.3c), focusing on theta power (Fig. 4.3d). As at medium speed (Fig. 4.2e), theta power in Tau + and Tau - mice was similar at high and low speeds.

Similarly to the V1 narrowband gamma analysis, I then looked at stationary power and speed/power slopes for CA1 theta in closed, open and dark conditions. During stationary periods (Fig 4.4a), there was no significant difference in theta power between the groups in any of the three conditions (closed: $t(5) = -1.09$, $p = 0.3274$, Tau+: $M = 838$, $SD = 489$, $n = 3$, Tau-: $M = 570$, $SD = 125$, $n = 4$, open: $t(5) = -1.76$, $p = 0.1391$, Tau+: $M = 786$, $SD = 225$, $n = 3$, Tau-: $M = 579$, $SD = 77.6$, $n = 4$, dark: $t(3) = -2.23$, $p = 0.1123$, Tau+: $M = 1.03e + 03$, $SD = 388$, $n = 2$, Tau-: $M = 576$, $SD = 29.6$, $n = 3$). The slope of the speed/power relationship was significantly different between closed and open loop in the Tau- mice (paired t-test: $t(3) = 3.9021$, $p = 0.0299$ closed: $M = 543$, $SD = 578$, $n = 4$, open: $M = -91.6$, $SD = 466$, $n = 4$), as expected, but there was no significant difference between closed loop and dark conditions for Tau- mice ($t(3) = 2.28$, $p = 0.1068$, closed: $M = 543$, $SD = 578$, $n = 4$, dark: $M = -69.6$, $SD = 658$, $n = 4$). Within the Tau+ mice, there was no difference between the slope of the speed/power relationship either in closed loop and open loop ($t(3) = 1.86$, $p = 0.1591$, closed: $M = 900$, $SD = 496$, $n = 4$, open: $M = 615$, $SD = 617$, $n = 4$), or in closed loop and dark conditions ($t(3) = 0.816$, $p = 0.4743$, closed: $M = 900$, $SD = 496$, $n = 4$ dark: $M = 647$, $SD = 195$, $n = 4$). In addition, there were no significant differences between Tau+ and Tau- mice in speed/power slope in any of the conditions (Fig

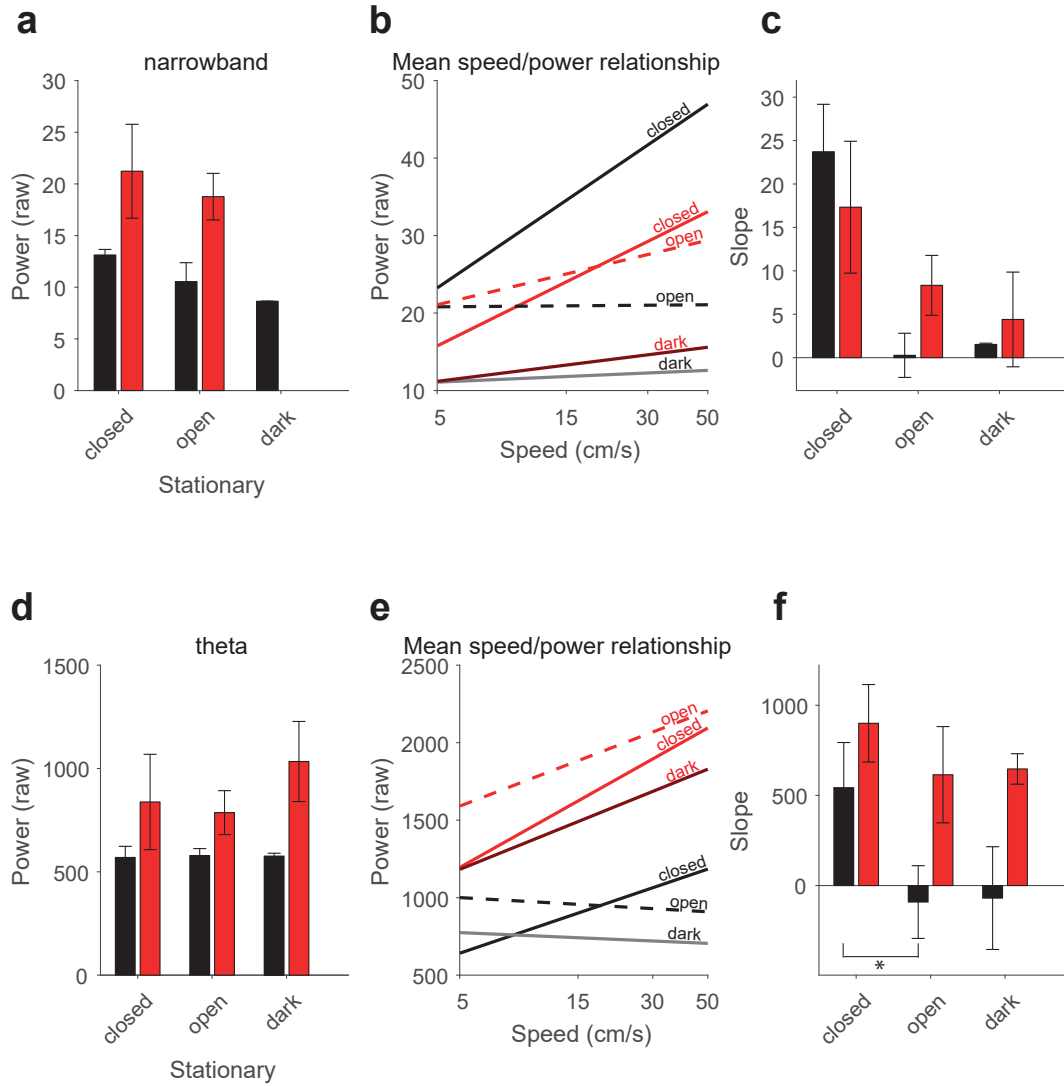


Figure 4.4: CA1 theta and V1 narrowband gamma relationships with mouse running speed in closed loop, open loop and dark conditions. (a) and (d) Stationary power in CA1 theta and V1 narrowband gamma in closed loop, open loop and dark running. **(b) and (e)** Mean speed-power relationships in closed, open and dark running for Tau+ (in red) and Tau- (in black). Speed-power relationships for each group are represented as the mean of all individual mice in that group. (Individual mice not shown). **(c) and (f)** Slopes of speed-power relationships in Tau+ and Tau- mice compared.

4.4c closed: $t(6) = -0.937$, $p = 0.3847$, Tau+: $M = 900$, $SD = 496$, $n = 4$, Tau-: $M = 543$, $SD = 578$, $n = 4$, open loop: $t(6) = -1.83$, $p = 0.1173$, Tau+: $M = 615$, $SD = 617$, $n = 4$, Tau-: $M = -91.6$, $SD = 466$, $n = 4$, dark: $t(6) = -2.09$, $p = 0.08178$, Tau+: $M = 647$, $SD = 195$, $n = 4$, Tau-: $M = -69.6$, $SD = 658$, $n = 4$).

4.3.3 Power changes over time

One potential confound for these power spectra analyses was that because our recording period spanned from 5-6.5 months, the recording sessions I was using for these analyses might be at slightly different ages in individual mice. As tau pathology, and associated changes in power spectrum, worsen in Tau+ mice over time (see Chapter 2), it might be the case that differences in mouse age could influence our results.

In order to check this, I compared V1 power spectra in individual mice at 6 months and 5.5 months against earlier recorded sessions at 5 months (Fig. 4.5a). Grouped analysis showed no difference between Tau+ and Tau- mice at 5.5 months (Fig 4.5b, t-tests at every frequency, maximum t : $t(7) = 1.79$, $p > 0.11$ for all frequencies, Tau+ $n = 4$, Tau- $n = 5$) and again no significant difference at 6 months (Fig. 4.5c, t-tests at every frequency, maximum t : $t(3) = 2.43$, $p > 0.09$ for all frequencies, Tau+ $n = 3$, Tau- $n = 2$) at lower frequencies.

This confirmed that the frequencies of interest for our analyses in V1 (narrow-band gamma and broadband gamma) were unaffected by mouse age between 5-6 months.

4.4 Results: Stimulus evoked potentials

In addition to looking at power spectra and changes in power with running speed in virtual reality, I also wanted to investigate LFP changes in response to visual stimuli in V1.

4.4.1 ERP to a full screen flash stimulus

As an initial analysis, I looked at visually evoked potentials in response to a full screen flash stimulus. Work by our collaborators (unpublished, from Lilly Pharmaceuticals) had shown that Tau+ mice showed differences in the amplitude of the C1 peak in the dentate gyrus during an auditory evoked potential protocol, with minor and less consistent differences in the C1 peak in CA1 (significant at 6.5 and 7.5 months, but not at 8 months), but responses to visual stimuli were not investigated (Blockeel et al, unpublished). I wanted to see whether a visual stimulus

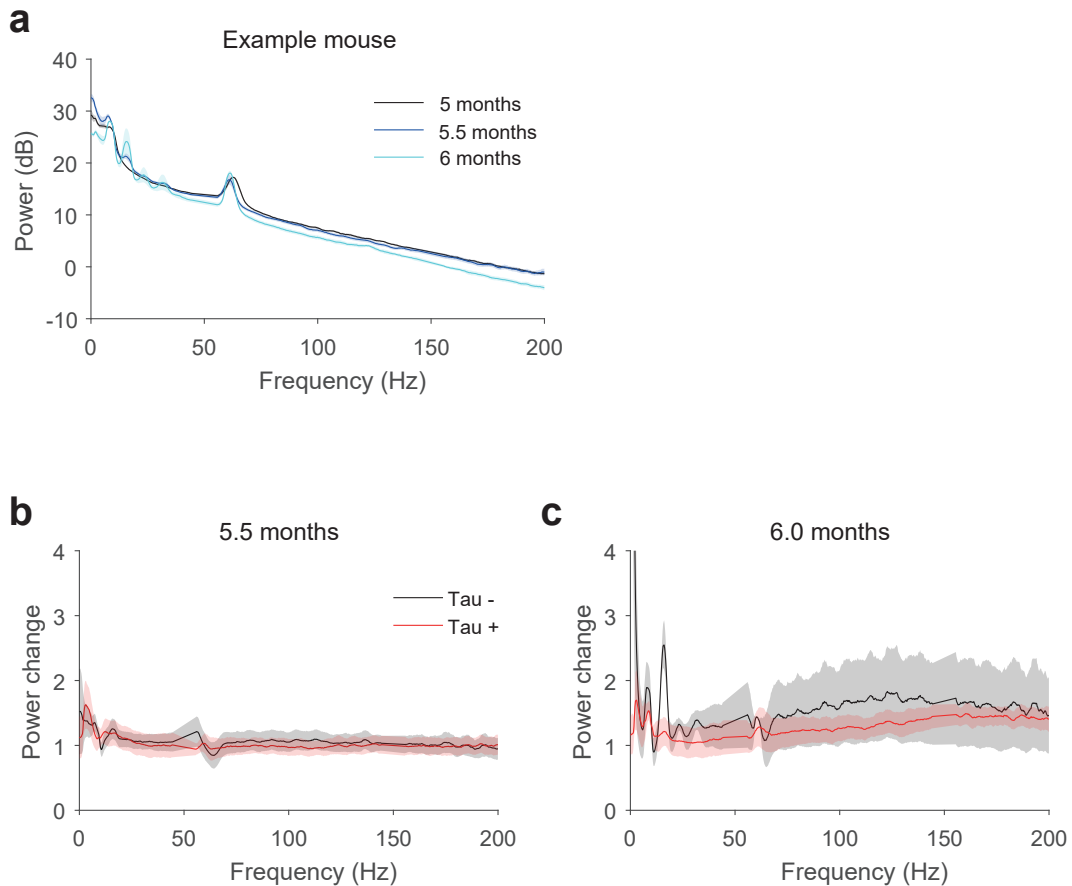


Figure 4.5: Tau+ and Tau- groups have similar changes in power due to age. (a) V1 power spectra from sparse noise sessions, grouped by age for an example mouse (b) Power spectra changes at 5.5 months in Tau+ and Tau- mice, normalised to power at 5 months. (c) Power spectra changes at 6 months in Tau+ and Tau- mice, normalised to power at 5 months.

would evoke a similar response in CA1, and also whether the ERP in V1 would show larger or earlier changes than in CA1, since V1 is a primary sensory area. In humans, the C1 peak during visually evoked potentials is generated from V1 (Clark and Hillyard, 1996; Clark et al., 1994). The amplitude of VEP components (P1 and N1, the C1 component was not compared) is also correlated with the degree of cognitive impairment in patients with both Alzheimer's disease and MCI (Stothart et al., 2015).

However, in our experiments, there was no difference in the ERP between Tau+ and Tau- mice either in V1 (Fig. 4.6a) or CA1 (Fig. 4.6b) and the ERP itself also looked very noisy. This may have been due to some noise issues I experienced

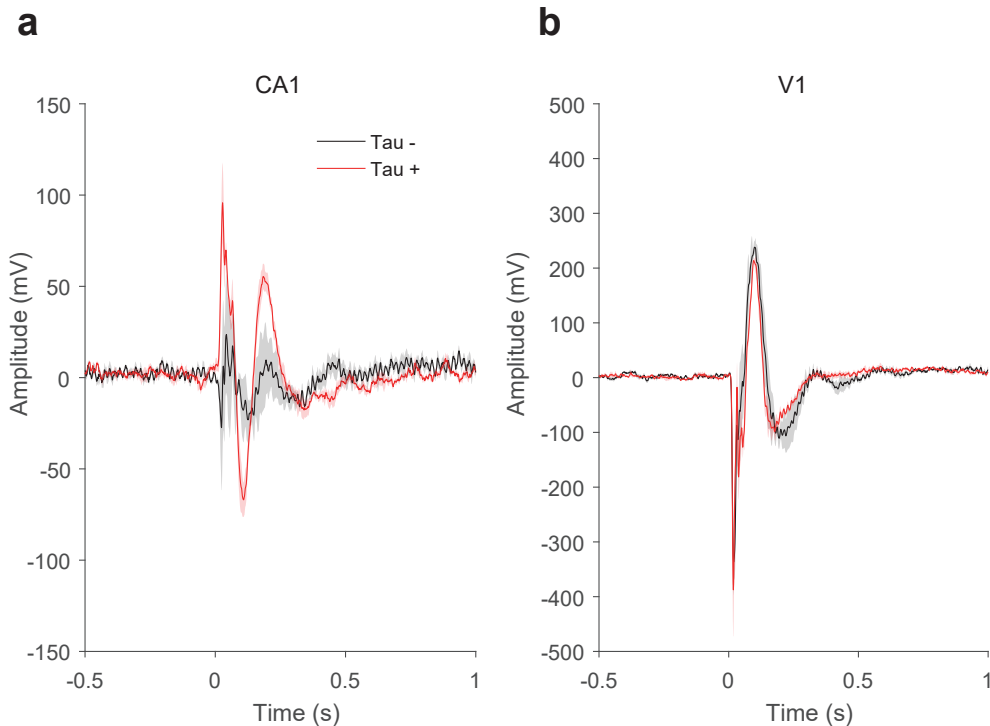


Figure 4.6: VEP amplitude is elevated in CA1 of Tau+ mice. (a) ERP in response to a 1s flash stimulus in V1 (L4). **(b)** ERP in CA1 in response to the same flash stimulus

specifically during the full screen flash protocol during recordings, which I was unable to fix. Given that auditory evoked potentials did not show any differences at this timepoint in previous work by Lilly colleagues (see Ch. 2), the fact that visually evoked potentials did not show a difference either is not surprising.

4.4.2 Stimulus-triggered power changes

More interesting than ERP changes, however, were changes in broadband and narrowband gamma power in response to visual stimuli. In the previous section, I showed that the Tau+ mice did not show any running speed dependent changes in V1 narrowband gamma, but this result could have been expected given that running speed is not the optimal driver of V1 narrowband gamma. A much better driver of V1 narrowband gamma is of course visual stimulation, for example the contrast or size of a stimulus (Saleem et al., 2017).

Normal wildtype mice show increasing broadband gamma power but decreasing narrowband gamma power to stimuli increasing in either contrast or size, and the

different responses reflect the different sources (cortical and subcortical) of broadband and narrowband gamma. Narrowband gamma should stay the same in Tau+ mice, as the areas it depends on (LGN) were not affected by tau pathology, but there might be differences in broadband gamma power, as broadband gamma is caused by cortical mechanisms. However, it was not clear what the direction of any broadband effect might be, given that there were no obvious changes in V1 broadband gamma power in our previous analyses (Fig. 4.2b).

4.4.2.1 Contrast

I investigated gamma power in V1 by first constructing normalised mean spectrograms for stimuli at different contrasts for each individual mouse. Figure 4.7b shows an example of a low contrast (6% contrast) stimulus and Figure 4.7a shows an example of a high contrast (100% contrast) stimulus. These responses could then be used to construct a contrast response relationship for broadband gamma, shown for Tau+ and Tau- groups in Figure 4.7c and narrowband gamma in Figure 4.7d. Linear fits for these relationships were obtained separately for each mouse which allowed me to compare the broadband and narrowband power relationships with contrast in Tau+ and Tau- mice. We chose to perform linear fits to reduce the number of parameters fitted to the response as the data was already noisy, and there was no obvious indication that another type of fit would be better. R^2 values for the broadband and narrowband linear fits for each individual mouse for both contrast and size can be found in Table 4.1.

Narrowband and broadband slopes were significantly different in Tau- mice ($t(8) = 02.8102, p = 0.0228$, narrowband $M = -0.0194, SD = 0.0302$, broadband $M = 0.0211, SD = 0.0112$, mice $n = 5$), similar to previous work in wildtypes (Saleem et al., 2017). However, there was no significant difference between narrowband and broadband slopes in Tau+ mice ($t(6) = -0.918, p = 0.3939$, narrowband $M = 0.0177, SD = 0.0333$, broadband $M = 0.0484, SD = 0.0579$, mice $n = 4$). There was also no difference between Tau+ and Tau- mice when broadband or narrowband slopes were compared between the groups (broadband: $t(7) = -1.05, p = 0.3285$, Tau+: $M = 0.0484, SD = 0.0579, n = 4$, Tau-: $M = 0.0211, SD = 0.0112$,

$n = 5$, narrowband: $t(7) = -1.76$ $p = 0.1226$, Tau+: $M = 0.0177$, $SD = 0.0333$, $n = 4$, Tau-: $M = -0.0194$, $SD = 0.0302$, $n = 5$).

Looking at the narrowband response to contrast in Figure 4.7d, it appears that Tau+ mice have a narrowband response to gamma that doesn't change much or is even slightly elevated with increasing contrast, compared to the Tau- mice who show a decrease in narrowband power. In broadband gamma, Figure 4.7c appears to show higher and more variable power in the Tau+ group, but Tau+ mice still show a positive relationship between broadband power and contrast, like Tau- mice, and wildtypes in previous work. This suggests, unexpectedly, that Tau+ mice have a difference in broadband gamma and narrowband gamma responses to contrast, but that this is due to changes in narrowband rather than broadband gamma.

4.4.2.2 Size

For size evoked changes, I again calculated normalised spectrograms for the different stimuli (small stimulus shown in Figure 4.8b, large stimulus shown in Figure 4.8a), and plotted broadband (Fig. 4.8c) and narrowband (Fig. 4.8d) power relationships to stimulus size.

This time, there was no significant difference between narrowband and broadband slopes in either Tau+ mice or Tau- mice (Tau+: $t(6) = -0.659$, $p = 0.5345$, narrowband: $M = 0.1005$, $SD = 0.0607$, broadband: $M = 0.1384$, $SD = 0.0977$, mice $n = 4$, Tau-: $t(6) = -1.86$, $p = 0.1121$, narrowband: $M = 0.0020$, $SD = 0.0263$, broadband: $M = 0.0937$, $SD = 0.0949$, mice $n = 4$). However comparing Tau+ and Tau- narrowband slopes showed a significant difference ($t(6) = -2.9757$, $p = 0.0248$, Tau+: $M = 0.1005$, $SD = 0.0607$, Tau-: $M = 0.0020$, $SD = 0.0263$), but Tau+ and Tau- broadband slopes were not different ($t(6) = -0.656$, $p = 0.5360$, Tau+: $M = 0.1384$, $SD = 0.0977$, $n = 4$, Tau-: $M = 0.0937$, $SD = 0.0949$, $n = 4$). Therefore the expected difference between broadband and narrowband slopes, which has been observed in wildtypes, was not present in Tau- mice.

The difference between Tau+ and Tau- mice in narrowband gamma is a little difficult to interpret in light of there not being any significant difference in Tau- mice between broadband and narrowband gamma. However, similar to the contrast

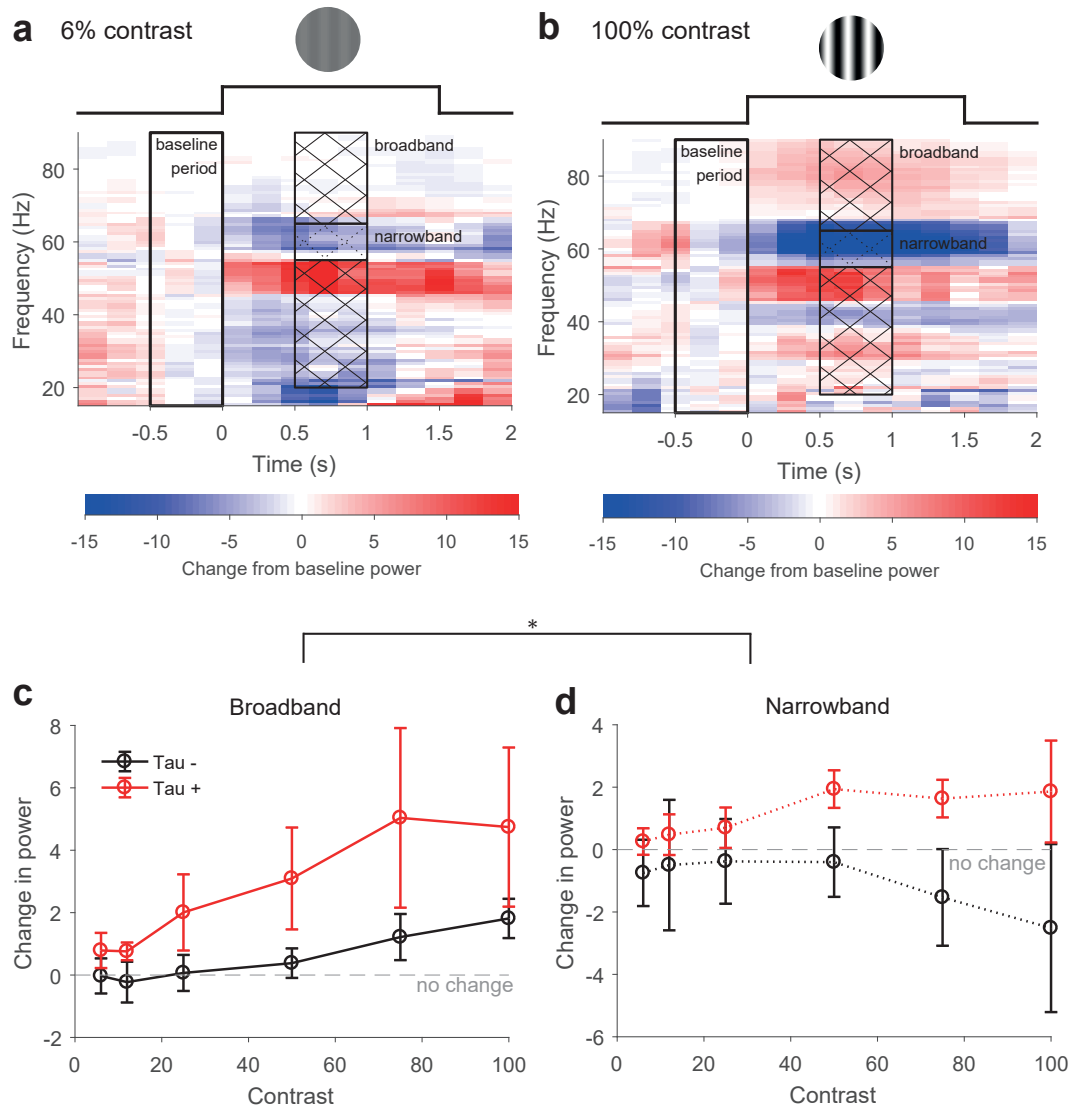


Figure 4.7: Tau+ mice do not show a decrease in narrowband gamma power with increasing contrast. (a) and (b) Example normalised spectrogram responses to high (100%) contrast (a) and low (6%) contrast (b). Normalised power change is calculated in relation to a pre-stimulus baseline period, indicated on the plot. Broadband and narrowband gamma responses were calculated from the labelled hatched regions. (c) Broadband gamma power changes at different contrasts in Tau+ and Tau- mice. (d) Narrowband gamma power changes at different contrasts in Tau+ and Tau- mice.

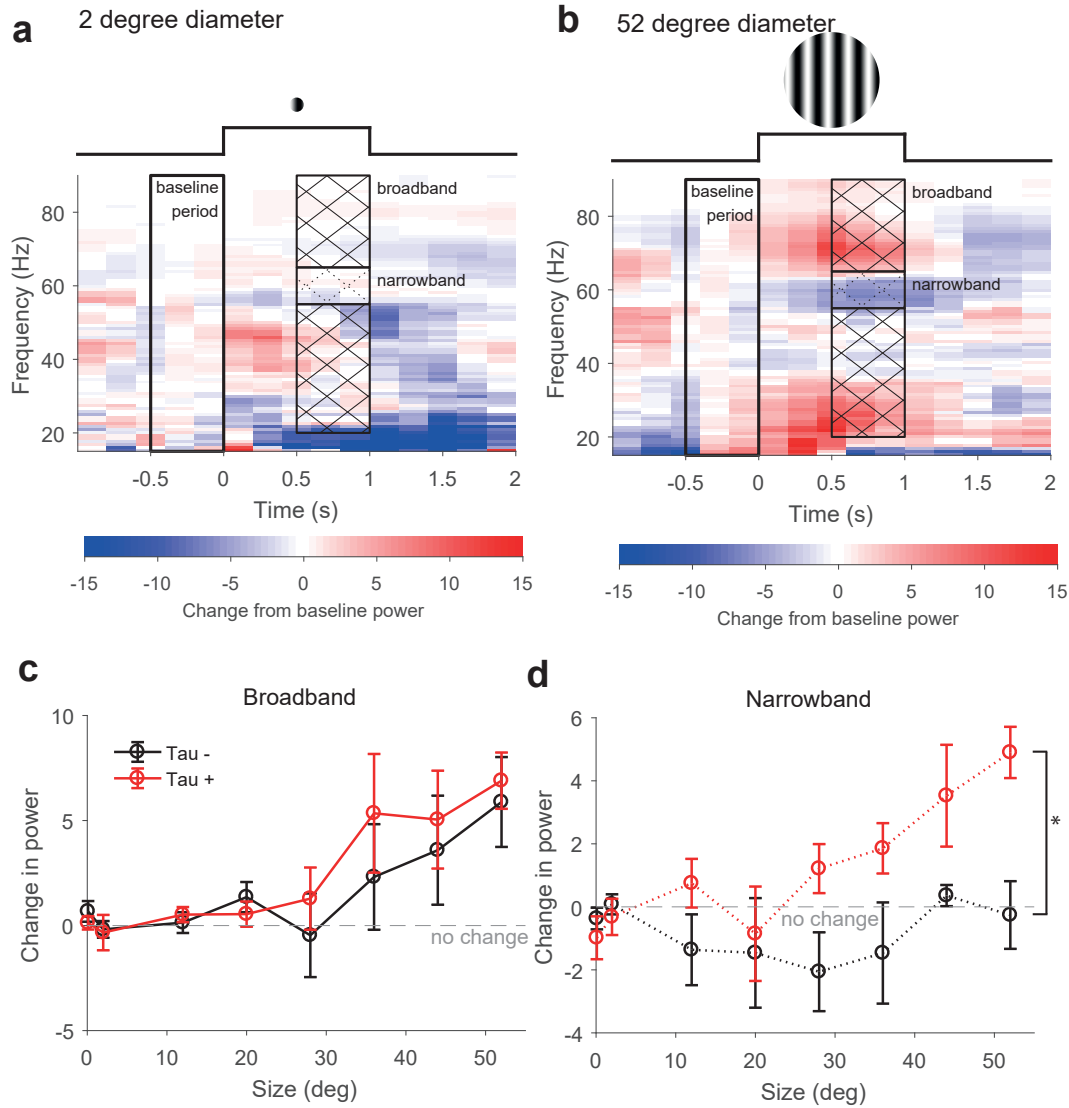


Figure 4.8: Size evoked narrowband gamma in V1. (a) and (b) Example normalised spectrogram responses to large (52 deg) (a) and small (2 deg) (b) drifting gratings (Example gratings not to scale). Normalised power change is calculated in relation to a pre-stimulus baseline period, indicated on the plot. Broadband and narrowband gamma responses were calculated from the labelled hatched regions. (c) Broadband gamma power changes with size in Tau+ and Tau- mice. (d) Narrowband gamma power changes with size in Tau+ and Tau- mice.

evoked gamma above, what appears to be happening in Figure 4.8d is that Tau+ mice have a more positive relationship of narrowband gamma with size, that looks more similar to a broadband gamma relationship.

Animal	Group	Broadband R^2 (Contrast)	Narrowband R^2 (Contrast)	Broadband R^2 (Size)	Narrowband R^2 (Size)
Mouse 1	Tau-	0.024	0.002	0.076	0.162
Mouse 2	Tau-	0.816	0.106	0.547	0.421
Mouse 3	Tau-	0.671	0.255	0.228	0.016
Mouse 4	Tau-	0.843	0.479	NaN	NaN
Mouse 5	Tau-	0.563	0.552	0.922	0.048
Mouse 6	Tau+	0.573	0.582	0.277	0.652
Mouse 7	Tau+	0.849	0.765	0.692	0.575
Mouse 8	Tau+	0.864	0.839	0.953	0.951
Mouse 9	Tau+	0.498	0.886	0.331	0.393

Table 4.1: R^2 values for linear fits.

4.5 Discussion

4.5.1 Power spectra changes in closed loop VR in Tau+ mice

I observed a small decrease in power at high frequencies in CA1 of Tau+ mice. There was a similar power reduction in V1 but this difference was not significant. The lack of significant difference in V1 was expected given previous Tg4510 results (see Chapter 2), but the differences in CA1 were surprising, as the earlier T-maze studies from my colleagues had shown differences mainly in the gamma range around 6 months, not in the high frequency ripple range.

There are a number of differences between this VR task and the T-maze task used in Chapter 2. Firstly, in VR the mouse is head fixed and running in a virtual environment rather than navigating a real world environment. Secondly, in the T maze the mouse had to make a decision about which way to turn, whereas in the VR corridor, the mouse is simply rewarded for continuing to run. The mouse was also rewarded at random locations in the VR corridor with Ribena, compared to the T-maze where sugar pellet rewards occurred at the end of a choice arm. Therefore, the T maze was probably more engaging.

The mice I used for these experiments also did not appear to find Ribena very rewarding - some of them drank it but some ignored it or seemed to find the Ribena drops mildly aversive. Therefore, the mice in my experiments may have had a more variable behavioural state than in the T-maze, where they were motivated and expecting a reward. In most head-fixed virtual reality experiments, the mice are water deprived and rewarded with drops of water, which is highly motivating, but as my Dox control mice I used for my experiments were administered doxycycline

in their drinking water, it was not possible to water deprive them.

Another source of difference, aside from task demands, are that running speed and also gait may be different between the two experiments. The power spectra for VR running were taken when mice were running at a medium speed, whereas in the T-maze running speed is generally higher (e.g. Fig. 3.2e in the same Tg4510 mice at a younger age). Anecdotally, mice running on a VR wheel do not have the same running motion as in the real world and many of my mice seemed to struggle with it, often climbing the wheel instead of running.

The changes in high frequency power probably reflect the reduced firing rate explored in Chapter 5 rather than differences in ripple frequency/amplitude, as both V1 and CA1 high frequency power are reduced. However, changes in ripples may be an interesting area for follow up work. Witton et al. (2014) found that ripple amplitude in 7-8 month old Tg4510 mice is reduced during sleep - it would be interesting to see whether this is also the case at an earlier stage of tauopathy and also during task learning, given the role of ripples in memory (e.g. Jadhav et al., 2012).

4.5.2 Speed/power relationships in closed loop, open loop and in the dark

It is difficult to draw strong conclusions about the speed/power relationship in Tau+ mice given that the only significant difference was the expected decrease in the slope of the CA1 theta speed/power relationship in Tau- mice in open loop compared to closed loop running. One potential explanation for not seeing differences that we expected is that the speed/power slope calculations might differ across mice. For example, there was no difference between closed loop and dark running in the Tau- mice, where I expected to see an effect. This may be because occupancy of the different speed bins, which were used to calculate the speed-power relationships, was not consistent across mice. Therefore some mice might have a speed/power line calculated from two points (e.g. stationary and medium speed) whereas others might have a speed/power line calculated from all four possible points (stationary, low, medium, high).

A slightly different method of calculating the speed/power relationship, for example more speed bins, could help somewhat to make these results more robust but are unlikely to make a large difference. For a mouse that always runs at medium speeds or sits still, for example, the speed-power relationship would still only be calculated from stationary and medium points and would not have any low or high speed measurements. However, questions of running speed are probably best addressed by running further experiments, for example looking at changes in power vs running speed in real world environments and running wheels, not just in head-fixed virtual reality environments.

There is an interesting (non-significant) trend of Tau+ mice having more similar speed/power relationships in closed loop, open loop and dark running compared to Tau- mice, which show a flattening of the relationship in open loop and dark running. Further work would be required to confirm whether this is an actual effect, as our results were not significant. If this were true, it would agree in an interesting way with Cheng and Ji (2013)'s finding that CA1 neurons in Tg4510 mice have less spatial information content and are more driven by internal input. Similarly, the differences between closed loop, open loop and dark running are purely in the external environment - whether there is a visual stimulus and whether it matches the mouse's own motion - whereas the internal self-motion cues are similar across all conditions.

Another exciting area of follow up work is to investigate CA1 and V1 unit firing during closed loop, open loop and dark running. Since Tg4510 mice show reduced spatial information in CA1 in the real world (Cheng and Ji, 2013), it would be interesting to see if this is also the case in virtual reality, and to compare how information content changes in CA1 when visual input is absent (dark) or not linked to self motion (open loop).

4.5.3 Power spectra at different ages

I looked at power changes at different ages (5.5 and 6 months) in my mice to see if changes in power over this timespan might be affecting my results, and I did not observe any differences in power at the time range I observed. However there were

a few difficulties in performing this analysis. As the V1 drive was moved during the course of recording, it was not possible to get recordings at the same depth spanning from 5 to 6.5 months. In addition recording start and finish ages varied slightly between mice depending on when surgery could be performed. I picked cortical depths to try to maximise the available timespan, but due to these problems I was only able to perform this time based analysis at 5.5 and 6 months, because I did not have enough mice for the 6.5 month comparison. As this was when the mice were culled, they were usually retired from recording a week or so before culling. I also decided not to run this power change analysis in CA1, as it usually took a couple of weeks of drive movement to find the cell layer (longer in some mice) leaving a much shorter timespan for analysis.

Because the depth was picked to maximise time span, the channel for this analysis was not necessarily in layer 4, where other V1 power spectra analyses were performed. Therefore if there were greater changes over time in layer 4 compared to other layers, my analysis would not have picked this up.

In previous analyses of power in cortical areas (PFC) in Tg4510 mice over time (Chapter 2), power differences do not begin to appear between Tau+ and Tau- mice until 8 months, and even then are relatively minor. Therefore, I do not think power changes would have been very large in V1 at the timepoint I was recording. Furthermore this problem is always present with any timepoint choice, and I chose to prioritise obtaining more recordings over having a very exact time span.

4.5.4 Changes in stimulus-evoked V1 narrowband gamma

Tau+ narrowband and broadband slopes were similar in contrast-evoked gamma, while Tau- slopes were significantly different, as expected. For size evoked gamma, neither narrowband versus broadband comparison (in either Tau+ or Tau- mice) was significant, but the Tau+ and Tau- groups were significantly different from each other.

In general, narrowband gamma changes were not as negative or as large as expected (based on previous work by Saleem et al., 2017), even in Tau- mice. This may be because of differences in the numbers of mice used in Saleem et al. (2017)

compared to my experiments - they had 7 mice whereas I had 4 mice in each group. Another possible explanation is that my mice might have had differences in running speed compared to the mice in Saleem et al. (2017) - V1 narrowband gamma also increases with running speed. If my Tg4510 mice ran faster than normal WT mice, this might explain their altered narrowband gamma results.

What appears to be happening with the Tau+ mice and evoked V1 gamma is actually a similar effect to what is seen with running speed and CA1 theta. Instead of the difference in response seen in wildtypes (Saleem et al., 2017), responses (here, narrowband and broadband slope) are more similar to each other in Tau+ mice. Narrowband gamma, instead of decreasing in response to contrast and size, appears to be increasing.

This is surprising, as V1 narrowband gamma is driven by LGN input, and LGN is not affected by tauopathy in these mice. However, as tau expression in this model is driven by CamKII, which is expressed in pyramidal cells (Ramsden et al., 2005; Wang et al., 2013), what may be happening is that the inhibitory cell activity driving broadband gamma (e.g. Cardin et al., 2009) may be less affected than thalamocortical synapses onto pyramidal cells which drive narrowband gamma (Saleem et al., 2017). If the narrowband gamma input was lessened or abolished, then the broadband gamma response would predominate in the narrowband range and broadband and narrowband responses would appear to be similar. Nevertheless, since our results were inconclusive, this would still have to be confirmed by further research.

4.6 Summary and conclusions

In summary, I found a significant decrease in high-frequency power in CA1 in Tau+ mice in the basic power spectrum (running at medium speed in closed loop). Aside from this there were no other clear cut group differences.

It is a little disappointing that I did not get more conclusive results from the various power spectra analyses I conducted, but this was expected to some extent from the previous T-maze LFP analyses showing limited changes in Tau+ mice

around this timepoint. Some interesting trends have still emerged, particularly in evoked V1 narrowband gamma responses, and in CA1 theta relationships with running speed. Tau+ mice appeared to have less sensitivity to visual input in the CA1 theta speed/power relationship, and less of a distinction between broadband and narrowband responses. However these experiments have not been able to confirm whether these represent true differences or just random fluctuations in individual mice that are unrelated to tau pathology. This would have to be confirmed by further work.

Chapter 5

Effect of tauopathy on receptive field properties of V1

5.1 Introduction

In this chapter, I focus on unit firing in V1 of Tg4510 mice. In particular, I look at single unit responses to changes in a specific stimulus dimension such as contrast or size. The pattern of response across a stimulus dimension is known as feature tuning. For example, tuning for orientation and direction in visual cortex was first observed by Hubel and Wiesel in the 1960s (Hubel and Wiesel, 1962, 1968). Feature tuning for different stimulus dimensions can be described by models relating the stimulus to the single unit response. I use these models in my chapter to understand how feature tuning changes in the Tg4510 mouse.

5.1.1 Feature tuning and underlying mechanisms in primary visual cortex

Feature tuning in primary visual cortex has been shown to have similar characteristics across many species, including more recently the mouse (Niell and Stryker, 2008). Researchers looking at the early visual system have, from the beginning, modelled the responses of single neurons to visual features by defining and fitting tuning curve equations that describe the relationship of the stimulus to the neuron's response (Naka and Rushton, 1966). This has been done for a wide range of stimulus features, such as orientation, size and spatial frequency (Kohn and Movshon,

2004; Cavanaugh et al., 2002; Croner and Kaplan, 1995; Enroth-Cugell and Robson, 1966), and the ensuing large body of modelling work makes it possible to measure changes in V1 function in terms of model parameters (e.g. Ayaz et al., 2013, for changes to size tuning during locomotion). This allows us to define functional changes quantitatively defined with reference to tuning models, and effects such as changes in gain or changes in baseline firing can be dissociated. Because of this, primary visual cortex is an ideal area for creating a comprehensive profile of functional changes in a neural population affected by tauopathy.

Functional changes in V1 can also, to some degree, be mapped to changes in underlying circuit mechanisms. While there is not yet a unified, comprehensive understanding of all feature tuning in V1 (although work has been done in this area e.g. Carandini and Heeger, 2011), there is an increasing body of work on how feature tuning arises, for example how different cell classes contribute to feature tuning (Hofer et al., 2011; Adesnik, 2017) as well as how input from other areas can affect tuning curves (Ayaz et al., 2013; Niell and Stryker, 2010). Thus, understanding of how single neuron computations arise from local and more long-range connectivity is extremely advanced in primary visual cortex compared to other cortical or hippocampal areas. Another important goal of research in primary visual cortex is to use findings in V1 to understand the general structure and function of the cortical microcircuit (Harris and Shepherd, 2015). Similarly with my own experiments, I hope to not only characterise how visual information processing is altered in a network affected by tauopathy, but also provide insight into the broader question of how cortical information processing in general is altered when tauopathy takes hold.

The experiments I have conducted consider the more standardised forms of feature tuning, where a single feature dimension is varied. More complex forms of feature tuning, where tuning for one feature can modulate the tuning for another (e.g. contrast normalisation) are not addressed in these experiments.

5.1.2 What is known about information processing by single units in the Tg4510 mouse

In one of the few papers looking at information processing in the Tg4510 mouse, Cheng and Ji (2013) observed that neurons in CA1 of 7-9 month old Tg4510 mice have lower spatial information content and more stereotyped firing patterns, suggesting that tauopathy might confer a general insensitivity to external information and bias for internally generated input, at least in CA1. In contrast, a study in V1 of Tg4510 mice by Kuchibhotla et al. (2014) found that orientation tuning was normal even in NFT-bearing neurons of 8-10 month old Tg4510 mice, suggesting information processing functions can be preserved even at a late stage of tauopathy. These conflicting results in different brain areas of both information processing and its disruption lead to the question of how such differences can arise - whether they result from differences in brain area alone or whether different types of information processing are selectively altered by tauopathy.

At the timepoint used by these two studies, gross atrophy and neuronal death had already occurred in both cortex and hippocampus (Spires et al., 2006). By looking at mice at an earlier timepoint (5 to 6.5 months), where synaptic alterations are prominent but large scale neuronal death has not yet taken place (Jackson et al., 2017), the effects of tauopathy can be characterised at an earlier stage, which may be more useful for early diagnosis and for drug development.

Aside from research looking at information processing by single units in awake behaving mice, Menkes-Caspi et al. (2015) observed reductions in firing rate in the frontal cortex of 4.5-6 month old Tg4510 mice under anaesthesia, as well as longer down states and fewer successful transitions to up states. Jackson et al. (2017) also found reduced firing rate in barrel cortex as well as fewer neurons that were responsive to whisker stimulation in 5-6 month old Tg4510 mice, concomitant with changes in synaptic turnover and density. Hence, at this earlier stage of tauopathy, where synaptic changes are already taking place, changes in neuronal firing can be observed. In this chapter I will try to elucidate what the functional consequences of these synaptic changes will be.

5.2 Methods

Details of mouse group assignments, recordings and visual protocols run can be found in Chapter 3. This methods section covers details of analysis methods.

I was blinded to group identity during spike sorting and all analyses apart from the centre/surround firing rates analysis (Fig. 5.3) for sparse noise.

All analysis was carried out using Matlab (MathWorks, Natick, MA, USA).

5.2.1 Spike sorting

Every day during data acquisition, all recorded sessions from a single mouse were merged so that each mouse had a single daily data file. Spikes were automatically detected from this file and clustered using KiloSort. I then manually accepted, rejected and merged clusters using phy based on the methods outlined in the phy user guide (<https://phy-contrib.readthedocs.io/en/latest/template-gui/#a-typical-approach-to-manual-clustering>). Only manually accepted clusters were progressed for further analysis.

5.2.2 Mean firing rates

Mean firing rates for the stimulus ON condition were calculated from the entire duration of stimulus presentation, and mean firing rates during the stimulus OFF condition were calculated from 0.5s prior to stimulus onset. For the firing rates analysis shown in Figure 5.1, only a subset of protocols were used. The protocols excluded were sparse noise (because it was not a drifting grating), adaptation protocols (because of adaptation effects and also because the pre-stimulus period was not a gray screen during adaptation), size vs temporal frequency (because two feature dimensions were varying at once) and centre surround protocol (because number of stimulus repeats was different from other protocols).

Mean firing rates for stimulus ON condition in Figure 5.1 were calculated using all stimulus presentations without any separation based on varying features of the stimulus (e.g. high vs low contrast). When calculating observed mean firing rates for modelling the tuning curves, a separate mean firing rate was calculated for each type of stimulus presented in the protocol (e.g. 6%, 12%, 25%, 50%, 75% 100% in

the case of contrast).

5.2.3 Modelling tuning curves

5.2.3.1 Model fitting

Tuning curves were modelled separately for each neuron recorded during a visual protocol by using a pre-determined equation for each type of stimulus tuning (e.g. Figure 5.4a shows a dual von Mises curve for orientation). The model was fit to the observed mean firing rates by minimising log likelihood, which was calculated as:

$$l(\theta|x) = \sum_{i=1}^n \log f(x_i|\theta) \quad (5.1)$$

where θ represents the parameters of the model fit, n represents the total number of observations used to fit the model - in my analyses, this equals the number of types of stimulus presented as model fits were calculated from mean firing rate - and x_i represents observed mean firing rates at different points on the tuning curve e.g. i would represent different orientations for the orientation protocol.

The likelihood of each observed response given the predicted response from the model was:

$$l(x|\lambda) = \frac{e^{-\lambda} \lambda^x}{x!} \quad (5.2)$$

i.e. the firing of each neuron (x) was treated as a Poisson process with the predicted firing rate as the mean (λ).

Log likelihood was minimised using the `fmincon` function in Matlab, and parameters were individually subject to upper and lower bounds. All predicted tuning curves were also constrained to have a minimum firing rate of 0 Hz so that negative firing rates were not possible. I manually set initial parameters to try to maximise the number of well fit neurons across all recorded sessions.

5.2.3.2 Normalised log likelihood and analysis thresholds

After all neurons were fit using tuning curves, the normalised log likelihood was calculated for each neuron as

$$\frac{LL - LB}{UB - LB} \quad (5.3)$$

where LL is the log likelihood calculated using Equation 5.1, LB is the lower bound for log likelihood, calculated using the mean of all observed firing rates for that neuron as λ in Equation 5.1, and UB is the upper bound for log likelihood, using the same observed firing rates at each point in the tuning curve for both λ and x .

The fit quality distribution was then calculated for the entire population using the normalised log likelihood (NLL) measure. Following this, cells were only used for further analyses looking at other measures if they passed an analysis threshold, which was a normalised log likelihood cutoff. For most protocols this was $NLL > 0.5$ but for sparse noise the threshold was lower at $NLL > 0.25$ as there were many more points for observed responses.

5.2.3.3 Receptive field model

The sparse noise mean response was calculated differently from the other protocols, as the sparse noise stimulus consisted of a movie of small white and black squares turning on and off at different times instead of drifting gratings. I used responses only to the white squares for my analysis.

Mean response was calculated by taking spike counts from 200ms following each white square onset and using these to calculate the mean response at each point in the visual field map.

To fit responses to the sparse noise stimulus, I used a tilted 2D gaussian:

$$R_{pred} = A \exp - \left(\frac{((x_i - x_0) \cos \theta)^2}{2\sigma_x^2} + \frac{((y_i - y_0) \sin \theta)^2}{2\sigma_y^2} \right) + b \quad (5.4)$$

where R_{pred} is the predicted response, A is the magnitude of the response, x_0 and y_0 define the centre point of the tilted gaussian, σ_x and σ_y define the length of the axes of the tilted gaussian, θ is the tilt angle and b is the baseline.

From the model I calculated receptive field area size, which was the size of the ellipse defined by σ_x and σ_y , and ellipse axis ratio, which was the ratio between σ_x

and σ_y , where the longer (major) axis was the numerator.

For the centre surround analysis, I used the centre point defined by x_0 and y_0 and found the nearest square presentation location to that point. I then defined that square and all immediately adjacent squares (9 squares total, where each square side length is 8 degrees) as the centre region, excluded all immediately adjacent squares to the centre region from analysis, and defined all other squares as the background region. An illustration can be found in Figure 5.3a.

5.2.3.4 Direction tuning model

For direction tuning, I fit a dual von Mises to model the response:

$$R_{pred} = \frac{A_1 \exp(\kappa \cos(\theta_i - \theta_{pref}))}{2\pi I_0(\kappa)} + \frac{A_2 \exp(\kappa \cos(\theta_i - \theta_{pref} + \pi))}{2\pi I_0(\kappa)} + b \quad (5.5)$$

where A_1 and A_2 are the magnitude of response at the cell's preferred direction and at the opposite direction, κ is the tuning width, θ_{pref} is the preferred direction and $I_0(\kappa)$ is the modified Bessel function of order 0.

From the resultant model fits I calculated OSI and DSI, where OSI was:

$$\frac{R_{pref} - R_{orth}}{R_{pref}} \quad (5.6)$$

and DSI was:

$$\frac{R_{pref} - R_{opp}}{R_{pref}} \quad (5.7)$$

Tuning width was calculated as half width half height from peak and baseline (b) and preferred orientation (θ_{pref}) were taken from model parameters.

The f1 response was calculated by taking the Fourier transform of the f0 response and using the value at the frequency nearest to the temporal frequency of the stimulus (2 Hz).

OSI for f1 response was calculated from the observed response as:

$$\frac{R_{pref} - R_{orth}}{R_{pref} + R_{orth}} \quad (5.8)$$

$$\frac{R_{pref} - R_{orth}}{R_{pref} + R_{orth}} \quad (5.9)$$

and DSI as:

$$\frac{R_{pref} - R_{opp}}{R_{pref} + R_{opp}} \quad (5.10)$$

5.2.3.5 Orientation adaptation

The same model used for orientation (Eq. 5.5) was used to separately fit tuning curves in pre-adaptation, adaptation and post-adaptation.

Suppression index for pre-adaptation and adaptation was calculated by:

$$\frac{R_{pre} - R_{adapt}}{R_{pre}} \quad (5.11)$$

and for pre-adaptation and post-adaptation as:

$$\frac{R_{pre} - R_{post}}{R_{pre}} \quad (5.12)$$

where R is the response at the selected orientation (preferred or adaptor). For pre-adaptation and adaptation suppression, only cells which passed the fit quality threshold ($NLL > 0.5$) in both blocks were used for the analysis, and similarly for pre-adaptation and post-adaptation suppression.

5.2.3.6 Contrast tuning model

Contrast tuning was fit with the Naka-Rushton equation:

$$R_{pred} = \frac{R_{max}C^n}{C^n + C_{50}^n} + b \quad (5.13)$$

where R_{max} is the maximum response, C_{50} is the semisaturation constant and n describes the slope of the line.

Signed sigma is the absolute value of C_{50} , and signed sensitivity is $\frac{nR_{max}}{4C_{50}}$

5.2.3.7 Size tuning model

The size tuning model is:

$$R_{pred} = \frac{(R_{centre} \operatorname{erf}(\frac{d}{d_{centre}})^2)^2}{1 + R_{surround} \operatorname{erf}(\frac{d}{d_{surround}})^2)^2} + b \quad (5.14)$$

where, roughly, R_{centre} and $R_{surround}$ define the magnitude of the centre and surround responses, and d_{centre} and $d_{surround}$ define the size of the centre and surround responses.

Preferred size was the smallest size where the response was 95% of the maximum response, and suppression index was calculated as:

$$SI = \frac{R_{pref} - R_{maxsize}}{R_{maxsize}} \quad (5.15)$$

where R_{pref} was the response at the preferred size (as defined above) and $R_{maxsize}$ was the response to the largest stimulus (52 degrees diameter).

5.2.3.8 Spatial frequency tuning model

The spatial frequency tuning model was:

$$R_{pred} = R_{centre} \pi d_{centre}^2 \exp(-(\pi d_{centre} s)^2) - R_{surround} \pi d_{surround}^2 \exp(-(\pi d_{surround} s)^2) + b \quad (5.16)$$

where, roughly, R_{centre} and $R_{surround}$ define the magnitude of the centre and surround responses (centre and surround with respect to preferred spatial frequency), and d_{centre} and $d_{surround}$ define the size of the centre and surround responses.

Preferred spatial frequency was calculated as the spatial frequency at the maximum response, full width half height was calculated around the maximum response, and the low spatial frequency rolloff was:

$$\frac{R_{max} - R_{minSF}}{R_{max}} \quad (5.17)$$

where R_{max} was the maximum response and R_{minSF} was the response at the lowest

spatial frequency (0.01cpd).

5.3 Results

5.3.1 Mean firing rates

I began by looking at how firing rates differed between Tau+ and Tau- across a selected range of drifting grating protocols, shown in Figure 5.1a. I chose protocols where stimuli only varied across one dimension and where the interstimulus gray screen was roughly the same length of time, hence excluding the orientation adaptation protocol. In these protocols, I compared firing rates in Tau+ and Tau- cells when the stimulus was either off or on (Fig. 5.1c). Tau+ mice had a significant reduction in firing rates both when the drifting grating stimulus was on ($t(6557) = -3.5727, p < 0.001$, Tau+: $n = 3329, M = 6.1734, SD = 7.1109$, Tau-: $n = 3241, M = 6.8293, SD = 7.7510$) and when the drifting grating stimulus was off and only a gray screen was displayed ($t(6557) = -3.0323, p = 0.0024$, Tau+: $n = 3329, M = 8.3834, SD = 10.0226$, Tau-: $n = 3241, M = 9.1676, SD = 10.9124$). An interesting aspect of this result was that the reduction in firing rate in Tau+ mice compared to Tau- mice did not appear to be uniform across all different protocols. Figure 5.1d shows firing rates in Tau- versus Tau+ groups by protocol, and some protocols, for example size and annulus size, appear to show a greater change in firing rate whereas firing rate is more similar between Tau+ and Tau- mice in contrast, orientation and spatial frequency protocols, for example. The protocol-specific difference was present even during the interstimulus interval ('stimulus off') when only a gray screen was present.

The non-uniform firing rate reductions in different visual protocols suggested that Tau+ neurons in V1 did not have just a simple reduction in firing rate, but rather Tau+ neurons might respond differently to different types of visual stimuli, with altered responses to some stimulus features but normal responses to others. To understand how the Tau+ V1 population responded to different visual features, I investigated a few visual protocols in more detail.

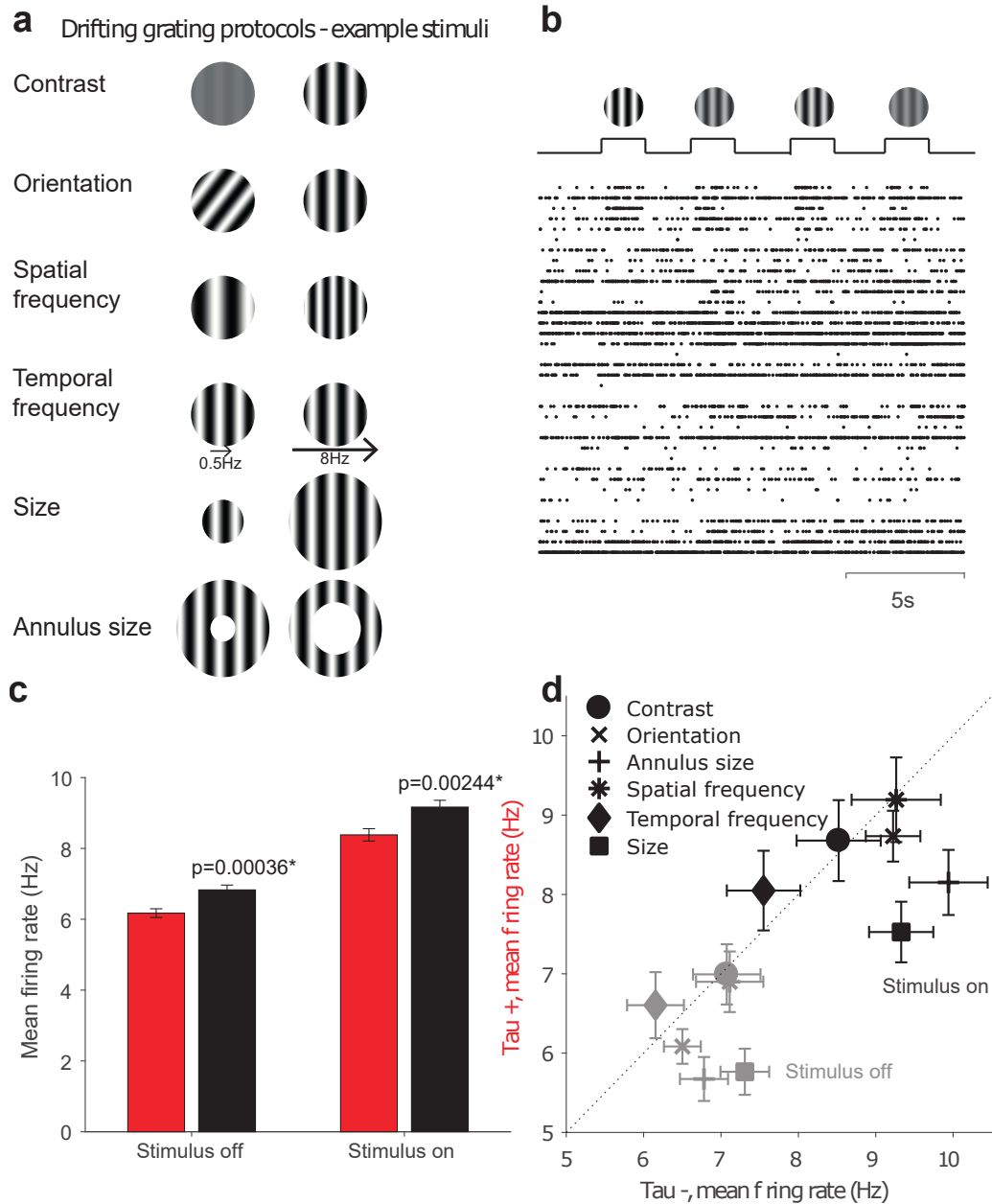


Figure 5.1: Tau+ mice have reduced firing rates before and during stimulus presentation. (a) Example stimuli from selected drifting grating protocols. (b) Example rasters from a contrast protocol recording session. Each line is a different cell. Presented stimuli and line indicating stimulus on/off times are shown above the rasters. (c) Pre-stimulus and evoked firing rate in Tau+ and Tau- mice, across all drifting grating protocols shown in (a). Error bars are SEM. (d) Pre-stimulus and evoked firing rate for Tau- vs Tau+ mice, split by protocol. Dotted line indicates where firing rate would be equal between the groups. Firing rate differences vary by protocol.

5.3.2 Spatial receptive fields

In order to investigate spatial receptive field properties, I analysed responses to a sparse noise stimulus. The sparse noise stimulus, an example frame of which can be seen in Figure 5.2a, consisted of small black and white squares (side length 8 degrees) displaying at random times on a gray screen background. More stimulus details can be seen in Chapter 3.

I fitted a tilted 2D gaussian (Fig. 5.2b) to each cell response (Fig. 5.2c). Neurons in Tau+ mice had lower fit quality than Tau- mice (Fig. 5.2d, $Z = 8.0233$, $p < 0.00001$, Tau+: $n = 2149$, median = 0.2037, Tau-: $n = 2186$, median = 0.2766). The size of the receptive field was slightly larger in Tau+ mice (Fig. 5.2e, $Z = -2.1974$, $p = 0.0280$ Tau+: $n = 939$, median = 120.9948, Tau-: $n = 1180$, median = 104.7284), but there was no difference in the shape of the receptive fields between the groups, as measured by the ratio of the major and minor axes of the ellipse making up the receptive field (Fig. 5.2f, $Z = 1.2253$, $p = 0.2205$, Tau+: $n = 939$, median = 2.3568, Tau-: $n = 1180$, median = 2.4566).

To further understand the decrease in fit quality for Tau+ mice which I observed, I looked at firing rates when squares were on within the receptive field centre versus firing rates when squares were on in the background area. I used the centre location of the receptive field from the model fit for each cell to define centre and background regions (Fig. 5.3a). Z-scored firing rates were significantly lower in Tau+ mice in all conditions - when squares were on in the centre regions, when squares were on in the background regions, and when they were on in both centre and background regions. (Fig. 5.3b, centre: $t(4333) = 5.7381$, $p < 0.0001$, Tau+: $n = 2149$, $M = 0.6571$, $SD = 0.8113$, Tau-: $n = 2186$, $M = 0.8050$, $SD = 0.8837$. background: $t(4333) = -6.6864$, $p < 0.0001$, Tau+: $M = -0.0739$, $SD = 0.0941$, Tau-: $M = -0.0941$, $SD = 0.1045$. centre + background: $t(4316) = 4.1707$, $p < 0.0001$, Tau+: $n = 2142$, $M = 0.7355$, $SD = 1.3141$, Tau-: $n = 2176$, $M = 0.9119$, $SD = 1.4606$).). However there was no difference in firing rate variability, measured by Fano factor, in any of the conditions (Fig. 5.3c, centre: $t(4312) = -0.403$, $p = 0.6871$, Tau+: $M = 29.3$, $SD = 11.9$, $n = 1180$,

Tau-: $M = 28.7$, $SD = 11.3$, $n = 989$, background: $t(4410) = -1.66$, $p = 0.09733$, Tau+: $M = 12.8$, $SD = 5.76$, $n = 1205$, Tau-: $M = 12$, $SD = 5.09$, $n = 1005$, centre + background: $t(3828) = -1.34$, $p = 0.1799$, Tau+: $M = 29.3$, $SD = 16.1$, $n = 1050$, Tau-: $M = 29.7$, $SD = 14.8$, $n = 911$).

For cells with good fit ($NLL > 0.25$), where the receptive field was clearly identifiable, Tau+ and Tau- mice had significantly different firing when either centre or background stimuli were on, but not when centre and background stimuli were both on at the same time (centre: $t(2117) = 2.0163$, $p = 0.0439$, Tau+: $n = 939$, $M = 1.2015$, $SD = 0.8900$, Tau-: $n = 1180$, $M = 1.2803$, $SD = 0.8960$. background: $t(2117) = -2.5085$, $p = 0.0122$, Tau+: $M = -0.1399$, $SD = 0.1032$, Tau-: $M = -0.1514$, $SD = 0.1068$; centre + background: $t(2117) = 1.122$, $p = 0.2619$, Tau+: $M = 1.35$, $SD = 1.39$, $n = 939$, Tau-: $M = 1.42$, $SD = 1.51$, $n = 1180$). Variability was not significantly different in any conditions for cells with good fit (centre: $t(2117) = 0.0901$, $p = 0.928$, Tau+: $M = 29.8$, $SD = 10.1$, $n = 939$, Tau-: $M = 29.8$, $SD = 10.7$, $n = 1180$, background: $t(2117) = -1.75$, $p = 0.0808$, Tau+: $M = 13.7$, $SD = 5.25$, $n = 939$, Tau-: $M = 13.3$, $SD = 5.84$, $n = 1180$, centre + background $t(2080) = -0.913$, $p = 0.361$, Tau+: $M = 30.3$, $SD = 14.1$, $n = 926$, Tau-: $M = 29.7$, $SD = 14.3$, $n = 1156$).

For cells with bad fit ($NLL < 0.25$), there was only a significant difference in firing rate when background stimuli were on (background: $t(2214) = -2.3777$, $p = 0.0175$, Tau+: $n = 1203$, $M = 0.2547$, $SD = 1.0220$, Tau-: $n = 996$, $M = 0.3064$, $SD = 1.1279$. centre: $t(2214) = 0.755$, $p = 0.4505$, Tau+: $M = 0.235$, $SD = 0.382$, $n = 1210$, Tau-: $M = 0.248$, $SD = 0.424$, $n = 1006$, centre + background: $t(2197) = 1.13$, $p = 0.2605$, Tau+: $M = 0.255$, $SD = 1.02$, $n = 1203$, Tau-: $M = 0.306$, $SD = 1.13$, $n = 996$). Cells with bad fit in Tau+ mice also had significantly higher variability when stimuli were on in background regions ($t(2213) = -2.1473$, $p = 0.0319$, Tau+: $n = 1210$, $M = 12.7433$, $SD = 5.5258$. Tau-: $n = 1005$, $M = 12.2528$, $SD = 5.1351$), but not when centre or centre plus background stimuli were on (centre: $t(2176) = -0.987$, $p = 0.3238$, Tau+: $M = 29.1$, $SD = 13.8$, $n = 1187$, Tau-: $M = 28.5$, $SD = 12.9$, $n = 991$, centre +

background: $t(1746) = -1.38$, $p = 0.1688$, Tau+: $M = 28.9$, $SD = 17.5$, $n = 944$, Tau-: $M = 27.8$, $SD = 17.2$, $n = 804$). However for cells with bad fit, most cells were so untuned to spatial location that the 'centre' of the receptive field fit was usually just a particularly high noise value in an overall very noisy spatial response, so these results did not reflect a true centre/background divide, rather they might reflect instead the fact that because the background area was much larger than the centre area, there were many more times during stimulus presentation when stimuli were on in the background compared to the number of times a stimulus was on only in the centre, and so background measurements were more reliable.

In summary, the reduced fit quality for spatial receptive fields in Tau+ mice appears to be due to differences in the magnitude of firing rate changes in response to centre or background stimuli, and not because firing rates were more variable when stimuli were presented in one region versus another. As the z-scored firing rate was reduced in Tau+ mice when centre stimuli were on but higher than Tau- firing rates when only the background was on, both for all cells and cells with a clearly identifiable receptive field, the Tau+ mice have a reduced dynamic range for firing rates in response to stimuli at different spatial locations. This could explain why the Tau+ mice had lower fit quality across the V1 population.

5.3.3 Orientation

Orientation selectivity, like retinotopic receptive fields, is one of the most well known and robust types of cell response within V1. I assessed orientation selectivity in my mice by fitting a dual von Mises distribution to each cell response (Fig. 5.4a), from which I calculated orientation and direction selectivity measures as well as fit quality.

Tau+ mice had higher fit quality for direction tuning than Tau- mice (Fig. 5.4b, $Z = -7.8905$, $p < 0.0001$, Tau+: $n = 1058$, median = 0.6763, Tau-: $n = 1033$, median = 0.5841) as well as higher orientation selectivity (Fig. 5.4c, $Z = -5.8891$, $p < 0.0001$, Tau+: $n = 772$, median = 0.5859, Tau-: $n = 640$, median = 0.4816) although direction selectivity was similar in the two groups (Fig. 5.4d, $Z = -0.942$, $p = 0.3460$, Tau+: $n = 772$, median = 0.2281, Tau-: $n = 640$, median = 0.2246).

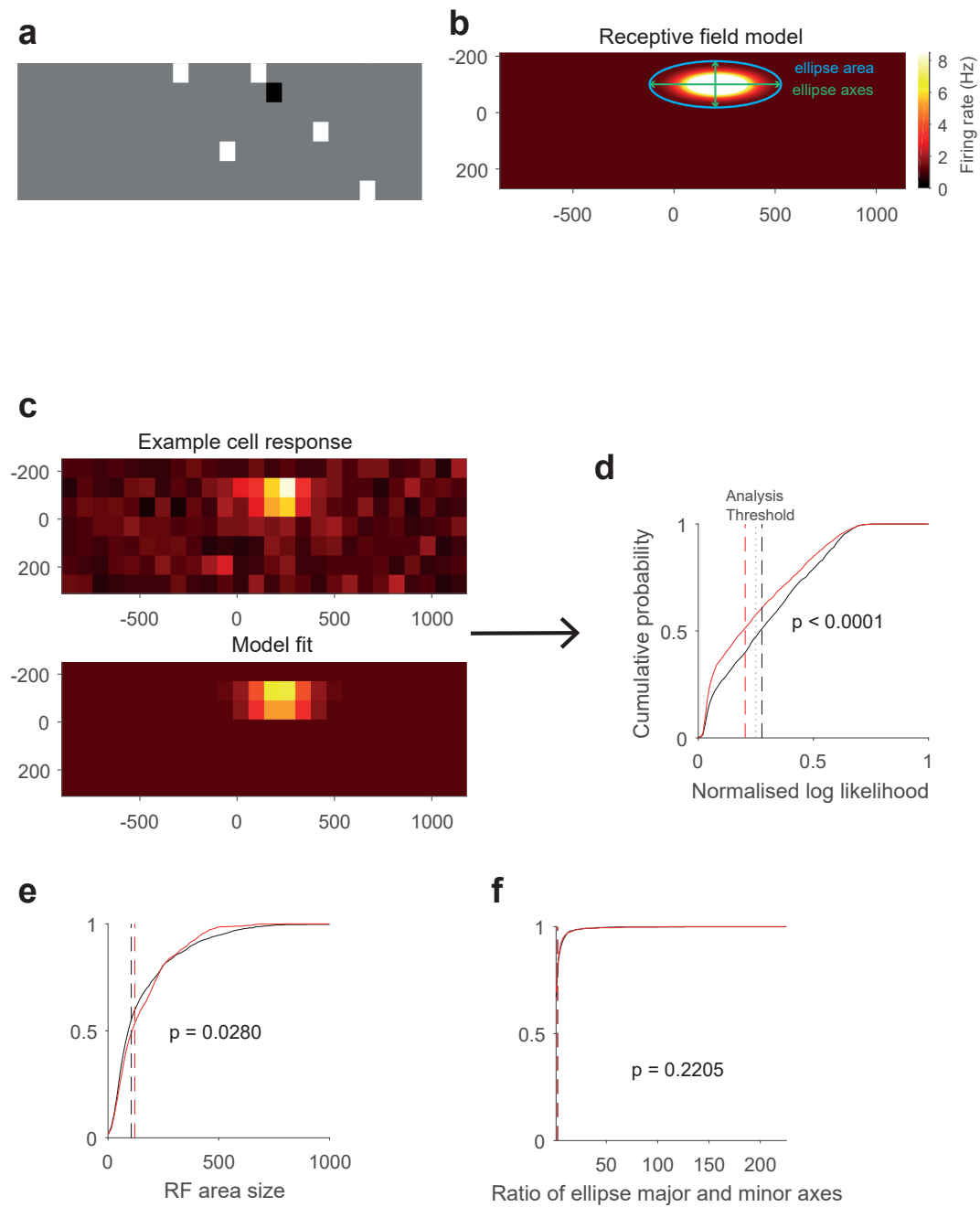


Figure 5.2: Tau+ mice have noisier spatial receptive fields. (a) Example frame from a sparse noise stimulus movie. Black and white squares appear and disappear at predetermined points during the sparse noise movie. (b) Spatial receptive field model. We modelled the firing rate of the cell at each stimulus point using a tilted 2D gaussian. (c) An example cell response to white squares and model fit below. (d) Fit quality (normalised log likelihood) was lower in Tau+ mice compared to Tau- mice across all V1 cells (e) Receptive field area size (calculated as the size of the ellipse from model fits) was slightly larger in Tau+ mice. (f) There was no difference between the groups in the ratio between ellipse major and minor axes.

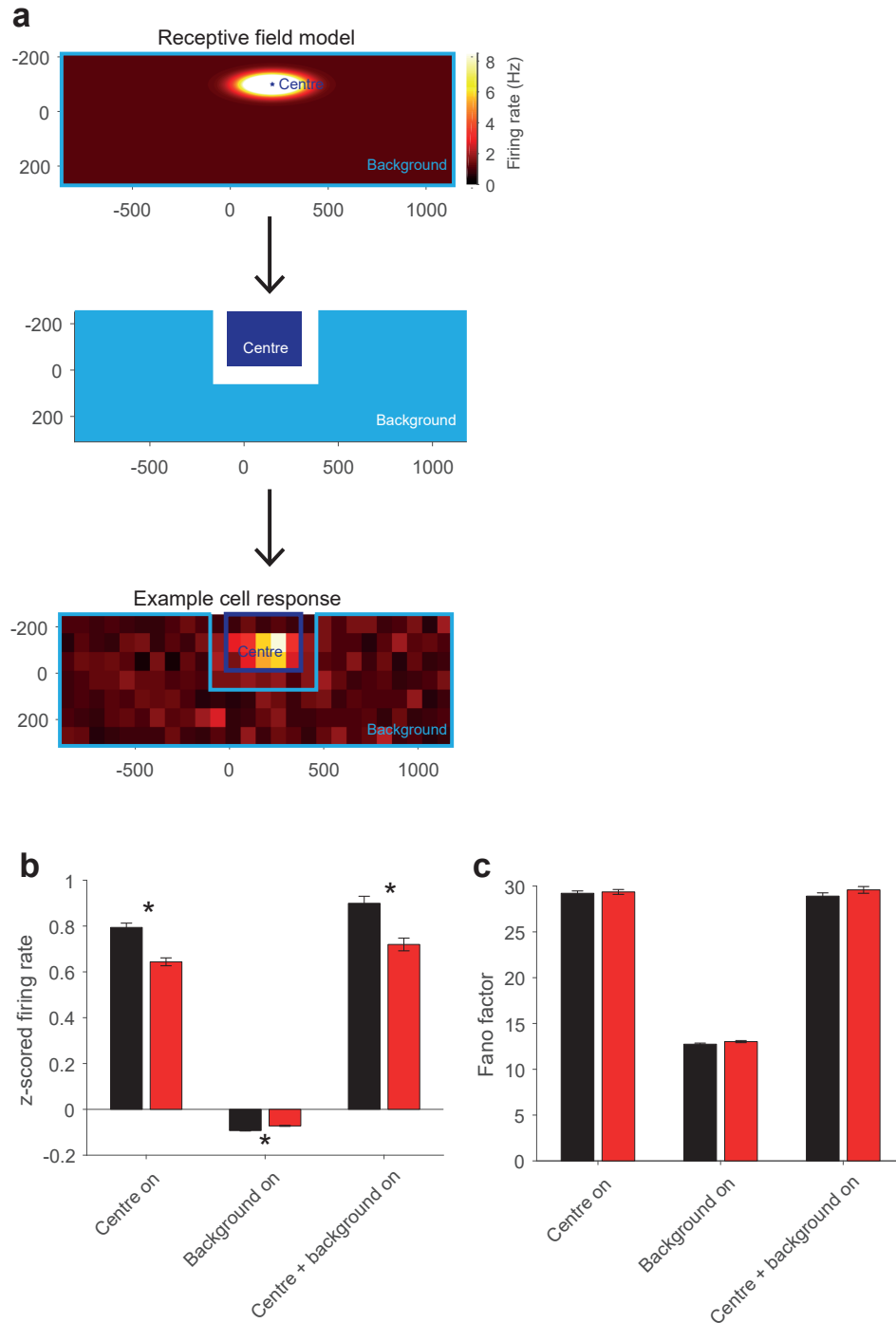


Figure 5.3: Dynamic range of firing during sparse noise is reduced in Tau+ mice. (a) Determining centre and background regions for an example cell. From the tilted gaussian model, we took the centre co-ordinates of the ellipse and found the nearest stimulus presentation point, and defined the centre zone as this point plus all adjacent points on each side, such that the centre zone was at maximum 24 deg on each side, since stimulus presentation points were 8 deg apart. The immediately adjacent points to the centre zone were excluded from analysis, and all remaining areas were labelled as background. (b) z-scored firing rates during times when stimuli were present in the centre only (centre on), background only (background on) or both (centre and background on). Firing rates were z-scored using the entire sparse noise recording session for that cell. (c) Fano factor for centre on, background on, and centre + background on times.

Finding an enhancement of orientation selectivity was a very surprising result, given that the only previous work in V1 of Tg4510 mice had shown no changes in orientation selectivity at a later timepoint (8-10 months) where tau pathology, as well as gross brain atrophy, are far more advanced (Kuchibhotla et al., 2014).

I looked in more detail at the model fits for Tau+ and Tau- mice to understand what was driving this enhancement in orientation tuning in Tau+ mice. Figure 5.4e shows the mean fitted tuning curves for Tau+ and Tau- mice, centred on the preferred orientation. These tuning curves showed that at the neuron's preferred orientation, Tau+ firing rates were similar to Tau- firing rates, but at the non-preferred orientation, Tau+ firing rates were reduced. As the orientation selectivity index compared the fitted response at the preferred and non-preferred orientations, this would explain why Tau+ mice had higher orientation selectivity.

Individual comparisons between model parameters in Tau+ and Tau- mice, such as tuning width ($Z = 0.798$, $p = 0.4251$, Tau-: $n = 640$, median = 37, Tau+: $n = 772$, median = 37), preferred orientation ($Z = 0.724$, $p = 0.4693$, Tau-: $n = 640$, median = 182, Tau+: $n = 772$, median = 180), peak height (peak 1: $Z = -0.7$, $p = 0.4838$, Tau-: $n = 640$, median = 10.1, Tau+: $n = 772$, median = 11.2, peak 2: $Z = -1.5$, $p = 0.1337$, Tau-: $n = 640$, median = 5.43, Tau+: $n = 772$, median = 6.61) and baseline ($Z = 1.08$, $p = 0.2811$, Tau-: $n = 640$, median = 0.862, Tau+: $n = 772$, median = 0.722), were all non-significant.

OSI calculated from the f1 response was also significantly higher in Tau+ mice ($Z = -4.3339$, $p < 0.0001$, Tau+: $n = 1058$, median = 0.5127, Tau-: $n = 1034$, median = 0.4426), while DSI and the proportion of simple to complex cells in V1 (measured by f1/f0 ratio) was not different between the groups (DSI: $Z = 1.63$, $p = 0.1027$, Tau-: $n = 1034$, median = 0.359, Tau+: $n = 1058$, median = 0.325, f1/f0 ratio: $Z = -0.486$, $p = 0.6272$, Tau-: $n = 1034$, median = 0.786, Tau+: $n = 1058$, median = 0.828).

5.3.4 Orientation adaptation

Another aspect of tauopathy-driven changes I was keen to investigate was changes in temporal dynamics. As described in the introduction to this chapter, Menkes-

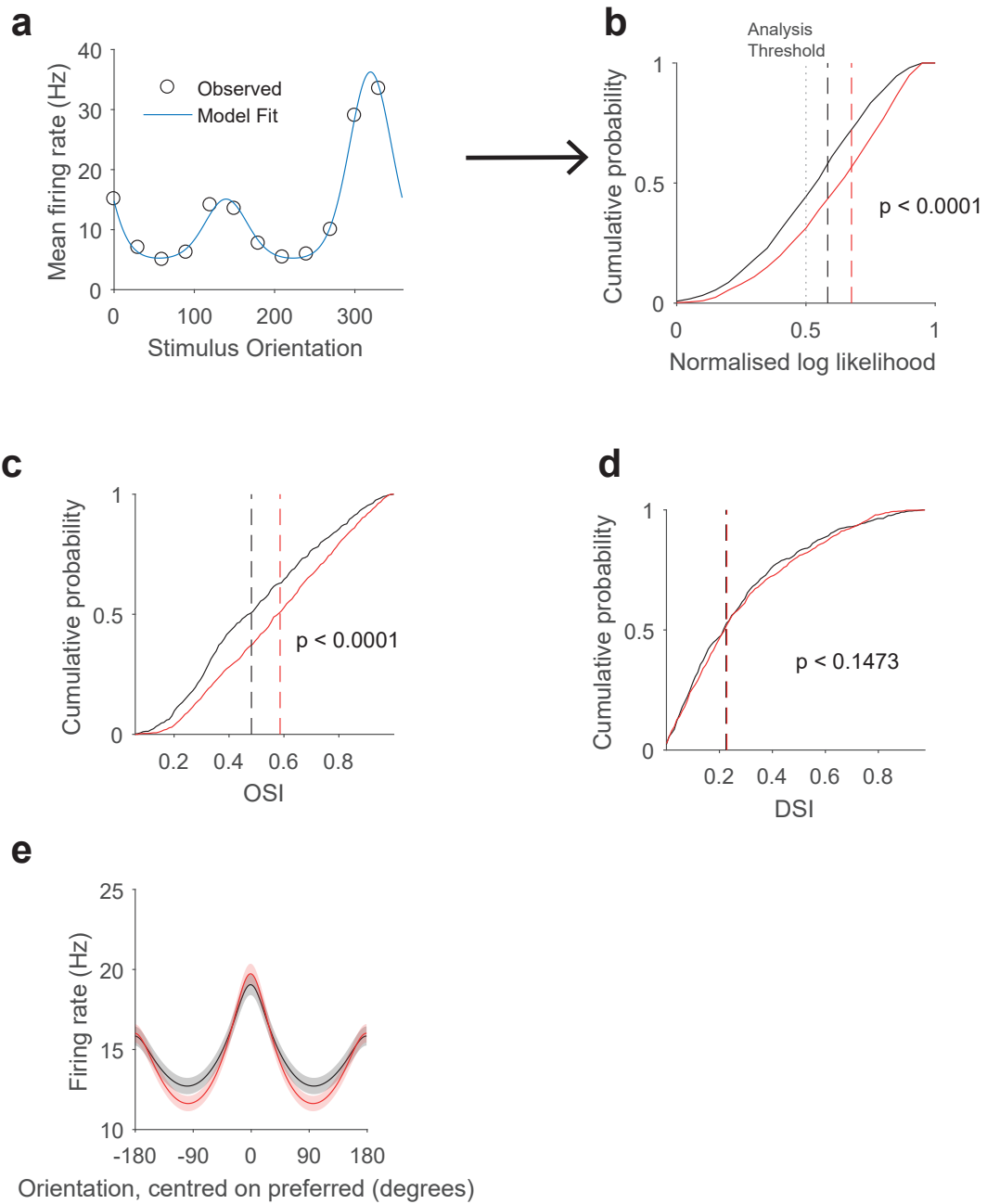


Figure 5.4: V1 populations in Tau+ mice are more well tuned for orientation. (a) Example cell response and model fit. Cell responses were fit using a dual von Mises distribution. (b) Fit quality, measured by normalised log likelihood, was higher in Tau+ mice than Tau- mice. (c) Orientation selectivity index was calculated from model fits in cells that passed the analysis threshold ($NLL > 0.5$). Tau+ mice had higher OSI in the V1 population than Tau- mice. (d) Direction selectivity was calculated from model fits and did not differ between groups. (e) Mean orientation tuning curves for Tau+ and Tau- mice, centred on preferred orientation.

Caspi et al. (2015) have observed abnormalities in state changes under anaesthesia in Tg4510 mice, which might reflect altered temporal dynamics. To understand this I looked at orientation adaptation, where, instead of a gray screen in the interval, an oriented drifting grating with 90 deg orientation was presented (more details in Chapter 3).

I first confirmed that results in the pre-adaptation block matched results in our orientation protocol. Test stimuli were the same in both orientation and orientation pre-adaptation protocols, but the pre-adaptation interstimulus interval was 4s instead of 1s, and fewer cells were recorded in the adaptation protocol as it was run less frequently.

Fit quality (Fig. 5.5b, $Z = -3.1144$, $p = 0.0018$, Tau+: $n = 505$, median = 0.6679, Tau-: $n = 458$, median = 0.6100) and orientation selectivity (not shown, $Z = -2.3558$, $p = 0.0185$, Tau+: $n = 505$, median = 0.3658, Tau-: $n = 458$, median = 0.2955) were indeed both enhanced in Tau+ mice in the pre-adaptation block. Fit quality was also higher in Tau+ mice in the adaptation block (Fig. 5.5c) and the post-adaptation block (not shown, adaptation NLL: $Z = -2.597$, $p = 0.0094$, Tau+: $n = 505$, median = 0.6338, Tau-: $n = 458$, median = 0.5880; post-adaptation NLL: $Z = -3.5004$, $p = 0.0005$, Tau+: $n = 505$, median = 0.6311, Tau-: $n = 458$, median = 0.5843)

To look at adaptation effects, I compared the suppression index between the groups. I first looked at suppression during the adaptation block by comparing the pre-adaptation response to the response during adaptation (Fig. 5.6a). There was higher suppression in Tau+ neurons both at the preferred orientation (Fig. 5.6b, $Z = -2.0975$, $p = 0.0360$, Tau+: $n = 236$, median = 0.1245, Tau-: $n = 191$, median = 0.0557) and the adaptor orientation (Fig. 5.6b, $Z = -3.7008$, $p = 0.0002$, Tau+: $n = 236$, median = 0.1736, Tau-: $n = 191$, median = 0.0605).

I also investigated the persistence of adaptation effects by calculating the suppression index using the pre-adaptation and post-adaptation blocks (Fig. 5.6d). Remaining suppression effects during the post-adaptation block were not significantly different at the preferred orientation (Fig. 5.6e $Z = -1.54$, $p = 0.1244$,

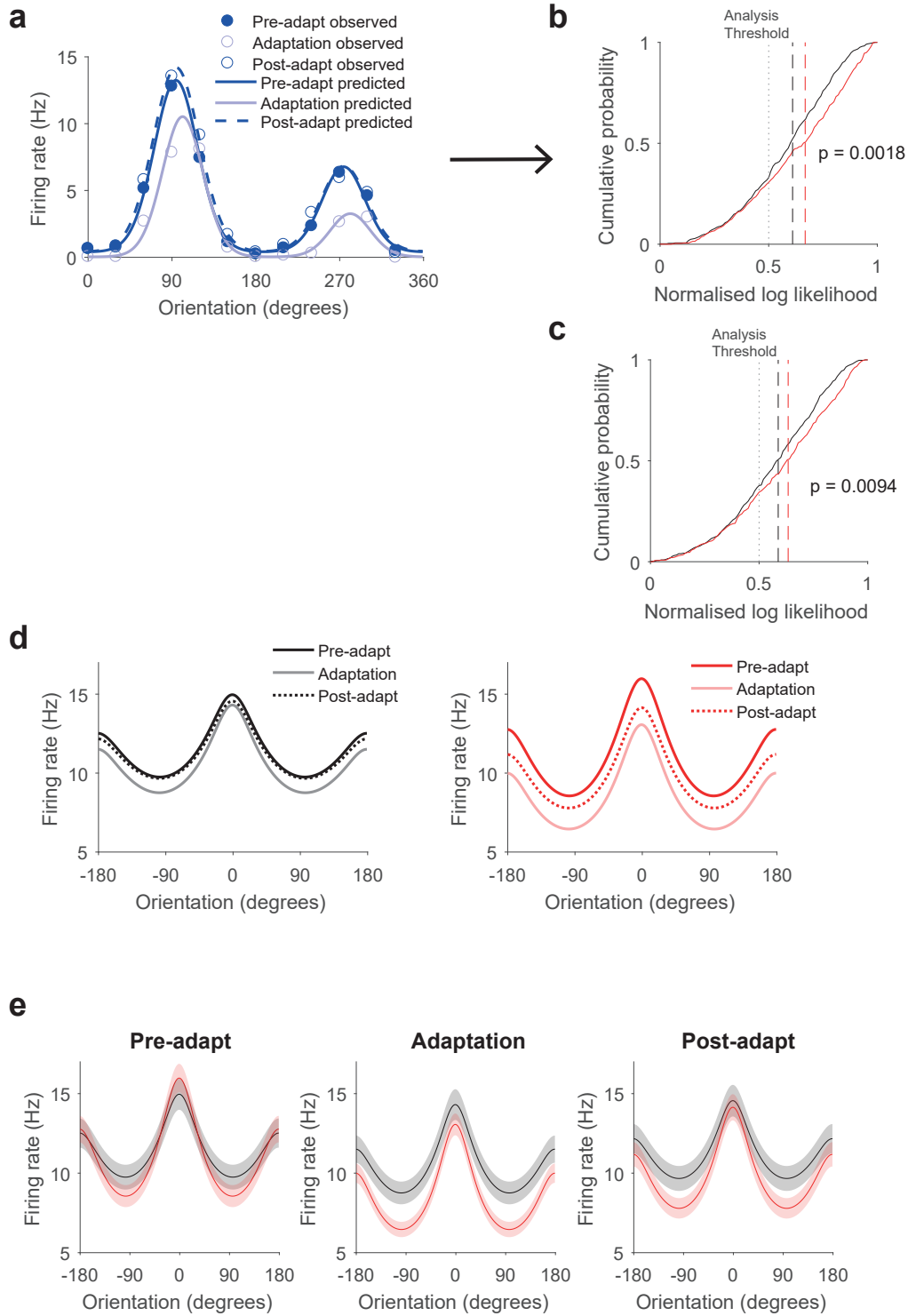


Figure 5.5: Orientation tuning is enhanced during adaptation in Tau+ mice. (a) An example neuron showing observed responses and model fits for pre-adaptation, adaptation and post-adaptation block. The same dual von Mises equation that had been used to fit orientation responses in Figure 5.4 was used to fit responses in all three adaptation conditions. (b) Fit quality for cells in the pre-adaptation block. (c) Fit quality for cells in the adaptation block. (d) Mean tuning curves for all conditions, for Tau+ and Tau- mice separately. (e) Mean tuning curves with error bars (error bars show SEM) for pre-adaptation, adaptation and post-adaptation blocks.

Tau-: $n = 187$, median = 0.0179, Tau+: $n = 237$, median = 0.0605) but Tau+ neurons showed a larger amount of suppression at the adaptor orientation (Fig. 5.6f, $Z = -2.0888$, $p = 0.0367$, Tau+: $n = 237$, median = 0.0489, Tau-: $n = 187$, median = -0.0087).

In summary, Tau+ mice showed more suppression than Tau- mice, and this suppression effect persisted at the adaptor orientation even after a 5 minute recovery period.

5.3.5 Contrast

Contrast tuning is another well known feature of the early visual system, first observed in the retina (Naka and Rushton, 1966) but also present in V1 neurons (Niell and Stryker, 2008, in mouse). As contrast tuning is mostly inherited from structures that should not be affected by tauopathy in the Tg4510 (retina and LGN), it should remain normal in the Tau+ mice.

In fact, Tau+ mice had higher fit quality for contrast tuning compared to Tau- mice (Fig. 5.7b, $Z = -2.4233$, $p = 0.0154$, Tau+: $n = 363$, median = 0.7796, Tau-: $n = 341$, median = 0.6169). However, signed sigma (C_{50} , where the contrast tuning curve reaches half of its maximum value, $Z = -0.154$, $p = 0.8776$, Tau-: $n = 199$, median = 46.2, Tau+: $n = 245$, median = 45.3) and signed sensitivity (a measurement of the slope of the tuning curve, $Z = -0.124$, $p = 0.9012$, Tau-: $n = 199$, median = 0.0401, Tau+: $n = 245$, median = 0.0438) were not significantly different between the groups, as shown in Figure 5.7c and Figure 5.7d respectively. The baseline parameter ($Z = 0.673$, $p = 0.5009$, Tau-: $n = 199$, median = 7.5, Tau+: $n = 245$, median = 7.66) and gain (R_{max}) parameter ($Z = 0.316$, $p = 0.7522$, Tau-: $n = 199$, median = 5.14, Tau+: $n = 245$, median = 5.07) also showed no difference between the groups. Mean tuning curves (Fig. 5.7e and 5.7f) also did not show any clear differences. Hence, the higher fit quality for contrast tuning in Tau+ mice could not be explained by any single change in tuning.

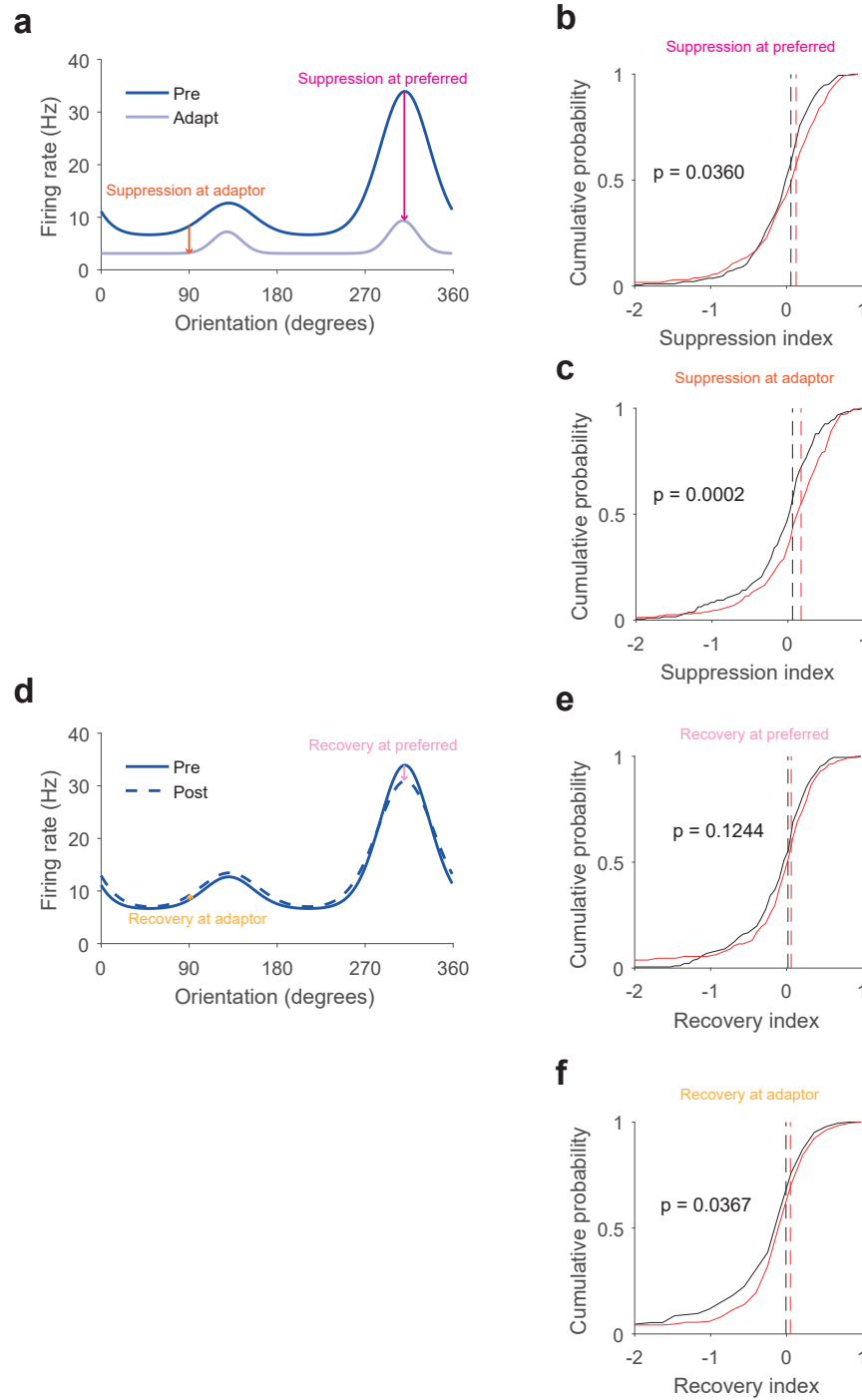


Figure 5.6: Tau+ mice show greater suppression due to adaptation than Tau- mice.

(a) Example orientation tuning curves to pre-adaptation and adaptation blocks from a single neuron. Adaptor and preferred orientations are indicated by coloured arrows. (b) Suppression index for Tau+ and Tau- mice calculated at each cell's preferred orientation. All suppression index plots are cut off at -2 and 1 to standardise between plots. (c) Suppression index for Tau+ and Tau- mice calculated at the adaptor orientation (90 degrees) (d) Example orientation tuning curves for pre-adaptation and post-adaptation blocks from the same neuron as in (a). (e) Suppression index for Tau+ and Tau- mice calculated at the preferred orientation. (f) Suppression index for Tau+ and Tau- mice calculated at the adaptor orientation.

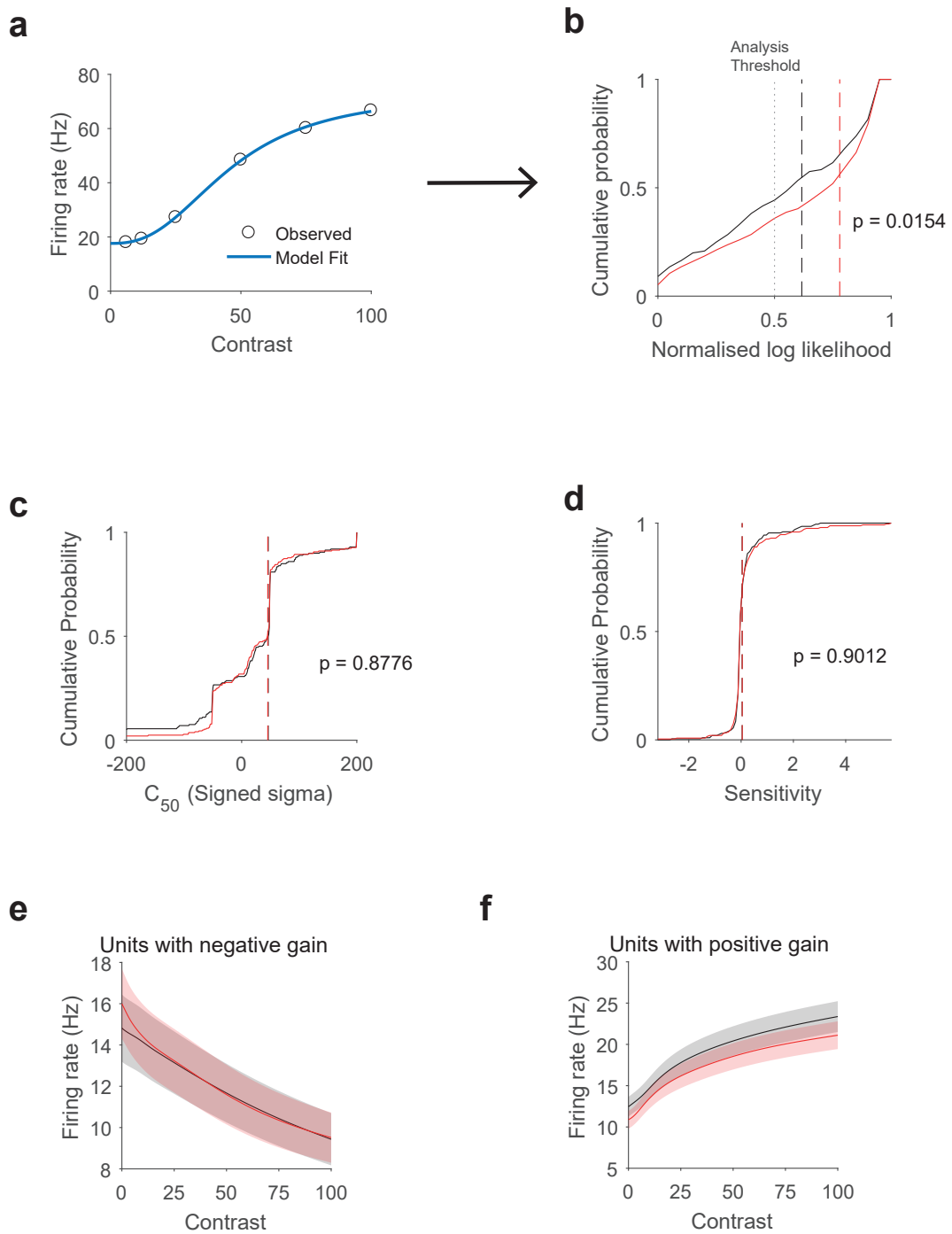


Figure 5.7: Contrast tuning is enhanced in Tau+ mice. (a) Example responses to contrast stimuli and fitted tuning curve and tuning curve equation. (b) Fit quality for contrast tuning in Tau+ and Tau- mice. (c) Signed sigma in Tau+ and Tau- mice (d) Sensitivity in Tau+ and Tau- mice (e) Mean tuning curves for units with negative gain. (f) Mean tuning curves for units with positive gain

5.3.6 Size

Size tuning, specifically, the surround suppression effects seen in response to large stimuli, is thought to reflect local inhibition within the cortex, which should be disrupted by tau pathology in the Tau+ mice. If cortical synapses were preferentially affected by tau pathology (compared to subcortical connections), size tuning would be worse in Tau+ mice, with reduced suppression to large stimuli.

However, after fitting size tuning curves to all neurons (Fig. 5.8a), Tau+ and Tau- mice showed no difference in fit quality (Fig. 5.8b, $Z = -1.03$, $p = 0.3014$, Tau-: $n = 455$, median = 0.752, Tau+: $n = 329$, median = 0.772). There was also no significant difference between the groups in preferred size (Fig. 5.8c, $Z = -0.042$, $p = 0.9665$, Tau-: $n = 313$, median = 41.2, Tau+: $n = 233$, median = 41), suppression index (Fig. 5.8d, $Z = -1.62$, $p = 0.1053$, Tau-: $n = 313$, median = -0.0507 , Tau+: $n = 233$, median = -0.0502), or in the baseline parameter of the model ($Z = 1.08$, $p = 0.2791$, Tau-: $n = 313$, median = 6.25, Tau+: $n = 233$, median = 5.3). Mean tuning curves for neurons with a smaller preferred size (Fig. 5.8e) and larger preferred size (Fig. 5.8f) also did not look very different, with only a small decrease in firing rate.

Because size tuning is very sensitive to the position of the stimulus in relation to a neuron's receptive field, I then conducted a secondary analysis of these results, using the sparse noise sessions run on the same day as size tuning sessions to determine the receptive field centre for neurons recorded during size tuning sessions, and restricted analysis to neurons where the centre of the drifting grating for the size protocol was within 20 degrees of the receptive field centre of the neuron calculated from the sparse noise model, and where neurons passed the fit quality threshold ($NLL > 0.5$) for size. Following this, there were no significant differences between Tau+ and Tau- mice in fit quality ($Z = 0.355$, $p = 0.7225$, Tau-: $n = 78$, median = 0.821, Tau+: $n = 41$, median = 0.807), preferred size ($Z = -0.66$, $p = 0.5093$, Tau-: $n = 78$, median = 16.6, Tau+: $n = 41$, median = 17.5) or suppression index ($Z = -0.26$, $p = 0.7948$, Tau-: $n = 78$, median = 0.332, Tau+: $n = 41$, median = 0.342).

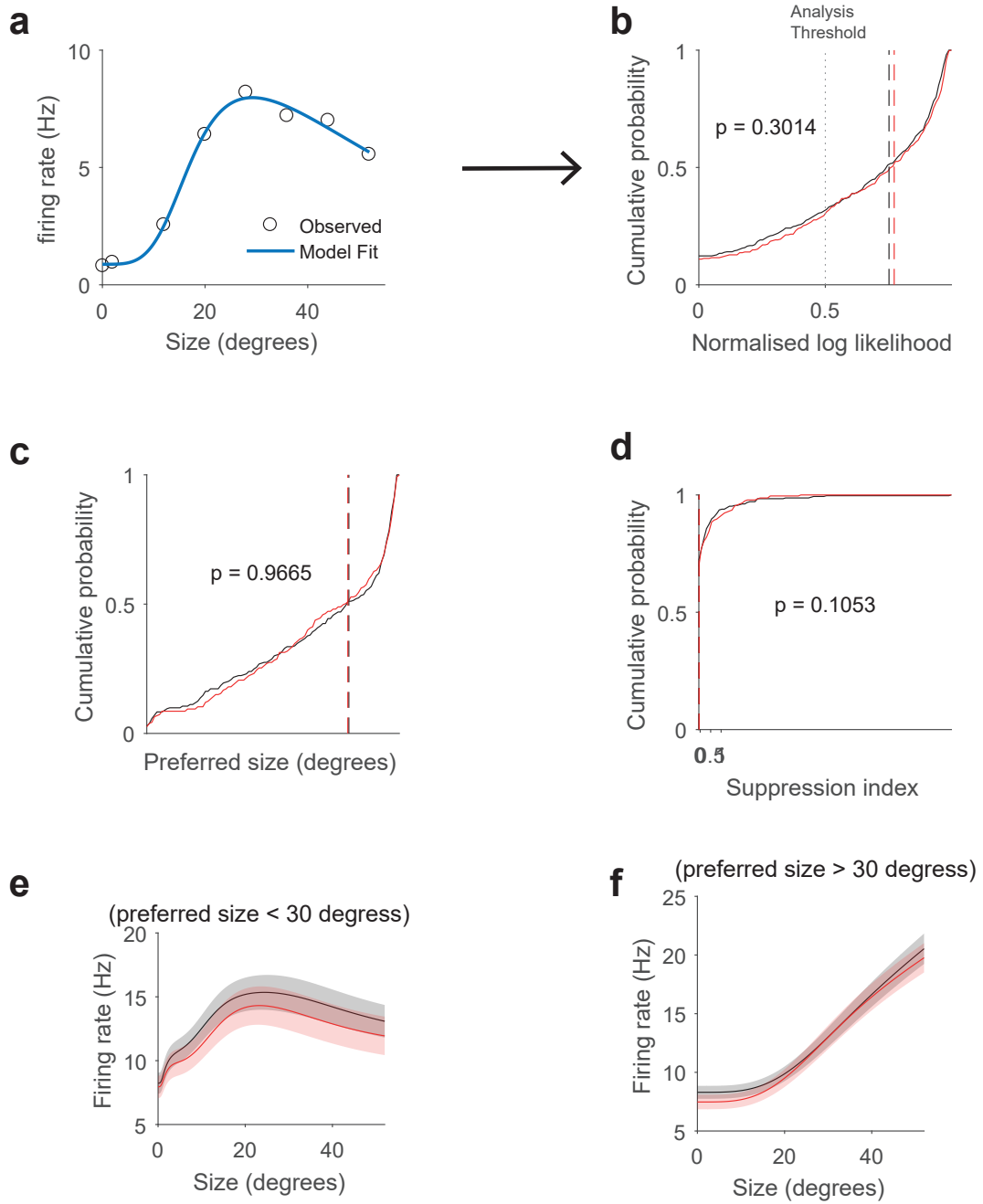


Figure 5.8: Size tuning is not changed in Tau+ mice. (a) Example observed response and model fit (b) Fit quality for Tau+ and Tau- neurons (c) Preferred size for Tau+ and Tau- neurons (d) Suppression index for Tau+ and Tau- neurons (e) Mean tuning curves for neurons with a small preferred size (less than 30 degrees) (f) Mean tuning curves for neurons with large preferred size (greater than 30 degrees)

5.3.7 Spatial frequency

Finally I also considered spatial frequency tuning. Like size tuning, Tau+ mice and Tau- mice showed no difference in normalised log likelihood (Fig. 5.9a, $Z = -0.33$, $p = 0.741$, Tau-: $n = 345$, median = 0.856, Tau+: $n = 363$, median = 0.846) or any other spatial frequency measure considered, such as preferred spatial frequency (Fig. 5.9c, $Z = 0.966$, $p = 0.3341$, Tau-: $n = 274$, median = 0.0429, Tau+: $n = 280$, median = 0.04), tuning width (Fig. 5.9d, $Z = 0.442$, $p = 0.6587$, Tau-: $n = 274$, median = 0.106, Tau+: $n = 280$, median = 0.0928) or low SF roll off (Fig. 5.9e, $Z = -0.0244$, $p = 0.9806$, Tau-: $n = 274$, median = 0.22, Tau+: $n = 280$, median = 0.227).

5.4 Discussion

5.4.1 Firing rate reduction in Tau+ mice

I observed a general reduction in the firing rate of Tau+ visual cortical neurons in Tg4510 mice when mice are awake and behaving. This agrees with the findings of Menkes-Caspi et al. (2015) and Jackson et al. (2017) where firing rate reductions were observed in other cortical areas. As my recordings were extracellular, it is not possible to identify the cause of firing rate reductions from my experiments alone, but a likely explanation for the firing rate reduction is that it reflects the state changes observed in Menkes-Caspi et al. (2015), possibly explained by the changes in spine turnover observed by Jackson et al. (2017), where alterations in pre-synaptic and post-synaptic stability might lead to an overall reduction in synaptic efficacy where stable synapses between neurons are less likely to form.

Although my findings agree with previous research, the experimental conditions for acquiring a baseline measure of firing rate in visual cortex were not ideal. One problem with my firing rate reduction results is that the stimulus OFF period did not really constitute a true baseline period because of the stimulus preceding each ISI. Ideally, baseline firing rates in V1 should have been acquired during a prolonged gray screen presentation. Unfortunately, given the nature of our experiments with the different groups and complex Dox assignment and surgery, it was

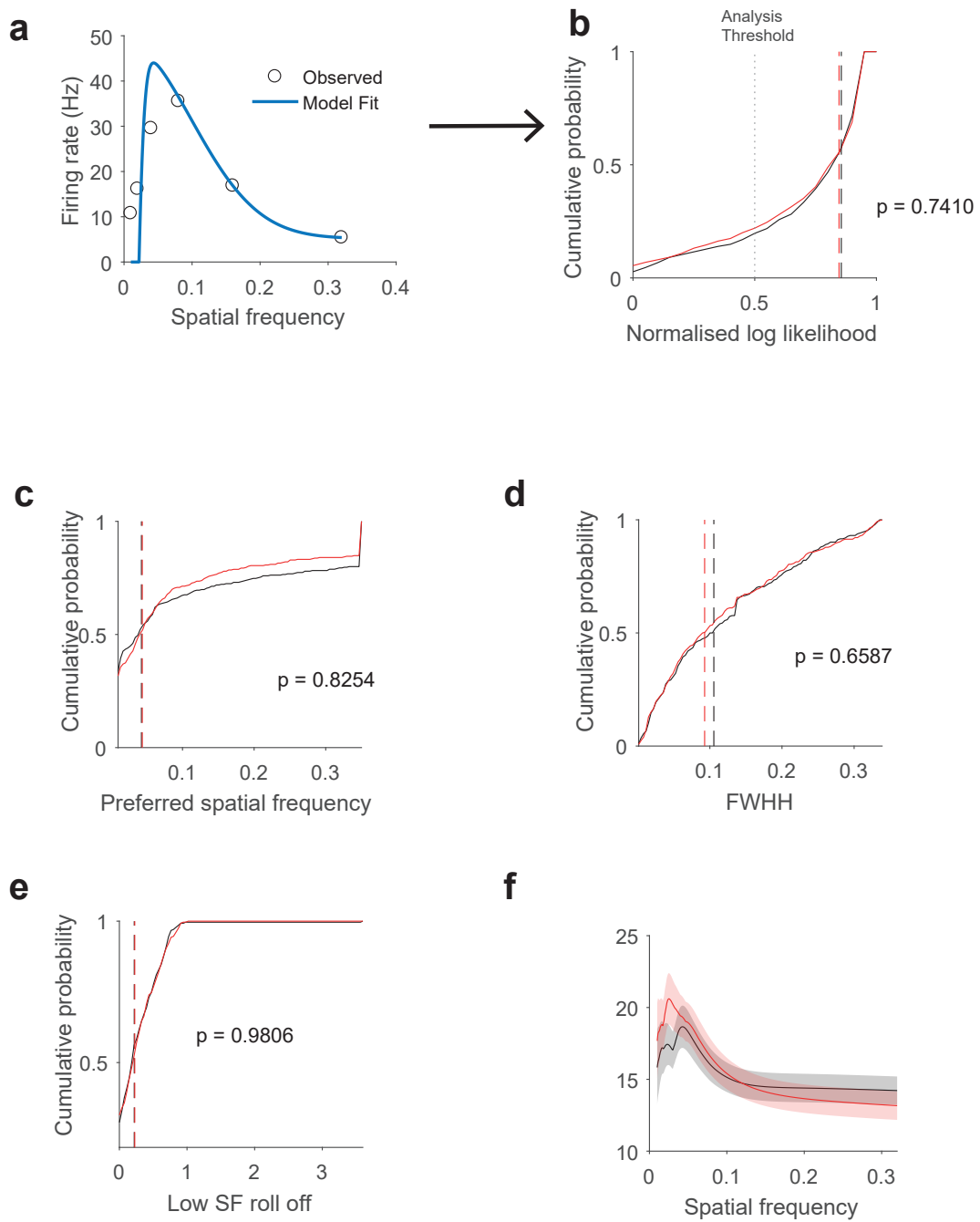


Figure 5.9: Spatial frequency tuning is not changed in Tau+ mice. (a) Example observed response and tuning curve for spatial frequency. (b) Fit quality for Tau+ and Tau- neurons (c) Preferred spatial frequency for Tau+ and Tau- neurons (d) Tuning width (FWHH) for Tau+ and Tau- neurons (e) Roll off for Tau+ and Tau- neurons

not possible to conduct any more experiments with new mice, so I tried looking through sessions which had already been acquired for other points of comparison. Firing rates during VR dark sessions, which were completely in the dark, and also during the 30 gray screen period preceding the pre-adaptation block were somewhat reduced in Tau+ mice, but not significantly so (dark: $t(334) = 0.956$, $p = 0.3395$, Tau-: $n = 130$, $M = 8.75$, $SD = 10.7$, Tau+: $n = 130$, $M = 8.75$, $SD = 10.7$, gray screen prior to pre-adaptation block: $t(993) = 0.838$, $p = 0.4022$, Tau-: $n = 484$, $M = 7.6$, $SD = 8.76$, Tau+: $n = 484$, $M = 7.6$, $SD = 8.76$). However, the number of neurons sampled under these conditions were lower compared to comparisons collapsing across visual protocols (hundreds compared to thousands of neurons). Firing rates during sparse noise, where stimuli were small black and white squares rather than large drifting gratings, and where most of the screen was still gray, did show a significant reduction ($t(4429) = 2.4794$, $p = 0.0132$, Tau+: $n = 2201$, $M = 7.4857$, $SD = 8.6802$; Tau-: $n = 2230$, $M = 8.1704$, $SD = 9.6665$).

Since this firing rate reduction was observed in all these different conditions, even though some of the reductions were not significant, I believe it is reasonable to conclude that these results reflect a true firing rate reduction in the Tau+ mice.

Another question which arises from these results is why differences in firing rate between Tau+ and Tau- mice are greater in some protocols but not others. Differences in firing rate by protocol did not match up with differences in model fits or tuning curve parameters. Orientation and contrast protocols, which showed differences in fit quality between the groups, had more similar mean firing rates, but spatial frequency, which had no fit differences, also had similar mean firing rates between Tau+ and Tau- mice. The size protocol had a larger difference in mean firing rate between Tau+ and Tau- mice but showed no differences in fit quality or tuning. Therefore, mean firing rate differences did not appear to be driven by differences in tuning or selectivity.

Another possibility was that differences between the protocols in stimulus duration or ISI might explain the differences in mean firing rate. Based on the enhanced adaptation effects in Tau+ mice, it could be that each stimulus presentation

would cause some level of adaptation depending on the duration of the stimulus presentation, and there would be more or less recovery depending on the duration of the ISI. However, when I looked at firing rate differences plotted against either stimulus duration or ISI, no clear trend emerged.

A final possible explanation is stimulus size - while most protocols had a stimulus diameter of 35 deg, the size and annulus size protocols, which varied stimulus size up to a maximum of 52 deg, showed the largest differences in firing rate. However if large stimuli had a greater effect on firing rate, this should have affected size tuning, particularly size suppression, but no differences were observed in size suppression in these experiments. The question of whether firing rate really does change with stimulus size may be an interesting area for future analysis. It may be the case that size tuning was not run often enough, compared to protocols like orientation and sparse noise, for effects to be clearly observed. In particular, further analysis of the centre-surround protocol, where each stimulus was repeated 100 times instead of 20 as in other protocols, might be useful in exploring size effects.

The protocol-specific differences in Tau + and Tau - firing rate also persisted during the interstimulus intervals when no stimulus was on the screen and only a gray background was shown. This suggests that adaptation effects might be contributing to differences in firing rate in some protocols. I discuss adaptation effects further in a later section.

5.4.2 Deficits in response to sparse noise in Tau+ mice

The deficits in sparse noise tuning are perhaps the most consistent with the firing rate reductions in Tg4510 mice that I and other researchers have observed. Reduced firing rates in Tau+ mice would directly explain the reduced dynamic range for differentiating centre and background regions in the Tau+ mice.

Some caveats with the results are that the centre versus background definition I picked does not really make sense for noisy responses with no clear receptive field, where the receptive field centre defined by the model is just a particularly high noise value. However, no other definition would fare any better given that the problem is a lack of receptive field in the cell response rather than a poorly defined centre

region from the model. In addition, an analysis of centre vs background responses in good responses only ($NLL > 0.25$) still showed significantly reduced z-scored firing rate in both background and centre regions, confirming the analysis run on all cells.

A second caveat is whether the result of receptive field area size being slightly larger in Tau+ mice is meaningful, as the size difference between Tau+ and Tau- receptive fields was not very large compared to the size of the stimuli (squares with sides of 8 degrees), and mouse visual acuity is quite poor. Furthermore, the y axis length of the receptive field was significantly different between Tau+ mice and Tau- mice but the x axis length was not, which seems odd. A true receptive field size difference would probably expand in both horizontal and vertical directions. One possibility is that due to the way the experiment was set up, with three monitors surrounding the mouse, much of the visual field was covered in the horizontal compared to the vertical direction, and perhaps some of the receptive fields measurements were cut off due to running out of screen in the vertical direction. To investigate this further it would be best to look perhaps also at the position of receptive fields across the monitors to see if one group had more at the top or bottom of the monitors.

5.4.3 Normal size tuning in Tau+ mice

Given the known changes in synaptic function in Tg4510 mice (Jackson et al., 2017), and the deficits in sparse noise tuning that I observed including a minor increase in receptive field area in Tau+ mice, it was surprising that there was no overall deficit in size tuning in Tau+ mice, either in fit quality or in suppression. In particular, I would have expected to see a large reduction in suppression in Tau+ mice in size tuning, as suppression is thought to be driven by local inhibition within V1 (Self et al., 2014) which I would expect to be disrupted by the synaptic changes in Tau+ mice. However my results did not show any changes in surround suppression.

One problem with the size tuning analysis was that size tuning is very sensitive to stimulus location. If the location of the stimulus is too far away from a neuron's

receptive field centre, the recorded size tuning curve will not reflect the true size tuning of the neuron as only larger stimuli will elicit a response. This was addressed by restricting a second round of analysis to only cells which had receptive field centres within 20 degrees of the stimulus. However this had the effect of reducing the number of cells in the analysis which may have made it more difficult to detect effects.

Another reason sparse noise and size tuning results are different may be because of the number of times each protocol was run - the sparse noise protocol was run almost daily with 4335 cells recorded in total, whereas size tuning was only run every few days with 784 cells recorded in total.

Alternatively, it may be the case that surround suppression is not affected by the synaptic changes seen in Tau+ mice at this intermediate stage of pathology, either because the synapses involved are not affected by pathology, or because the synapses are affected by pathology but still functional. It is unclear what the functional consequences of the changes in spine turnover, density etc observed by Jackson et al. (2017) would be, and my experiments are not able to distinguish between these options. One argument for some pathology-affected neurons being functional is given by Kuchibhotla et al. (2014)'s observation that NFT-bearing neurons had normal orientation selectivity in 8-10 month old Tg4510 mice, but it is not clear whether these findings from a later timepoint would be applicable to my own experiments - especially given my own findings in orientation selectivity.

5.4.4 Contrast enhancement in Tau+ mice

I also observed a small enhancement in contrast tuning in Tau+ mice, although it was not entirely clear what this represented as there were no differences in any other model parameters or obvious changes in the mean model fits. Given this, it is difficult to interpret what exactly the contrast enhancement represents. The improved fit quality cannot be explained as either a change in baseline or in overall maximum firing rate, as both were similar in Tau+ and Tau- mice,

One interesting possibility is that perhaps only robust, well-tuned cells survive in the Tau+ mice, but this gives rise to the questions of how and why tau pathol-

ogy should be able to distinguish between well tuned and poorly tuned cells, and why enhancement only occurs for certain types of selectivity (contrast, orientation). Furthermore, at this stage of pathology we should not expect a large amount of cell death.

Contrast tuning, like many types of feature selectivity in V1, is a complex phenomenon which is partly inherited from retina and LGN, but also mediated by local processing within cortex (see Carandini and Heeger, 2011, for a review). Contrast tuning also interacts with the size of the stimulus (Nienborg et al., 2013; Cavanaugh et al., 2002). A potential explanation for the contrast enhancement we see may be that feedforward contrast information is preserved but local changes to contrast tuning are disrupted, leading to an overall 'enhancement' of contrast tuning.

5.4.5 Orientation selectivity enhancement in Tau+ mice

Another surprising result was the orientation selectivity enhancement I observed in Tau+ mice. Kuchibhotla et al. (2014)'s previous study in 8-10 month old Tg4510 mice found normal orientation selectivity in NFT-bearing neurons, but no enhancements. What my results have shown is that this previously observed normal selectivity at a late stage of tauopathy does not necessarily reflect a straightforward preservation of function throughout the course of neurodegeneration, but rather different changes in selectivity (enhancement, disruption, similarity) may be seen at different stages of tauopathy and may reflect changing effects on the neural population as the tauopathy progresses.

Another difference between my study and Kuchibhotla et al. (2014)'s work are that I used electrophysiology rather than calcium imaging, allowing me to sample from all layers rather than just the superficial layers. I have not yet performed an analysis of cell responses by layer, but this would be an interesting area for follow up work to see whether the enhancements can be localised to any specific layer or occur throughout the cortex. For example, it could be possible that layer 2/3 cells have normal orientation tuning like Kuchibhotla et al. (2014) found at their later timepoint, and other changes are occurring in different layers.

Excitatory neurons in V1 have higher orientation selectivity than inhibitory

neurons, which are more broadly tuned (Hofer et al., 2011; Kerlin et al., 2010). One interesting explanation for the orientation selectivity enhancement in Tau+ mice could be that excitatory neurons survive whereas inhibitory neurons are more affected by tauopathy - although this would be a strange result given that tau expression in the Tg4510 is driven by CaMKII which should be restricted to pyramidal neurons (Ramsden et al., 2005). A follow up analysis to look at this possibility could be to divide recorded neurons into excitatory and inhibitory groups based on their spike width and compare OSI within these groups in Tau+ and Tau- mice.

Perhaps the most compelling explanation of the orientation selectivity enhancement is a lower tendency to fire in Tau+ neurons, as observed by Menkes-Caspi et al. (2015) in frontal cortex. This could explain the reduced baseline at non-preferred orientations, as input is weaker and less likely to pass the threshold for firing, and the normal firing rates at the preferred orientation, where input is strong enough to overcome the lowered tendency to fire. This would also tie in with the reduced firing rates observed in my experiments, and could also provide an explanation for the contrast tuning enhancement. Contrast changes might produce enough of a difference. However, it is not clear from this why some kinds of selectivity are unaffected. Perhaps due to the nature of the protocols I ran, where only one stimulus dimension was varied during each session, many of the stimuli were sub-optimal to varying degrees. If all the stimuli in the size protocol were at a sub-optimal orientation, for example, there might be an overall reduction in firing rate, but no single stimulus would generate the input required to cause a normal or enhanced response.

5.4.6 Enhanced orientation adaptation effects in Tau+ mice

Tau+ mice displayed an increased magnitude of suppression following orientation adaptation, and the duration of the adaptation effect also appeared to be prolonged. Adaptation effects in V1 are complex (see Solomon and Kohn, 2014, for review) and it is unclear from previous work in Tg4510 mice what might be driving this increased suppression effect, as temporal effects on neuronal firing have not been much explored. One study by Gelman et al. (2017) finds that measures of short

term plasticity, like paired pulse facilitation, are reduced in Tg4510 mice, but it is not clear how these results can explain our findings which are on the timescale of minutes, while paired pulse facilitation is a much more short term effect.

One intriguing possibility is that the enhanced adaptation effects may reflect similar mechanisms to what drives increased duration of down states and fewer successful up states in Tg4510 mice (Menkes-Caspi et al., 2015). Menkes-Caspi et al. (2015) observed that neurons in Tg4510 mice not only had reduced firing rates, but also had altered subthreshold membrane potential dynamics. They suggested that both these effects could be driven by a general breakdown of synaptic input efficiency, where the dysfunction of tau-affected neurons affects the properties of the entire network. Neurons in the affected network are then 'reluctant to fire' - difficult to drive beyond their firing threshold. The prolonged suppression we observed could similarly be due to problems with synaptic input efficiency. Prolonged adaptation might provide a strong enough stimulus to drive the network into a suppressed state, and overcome the synaptic deficiencies within the network. However when the adaptor stimulus is removed, because of the poor synaptic efficiency, the network is not able to quickly recover back to normal levels of activity.

5.5 Summary and conclusions

Overall, I observed a varied profile of changes in feature selectivity in Tau+ mice, many of which did not follow predictions based on previous work. Orientation selectivity and contrast tuning were enhanced, but responses to a sparse noise stimulus were disrupted. Firing rates were also reduced across multiple visual protocols.

The enhancements and disruptions I observed may reflect synaptic changes which have previously been observed in this mouse model, and different effects in various visual protocols may reflect how effective the stimuli in that protocol are at driving firing in V1 neurons. Following from this, future work could explore this hypothesis further either by comparing responses to optimal versus sub-optimal stimuli, or exploring whether the effect is limited to certain subsets of neurons e.g. excitatory versus inhibitory, or layer specific.

Another important unsolved question is what underlies the adaptation effects seen in my Tg4510 mice, for example identifying the mechanism leading to this effect or conducting further experiments to understand under what conditions these adaptation enhancements manifest. This line of research is already being pursued by my collaborators.

Chapter 6

General Conclusions

In my thesis, I have explored the effects of tau pathology on the information processing capabilities of neural populations in the Tg4510 mouse. In this final chapter, I summarise my results and discuss potential applications of my research.

6.1 Selecting the Tg4510 mouse

I began in Chapter 2 by comparing two mouse models, one with amyloid pathology (J20) and one with tau pathology (Tg4510) on an alternating T-maze task. Both groups of mice showed behavioural deficits. J20 mice had reduced high-frequency power in prefrontal cortex and reduced theta-gamma phase-amplitude coupling at the 5-6 month timepoint, together with increased CA1-PFC theta coherence, which appeared to show a promising change in LFP characteristics due to pathology. However, there were a large number of unexplained deaths in J20 mice before the cohort reached 10-11 months, making the 10-11 month timepoint results from the remaining mice very difficult to interpret. As I did not want my mice to die in the middle of my rather more complex T-maze experiments (not least because the probes were a lot more expensive) I decided to use the Tg4510 mouse for my head-fixed experiments.

In fact, the Tg4510 T-maze data from my collaborators showed a clear decline in CA1 power, CA1 phase-amplitude coupling and CA1-PFC coherence, and the magnitude of these effects clearly increased at each timepoint. Furthermore, other work in the Tg4510 model, by Lilly colleagues, also suggested that these changes

observed in the LFP during the T-maze task might be a lagging indicator of synaptic dysfunction that began to appear much earlier in the course of pathology (Jackson et al., 2017).

6.2 Changes in the local field potential at an early stage of tauopathy

To investigate this, in Chapter 4 I looked at evoked changes in LFP power in two conditions - running in closed loop, open loop or dark virtual reality environments, or changes in LFP power evoked by visual stimuli. There were interesting suggestive changes in Tau+ Tg4510 mice - lack of a flattening of the CA1 theta-running speed slope in open loop and dark running, and V1 narrowband gamma increase to contrast and size stimuli rather than the expected decrease. However none of these results were significant, and the only clear difference between the groups was a reduction in CA1 high-frequency power in the Tau+ mice.

From this we cannot definitively conclude that LFP measures are poor indicators of early tauopathy. It may be that the measures I have looked at do not change much, but other measures may show larger changes. For example, in my analysis of V1 unit firing in Chapter 5, I found Tau+ neurons had less effective spatial receptive fields. Spatial receptive fields can also be measured in the local field potential or with fMRI (Dumoulin and Wandell, 2008), and now I know that unit responses to sparse noise are altered, it would be interesting to see whether the field potential response changes as well.

It is perhaps not surprising, however, that I did not observe large changes in LFP power in my mice. The local field potential represents the pooled activity of many synapses, and may not be the most sensitive measure for tauopathy-driven changes, as large changes must occur across the entire population before measurable changes emerge in the LFP. However, there are still practical reasons to keep investigating LFP changes. LFP changes are far easier to measure in high-throughput experiments in mouse models, and are also perhaps more translatable to human work, as EEG can be recorded in human patients whereas single unit activity cannot be

non-invasively recorded.

6.3 Changes in V1 population feature tuning at an early stage of tauopathy

In Chapter 5, I observed a remarkable set of results in Tau+ mice. As well as observing a reduced firing rate in V1, which has been reported by other researchers in other cortical areas, I found that spatial receptive field responses to a sparse noise stimulus are disrupted due to this reduced firing rate and lack dynamic range. However, I observed an opposite effect in orientation selectivity, where Tau+ neurons were in fact more orientation selective. This was due to a reduced firing rate only at non-preferred orientations, but a normal firing rate at preferred orientations. Neurons in Tau+ mice also showed a greater amount of suppression due to orientation adaptation, and the effects also lasted longer than in neurons in Tau- mice. Contrast tuning was also slightly improved in neurons in Tau+ mice compared to Tau-.

Together, these results suggest that information processing in V1, and potentially other cortical areas, does not undergo a straightforward decline as a result of tauopathy. Instead, at this early stage of tauopathy different types of processing within the cortex are affected in diverse ways, which might result from tauopathy affecting certain parts of the cortical microcircuit more than others. An interesting area for future work would be to try to identify what mechanisms underlie these disparate effects, for example by isolating the contributions of different cell types.

In Chapter 5 I also discussed how my results, in conjunction with what we already know about V1 function and mechanisms, can explain how cortical circuits are affected by tau pathology. The profile of results I observed did not point to a deficit in specific types of synapse or elements of the V1 microcircuit, but rather suggested that neurons in Tau+ mice might have a lowered tendency to fire. Differences in adaptation, orientation tuning and contrast tuning then arise from this broader network dysfunction. If this is the case, perhaps only stimuli which were optimised for driving each neuron would successfully cause the neuron to change its activity. One possibility is that the feed-forward mechanisms contributing to ori-

entation tuning are well preserved in Tau+ mice and therefore input to V1 neurons is more biased towards information about orientation, rather than other visual information that is dependent on local synaptic integration. An interesting follow up experiment would be to present a range of stimuli varying across two dimensions. For example, stimuli varying in orientation and contrast, or orientation and position in the receptive field, could be used to see whether responses of V1 neurons in Tau+ mice show greater differences when stimuli are varying degrees of 'optimal'.

Another very exciting area for follow up work is the analysis of unit firing in closed loop, open loop and dark running, which I was not able to complete during the course of this project. Saleem et al. (2018) recently showed that neurons in V1 and CA1 encode an animal's position in a virtual corridor, and given the deficits in spatial information and place fields that have been previously observed in this model (Cheng and Ji, 2013), alterations in position encoding in a virtual reality environment could also be expected in these mice. Furthermore, by linking activity in V1 and CA1, it will be possible to investigate unit firing both in an area which is known to be affected in Alzheimer's disease (CA1) and an area where we have much clearer models of single unit responses (V1). Hopefully, joining these two will give a clearer understanding of the effects of tauopathy.

6.4 Application of this project towards Alzheimer's disease

My work has shown that there are interesting alterations in visual cortical activity at an intermediate stage of tauopathy. There are a number of interesting followup studies that could be performed resulting from my research.

In mice, the most important application of my research would be to use changes in visual response as a functional marker of tauopathy. Drugs which aim to treat Alzheimer's (or other diseases) by clearing tau from the brain could be assessed based on whether the drug can reverse the functional changes I have observed. This would represent an important step forward in markers for drug development in Alzheimer's disease. Pathological markers such as tau or amyloid burden do not

directly measure disease symptoms, and as has been found with anti-amyloid drugs, pathology can be cleared while cognitive symptoms remain. For behavioural markers such as Morris Water Maze or T-maze performance, successful performance relies on the complex interaction of many brain areas and cognitive processes. Therefore while behavioural markers are translatable to the behavioural symptoms of Alzheimer's disease, they are less useful at dissociating specific cognitive processes of interest. Mice (and patients) can rescue task performance by developing alternative coping strategies to solve tasks. The most direct measure of cognitive processes is to look at brain activity itself - to obtain functional markers, rather than behavioural or pathological markers.

However, one of the key criteria for the use of functional markers in drug development is that they are easy to obtain and experiments can be run in a high-throughput manner. Therefore an obstacle to using my results for drug development is the complexity of my experiments. The specific types of experiments I performed - head fixed recordings using chronically implanted, driveable electrodes, capable of recording unit activity - are complex and invasive. Therefore my findings cannot be directly transferred to the clinic. However, there are ways in which my experiments could be adapted to be easier and faster to run. For example, a simpler experiment would be to use fixed instead of driveable electrodes, that only record field potentials and not units.

In my work the clearest differences between Tau+ and Tau- mice were in unit activity, not in LFP, but this may have partly been due to the specific types of activity and response I looked at in my LFP analyses. I mainly looked at changes in power with running speed, and in terms of responses to visual protocols, I only looked at the evoked response to a flash stimulus and broadband and narrowband gamma responses to contrast and size changes. My results with unit activity have identified some key types of stimulus that V1 neurons in Tau+ mice are particularly sensitive to and show a large difference from Tau- mice. To maximise the chances of finding differences in Tau+ and Tau- mice in the field potential, protocols could be chosen that have already shown large differences in unit activity.

One of the changes in unit activity which would be especially interesting to look at in the field potential response is adaptation. The greater adaptation effects I observed in the Tau+ mice were relatively insensitive to how different the adaptor orientation was from the preferred orientation of each single neuron. Therefore, the adaptation effects appear to be occurring across the entire population rather than just cells already tuned to a specific orientation. If the adaptation response is occurring across multiple cells, it should also be detectable in the field potential. Such an analysis could even be performed on my existing data.

It would also be interesting to try adaptation experiments using stimuli other than oriented gratings, which need to be placed in a specific location in the receptive field. Ideally, functional assays for drug development would be high-throughput and simple to perform, and if the head fixation aspect of these experiments could be removed so the mice could be freely moving, this would make the experiments much easier to run.

It would also be interesting to look at the ERP in response to different stimuli, especially in adaptation protocols or protocols with prolonged stimulation. In particular, based on the changes in adaptation response in the Tau+ mice, a useful analysis to perform would be to see if the timecourse of the ERP changes, as well as looking at the amplitude of the components. Although, I did not observe a change in the evoked response to a full screen flash stimulus in my mice, this might be due to the choice of stimulus rather than a problem with ERP as a measure of cortical (and subcortical) function. Protocols could also be used which are known to cause changes in the VEP. For example, Cooke and Bear (2010) presented the same stimuli over multiple days. With these multiple presentations, mice display stimulus-specific response potentiation of the evoked potential in V1, where the amplitude of the VEP increases with repeated presentations. Cooke and Bear (2010) show that stimulus-specific response potentiation in V1 is driven by similar mechanisms to LTP. LTP is known to be impaired in the Tg4510 mouse, as well as in many other Alzheimer's models (Hoover et al., 2010; Saganich et al., 2006; Larson et al., 1999). This, together with my adaptation findings, makes stimulus-specific

response potentiation an excellent candidate for a potential functional marker for drug development. Local field potential changes, and especially changes in ERP, would also be useful to understand in mice because similar experiments can also be performed in humans using EEG or MEG. This would allow direct translation to the clinic.

In humans, visual protocols are likely to be of limited use in Alzheimer's disease, given that tau pathology does not reach the visual cortex until quite late in the disease. However, my findings can be directly translated to patients with posterior cortical atrophy, a type of dementia where tauopathy occurs in the visual regions of the brain. Not only could recording experiments be performed, but also simpler psychophysics experiments. For example, patients could be shown adaptation stimuli and given perceptual judgement tasks following the adaptation to assess the magnitude and recovery timecourse of adaptation. Experiments with collaborators are already taking place in patients with posterior cortical atrophy to determine whether my findings are of use in the clinic for diagnosis. The plan is to use visual adaptation protocols in conjunction with EEG or MEG to determine whether PCA patients show similar changes in visual adaptation to what I have found in my experiments.

6.5 Conclusion

I have shown clear changes in visual cortex in a tauopathy model of Alzheimer's disease, which demonstrates that V1 can in fact be used as a useful model for pathology-driven functional changes. Furthermore, the selective alterations of selectivity I have observed in the Tg4510 mouse are quite different from most previous studies in the visual cortex of Alzheimer's models, which either report disruptions or normal activity. In my experiments, I have found that enhancement of selectivity is also possible at some stages of neurodegeneration.

The wider goal of this research, which I hope others will continue to work on, is to understand functional changes in neural populations which are relevant to patients, rather than changes that can be explained as being specific to one particular model. This will require further research in different mouse models and

different brain areas, to see if these V1 results reflect general principles of the effect of neurodegeneration on cortical processing. My research has, I hope, offered an intriguing window into this general problem.

Bibliography

- Adesnik, H. (2017). Synaptic mechanisms of feature coding in the visual cortex of awake mice. *Neuron*, 95(5):1147 – 1159.e4.
- Adesnik, H., Bruns, W., Taniguchi, H., Huang, Z. J., and Scanziani, M. (2012). A neural circuit for spatial summation in visual cortex. *Nature*, 490(7419):226.
- Alzheimer’s Association (2015). 2015 Alzheimer’s disease facts and figures. *Alzheimer’s & Dementia*, 11(3):332–384.
- Ameen-Ali, K. E., Simpson, J. E., Wharton, S. B., Heath, P. R., Sharp, P., Brezzo, G., and Berwick, J. (2018). The time course of recognition memory impairment and glial pathology in the happ-j20 mouse model of alzheimer’s disease. *bioRxiv*.
- Amieva, H., Jacqmin-Gadda, H., Orgogozo, J.-M., Carret, N. L., Helmer, C., Letenneur, L., Barberger-Gateau, P., Fabrigoule, C., and Dartigues, J.-F. (2005). The 9 year cognitive decline before dementia of the Alzheimer type: a prospective population-based study. *Brain*, 128(5):1093–1101.
- Aronov, D. and Tank, D. W. (2014). Engagement of Neural Circuits Underlying 2D Spatial Navigation in a Rodent Virtual Reality System. *Neuron*, 84(2):442–456.
- Ayaz, A., Saleem, A., Schölvinck, M., and Carandini, M. (2013). Locomotion controls spatial integration in mouse visual cortex. *Current Biology*, 23(10):890 – 894.
- Bäckman, L., Jones, S., Berger, A.-K., Laukka, E. J., and Small, B. J. (2005). Cognitive impairment in preclinical Alzheimer’s disease: A meta-analysis. *Neuropsychology*, 19(4):520–531.

- Bäckman, L., Small, B. J., and Fratiglioni, L. (2001). Stability of the preclinical episodic memory deficit in Alzheimer's disease. *Brain*, 124(1):96–102.
- Bannerman, D., Deacon, R., Offen, S., Friswell, J., Grubb, M., and Rawlins, J. (2002). Double dissociation of function within the hippocampus: spatial memory and hyponeophagia. *Behavioral neuroscience*, 116(5):884.
- Bannerman, D., Yee, B., Good, M., Heupel, M., Iversen, S., and Rawlins, J. (1999). Double dissociation of function within the hippocampus: a comparison of dorsal, ventral, and complete hippocampal cytotoxic lesions. *Behavioral neuroscience*, 113(6):1170.
- Barker, W. W., Luis, C. A., Kashuba, A., Luis, M., Harwood, D. G., Loewenstein, D. ., Waters, C., Jimison, P., Shepherd, E., Sevush, S., Graff-Radford, N., Newland, D., Todd, M., Miller, B., Gold, M., Heilman, K., Doty, L., Goodman, I., Robinson, B., Pearl, G., Dickson, D., and Duara, R. . (2002). Relative Frequencies of Alzheimer Disease, Lewy Body, Vascular and Frontotemporal Dementia, and Hippocampal Sclerosis in the State of Florida Brain Bank. *Alzheimer Disease & Associated Disorders*, 16(4):203–212.
- Bejanin, A., Schonhaut, D. R., La Joie, R., Kramer, J. H., Baker, S. L., Sosa, N., Ayakta, N., Cantwell, A., Janabi, M., Lauriola, M., O'Neil, J. P., Gorno-Tempini, M. L., Miller, Z. A., Rosen, H. J., Miller, B. L., Jagust, W. J., and Rabinovici, G. D. (2017). Tau pathology and neurodegeneration contribute to cognitive impairment in Alzheimers disease. *Brain*, 140(12):3286–3300.
- Bekris, L. M., Yu, C.-E., Bird, T. D., and Tsuang, D. W. (2010). Genetics of alzheimer disease. *Journal of geriatric psychiatry and neurology*, 23(4):213–227.
- Bender, F., Gorbati, M., Cadavieco, M. C., Denisova, N., Gao, X., Holman, C., Korotkova, T., and Ponomarenko, A. (2015). Theta oscillations regulate the speed of locomotion via a hippocampus to lateral septum pathway. *Nature Communications*, 6:8521 EP –.

- Benilova, I., Karran, E., and De Strooper, B. (2012). The toxic A β oligomer and Alzheimer's disease: an emperor in need of clothes. *Nature Neuroscience*, 15(3):349–357.
- Berisha, F., Feke, G. T., Trempe, C. L., McMeel, J. W., and Schepens, C. L. (2007). Retinal Abnormalities in Early Alzheimer's Disease. *Investigative Ophthalmology & Visual Science*, 48(5):2285–2289.
- Blackmore, T., Meftah, S., Murray, T. K., Craig, P. J., Blockeel, A., Phillips, K., Eastwood, B., O'Neill, M. J., Marston, H., Ahmed, Z., Gilmour, G., and Gastambide, F. (2017). Tracking progressive pathological and functional decline in the rtg4510 mouse model of tauopathy. *Alzheimers Res Ther*, 9(1):77–77.
- Bliss, T. V. and Collingridge, G. L. (1993). A synaptic model of memory: long-term potentiation in the hippocampus. *Nature*, 361(6407):31.
- Bliss, T. V. and Lømo, T. (1973). Long-lasting potentiation of synaptic transmission in the dentate area of the anaesthetized rabbit following stimulation of the perforant path. *The Journal of physiology*, 232(2):331–356.
- Bolmont, T., Clavaguera, F., Meyer-Luehmann, M., Herzig, M. C., Radde, R., Staufenbiel, M., Lewis, J., Hutton, M., Tolnay, M., and Jucker, M. (2007). Induction of tau pathology by intracerebral infusion of amyloid- β -containing brain extract and by amyloid- β deposition in app \times tau transgenic mice. *The American journal of pathology*, 171(6):2012–2020.
- Bomben, V., Holth, J., Reed, J., Cramer, P., Landreth, G., and Noebels, J. (2014). Bexarotene reduces network excitability in models of Alzheimer's disease and epilepsy. *Neurobiology of aging*.
- Booth, C. A., Ridler, T., Murray, T. K., Ward, M. A., de Groot, E., Goodfellow, M., Phillips, K. G., Randall, A. D., and Brown, J. T. (2016). Electrical and network neuronal properties are preferentially disrupted in dorsal, but not ventral, medial entorhinal cortex in a mouse model of tauopathy. *Journal of Neuroscience*, 36(2):312–324.

- Braak, H. and Braak, E. (1991). Neuropathological staging of Alzheimer-related changes. *Acta Neuropathologica*, 82(4):239–259.
- Braak, H. and Braak, E. (1996). Evolution of the neuropathology of Alzheimer's disease. *Acta Neurologica Scandinavica*, 94(S165):3–12.
- Bramblett, G. T., Goedert, M., Jakes, R., Merrick, S. E., Trojanowski, J. Q., and Lee, V. M. (1993). Abnormal tau phosphorylation at ser396 in alzheimer's disease recapitulates development and contributes to reduced microtubule binding. *Neuron*, 10(6):1089 – 1099.
- Buchwald, J. S., Erwin, R. J., Read, S., Van Lancker, D., and Cummings, J. L. (1989). Midlatency auditory evoked responses: differential abnormality of p1 in alzheimer's disease. *Electroencephalography and Clinical Neurophysiology/Evoked Potentials Section*, 74(5):378–384.
- Busche, M. A., Chen, X., Henning, H. A., Reichwald, J., Staufenbiel, M., Sakmann, B., and Konnerth, A. (2012). Critical role of soluble amyloid- β for early hippocampal hyperactivity in a mouse model of Alzheimer's disease. *Proceedings of the National Academy of Sciences*, 109(22):8740–8745.
- Busche, M. A., Eichhoff, G., Adelsberger, H., Abramowski, D., Wiederhold, K.-H., Haass, C., Staufenbiel, M., Konnerth, A., and Garaschuk, O. (2008). Clusters of Hyperactive Neurons Near Amyloid Plaques in a Mouse Model of Alzheimer's Disease. *Science*, 321(5896):1686–1689.
- Busche, M. A., Kekuš, M., Adelsberger, H., Noda, T., Förstl, H., Nelken, I., and Konnerth, A. (2015). Rescue of long-range circuit dysfunction in Alzheimer's disease models. *Nature Neuroscience*, 18(11):1623–1630.
- Bussey, T. J., Duck, J., Muir, J. L., and Aggleton, J. P. (2000). Distinct patterns of behavioural impairments resulting from fornix transection or neurotoxic lesions of the perirhinal and postrhinal cortices in the rat. *Behavioural Brain Research*, 111(1):187 – 202.

- Buzsáki, G., Anastassiou, C. A., and Koch, C. (2012). The origin of extracellular fields and currents — EEG, ECoG, LFP and spikes. *Nature Reviews Neuroscience*, 13(6):407–420.
- Cacucci, F., Yi, M., Wills, T. J., Chapman, P., and O’Keefe, J. (2008). Place cell firing correlates with memory deficits and amyloid plaque burden in Tg2576 Alzheimer mouse model. *Proceedings of the National Academy of Sciences*, 105(22):7863–7868.
- Carandini, M., Demb, J. B., Mante, V., Tolhurst, D. J., Dan, Y., Olshausen, B. A., Gallant, J. L., and Rust, N. C. (2005). Do We Know What the Early Visual System Does? *The Journal of Neuroscience*, 25(46):10577–10597.
- Carandini, M. and Heeger, D. J. (2011). Normalization as a canonical neural computation. *Nature Reviews Neuroscience*, 13:51–62.
- Cardin, J. A., Carlén, M., Meletis, K., Knoblich, U., Zhang, F., Deisseroth, K., Tsai, L.-H., and Moore, C. I. (2009). Driving fast-spiking cells induces gamma rhythm and controls sensory responses. *Nature*, 459:663 EP –.
- Cavanaugh, J. R., Bair, W., and Movshon, J. A. (2002). Nature and interaction of signals from the receptive field center and surround in macaque v1 neurons. *Journal of Neurophysiology*, 88(5):2530–2546.
- Chapman, P. F., White, G. L., Jones, M. W., Cooper-Blacketer, D., Marshall, V. J., Irizarry, M., Younkin, L., Good, M. A., Bliss, T., Hyman, B. T., et al. (1999). Impaired synaptic plasticity and learning in aged amyloid precursor protein transgenic mice. *Nature neuroscience*, 2(3):271.
- Chen, G., King, J. A., Burgess, N., and O’Keefe, J. (2013). How vision and movement combine in the hippocampal place code. *Proceedings of the National Academy of Sciences*, 110(1):378–383.
- Chen, G., King, J. A., Lu, Y., Cacucci, F., and Burgess, N. (2018). Spatial cell

- firing during virtual navigation of open arenas by head-restrained mice. *eLife*, 7:e34789.
- Cheng, I. H., Searce-Levie, K., Legleiter, J., Palop, J. J., Gerstein, H., Bien-Ly, N., Puolivali, J., Lesne, S., Ashe, K. H., Muchowski, P. J., and Mucke, L. (2007). Accelerating Amyloid-beta Fibrillization Reduces Oligomer Levels and Functional Deficits in Alzheimer Disease Mouse Models. *Journal of Biological Chemistry*, 282(33):23818–23828.
- Cheng, J. and Ji, D. (2013). Rigid firing sequences undermine spatial memory codes in a neurodegenerative mouse model. *eLife*, 2:e00647.
- Cirrito, J. R., Yamada, K. A., Finn, M. B., Sloviter, R. S., Bales, K. R., May, P. C., Schoepp, D. D., Paul, S. M., Mennerick, S., and Holtzman, D. M. (2005). Synaptic Activity Regulates Interstitial Fluid Amyloid- β Levels In Vivo. *Neuron*, 48(6):913–922.
- Cissé, M., Sanchez, P. E., Kim, D. H., Ho, K., Yu, G.-Q., and Mucke, L. (2011). Ablation of cellular prion protein does not ameliorate abnormal neural network activity or cognitive dysfunction in the J20 line of human amyloid precursor protein transgenic mice. *The Journal of Neuroscience*, 31(29):10427–10431.
- Citron, M., Oltersdorf, T., Haass, C., McConlogue, L., Hung, A. Y., Seubert, P., Vigo-Pelfrey, C., Lieberburg, I., and Selkoe, D. J. (1992). Mutation of the β -amyloid precursor protein in familial alzheimer's disease increases β -protein production. *Nature*, 360(6405):672.
- Clair, D. M. S., Blackwood, D. H. R., and Christie, J. E. (1985). P3 and other long latency auditory evoked potentials in presenile dementia alzheimer type and alcoholic korsakoff syndrome. *British Journal of Psychiatry*, 147(6):702706.
- Clark, V. P., Fan, S., and Hillyard, S. A. (1994). Identification of early visual evoked potential generators by retinotopic and topographic analyses. *Human brain mapping*, 2(3):170–187.

- Clark, V. P. and Hillyard, S. A. (1996). Spatial selective attention affects early extrastriate but not striate components of the visual evoked potential. *Journal of Cognitive Neuroscience*, 8(5):387–402.
- Clavaguera, F., Akatsu, H., Fraser, G., Crowther, R. A., Frank, S., Hench, J., Probst, A., Winkler, D. T., Reichwald, J., Staufenbiel, M., et al. (2013). Brain homogenates from human tauopathies induce tau inclusions in mouse brain. *Proceedings of the National Academy of Sciences*, 110(23):9535–9540.
- Clavaguera, F., Bolmont, T., Crowther, R. A., Abramowski, D., Frank, S., Probst, A., Fraser, G., Stalder, A. K., Beibel, M., Staufenbiel, M., et al. (2009). Transmission and spreading of tauopathy in transgenic mouse brain. *Nature cell biology*, 11(7):909.
- Colgin, L. L. (2016). Rhythms of the hippocampal network. *Nature Reviews Neuroscience*, 17(4):239–249.
- Cooke, S. F. and Bear, M. F. (2010). Visual experience induces long-term potentiation in the primary visual cortex. *Journal of Neuroscience*, 30(48):16304–16313.
- Coon, K. D., Myers, A. J., Craig, D. W., Webster, J. A., Pearson, J. V., Lince, D. H., Zismann, V. L., Beach, T. G., Leung, D., Bryden, L., et al. (2007). A high-density whole-genome association study reveals that apoe is the major susceptibility gene for sporadic late-onset alzheimer’s disease. *The Journal of clinical psychiatry*, 68(4):613–618.
- Corkin, S. (2002). What’s new with the amnesic patient hm? *Nature reviews neuroscience*, 3(2):153.
- Crimins, J. L., Rocher, A. B., and Luebke, J. I. (2012). Electrophysiological changes precede morphological changes to frontal cortical pyramidal neurons in the rtg4510 mouse model of progressive tauopathy. *Acta Neuropathologica*, 124(6):777–795.

- Croner, L. J. and Kaplan, E. (1995). Receptive fields of p and m ganglion cells across the primate retina. *Vision Research*, 35(1):7 – 24.
- Czurkó, A., Hirase, H., Csicsvari, J., and Buzsóki, G. (2001). Sustained activation of hippocampal pyramidal cells by space clamping in a running wheel. *European Journal of Neuroscience*, 11(1):344–352.
- de Calignon, A., Fox, L. M., Pitstick, R., Carlson, G. A., Bacskai, B. J., Spires-Jones, T. L., and Hyman, B. T. (2010). Caspase activation precedes and leads to tangles. *Nature*, 464(7292):1201.
- De Calignon, A., Polydoro, M., Suárez-Calvet, M., William, C., Adamowicz, D. H., Kopeikina, K. J., Pitstick, R., Sahara, N., Ashe, K. H., Carlson, G. A., et al. (2012). Propagation of tau pathology in a model of early alzheimer's disease. *Neuron*, 73(4):685–697.
- de Toledo-Morrell, L., Dickerson, B., Sullivan, M. P., Spanovic, C., Wilson, R., and Bennett, D. A. (2000). Hemispheric differences in hippocampal volume predict verbal and spatial memory performance in patients with Alzheimer's disease. *Hippocampus*, 10(2):136–142.
- Deacon, R. M. J. and Rawlins, J. N. P. (2006). T-maze alternation in the rodent : Abstract : Nature Protocols. *Nat. Protocols*, 1(1):7–12.
- Delbeuck, X., Van der Linden, M., and Collette, F. (2003). Alzheimer's disease as a disconnection syndrome? *Neuropsychology Review*, 13(2):79–92.
- Destexhe, A. and Bedard, C. (2013). Local field potential. *Scholarpedia*, 8(8):10713. revision #137113.
- Drzezga, A., Grimmer, T., Henriksen, G., Mühlau, M., Perneczky, R., Miederer, I., Praus, C., Sorg, C., Wohlschläger, A., Riemenschneider, M., Wester, H. J., Foerstl, H., Schwaiger, M., and Kurz, A. (2009). Effect of apoe genotype on amyloid plaque load and gray matter volume in alzheimer disease. *Neurology*, 72(17):1487–1494.

- Dumoulin, S. O. and Wandell, B. A. (2008). Population receptive field estimates in human visual cortex. *NeuroImage*, 39(2):647 – 660.
- Enroth-Cugell, C. and Robson, J. G. (1966). The contrast sensitivity of retinal ganglion cells of the cat. *The Journal of Physiology*, 187(3):517–552.
- Frost, B., Götz, J., and Feany, M. B. (2015). Connecting the dots between tau dysfunction and neurodegeneration. *Trends Cell Biol*, 25(1):46–53.
- Fuhrmann, F., Justus, D., Sosulina, L., Kaneko, H., Beutel, T., Friedrichs, D., Schoch, S., Schwarz, M., Fuhrmann, M., and Remy, S. (2015). Locomotion, theta oscillations, and the speed-correlated firing of hippocampal neurons are controlled by a medial septal glutamatergic circuit. *Neuron*, 86(5):1253 – 1264.
- Gelman, S., Palma, J., Tombaugh, G., and Ghavami, A. (2017). Differences in synaptic dysfunction between rtg4510 and app/ps1 mouse models of alzheimer’s disease. *J Alzheimers Dis*, 61(1):195–208.
- Gerlai, R. (1998). A new continuous alternation task in T-maze detects hippocampal dysfunction in mice: A strain comparison and lesion study. *Behavioural Brain Research*, 95(1):91–101.
- Giannakopoulos, P., Herrmann, F. R., Bussière, T., Bouras, C., Kövari, E., Perl, D. P., Morrison, J. H., Gold, G., and Hof, P. R. (2003). Tangle and neuron numbers, but not amyloid load, predict cognitive status in alzheimer’s disease. *Neurology*, 60(9):1495–1500.
- Grienberger, C., Rochefort, N. L., Adelsberger, H., Henning, H. A., Hill, D. N., Reichwald, J., Staufenbiel, M., and Konnerth, A. (2012). Staged decline of neuronal function in vivo in an animal model of Alzheimer’s disease. *Nature Communications*, 3:774.
- Grundke-Iqbal, I., Iqbal, K., Tung, Y. C., Quinlan, M., Wisniewski, H. M., and Binder, L. I. (1986). Abnormal phosphorylation of the microtubule-associated

- protein tau (tau) in alzheimer cytoskeletal pathology. *Proc Natl Acad Sci U S A*, 83(13):4913–4917.
- Haass, C. and Selkoe, D. J. (2007). Soluble protein oligomers in neurodegeneration: lessons from the Alzheimer's amyloid β -peptide. *Nature Reviews Molecular Cell Biology*, 8(2):101–112.
- Hall, A. M. and Roberson, E. D. (2012). Mouse models of alzheimer's disease. *Brain Research Bulletin*, 88(1):3 – 12. Genetically Engineered Mouse Models of Neurologic Diseases.
- Hardy, J. and Selkoe, D. J. (2002). The Amyloid Hypothesis of Alzheimer's Disease: Progress and Problems on the Road to Therapeutics. *Science*, 297(5580):353–356.
- Harris, K. D. and Shepherd, G. M. G. (2015). The neocortical circuit: themes and variations. *Nature Neuroscience*, 18:170 EP –.
- Hartman, R. E., Izumi, Y., Bales, K. R., Paul, S. M., Wozniak, D. F., and Holtzman, D. M. (2005). Treatment with an amyloid- antibody ameliorates plaque load, learning deficits, and hippocampal long-term potentiation in a mouse model of alzheimer's disease. *Journal of Neuroscience*, 25(26):6213–6220.
- Harvey, C. D., Collman, F., Dombeck, D. A., and Tank, D. W. (2009). Intracellular dynamics of hippocampal place cells during virtual navigation. *Nature*, 461(7266):941–946.
- Hofer, S. B., Ko, H., Pichler, B., Vogelstein, J., Ros, H., Zeng, H., Lein, E., Lesica, N. A., and Mrsic-Flogel, T. D. (2011). Differential connectivity and response dynamics of excitatory and inhibitory neurons in visual cortex. *Nature Neuroscience*, 14:1045 EP –.
- Hoover, B. R., Reed, M. N., Su, J., Penrod, R. D., Kotilinek, L. A., Grant, M. K., Pitstick, R., Carlson, G. A., Lanier, L. M., Yuan, L.-L., Ashe, K. H., and Liao,

- D. (2010). Tau mislocalization to dendritic spines mediates synaptic dysfunction independently of neurodegeneration. *Neuron*, 68(6):1067 – 1081.
- Hort, J., Laczó, J., Vyhnálek, M., Bojar, M., Bureš, J., and Vlček, K. (2007). Spatial navigation deficit in amnesic mild cognitive impairment. *Proceedings of the National Academy of Sciences*, 104(10):4042–4047.
- Huang, X., Yee, B., Nag, S., Chan, S., and Tang, F. (2003). Behavioral and neurochemical characterization of transgenic mice carrying the human presenilin-1 gene with or without the leucine-to-proline mutation at codon 235. *Experimental Neurology*, 183(2):673 – 681.
- Hubel, D. H. and Wiesel, T. N. (1962). Receptive fields, binocular interaction and functional architecture in the cat's visual cortex. *The Journal of Physiology*, 160(1):106–154.
- Hubel, D. H. and Wiesel, T. N. (1968). Receptive fields and functional architecture of monkey striate cortex. *The Journal of Physiology*, 195(1):215–243.
- Huber, C. M., Yee, C., May, T., Dhanala, A., and Mitchell, C. S. (2018). Cognitive decline in preclinical alzheimers disease: amyloid-beta versus tauopathy. *Journal of Alzheimer's Disease*, 61(1):265–281.
- Hunsaker, M. R. and Kesner, R. P. (2018). Unfolding the cognitive map: The role of hippocampal and extra-hippocampal substrates based on a systems analysis of spatial processing. *Neurobiology of learning and memory*, 147:90–119.
- Jack, C. R., Petersen, R. C., Xu, Y. C., O'Brien, P. C., Smith, G. E., Ivnik, R. J., Boeve, B. F., Waring, S. C., Tangalos, E. G., and Kokmen, E. (1999). Prediction of AD with MRI-based hippocampal volume in mild cognitive impairment. *Neurology*, 52(7):1397–1397.
- Jack, C. R. J., Knopman, D. S., Jagust, W. J., Petersen, R. C., Weiner, M. W., Aisen, P. S., Shaw, L. M., Vemuri, P., Wiste, H. J., Weigand, S. D., Lesnick, T. G.,

- Pankratz, V. S., Donohue, M. C., and Trojanowski, J. Q. (2013). Tracking pathophysiological processes in alzheimer's disease: an updated hypothetical model of dynamic biomarkers. *Lancet Neurol*, 12(2):207–216.
- Jack, C. R. J., Knopman, D. S., Jagust, W. J., Shaw, L. M., Aisen, P. S., Weiner, M. W., Petersen, R. C., and Trojanowski, J. Q. (2010). Hypothetical model of dynamic biomarkers of the alzheimer's pathological cascade. *Lancet Neurol*, 9(1):119–128.
- Jackson, J. S., Witton, J., Johnson, J. D., Ahmed, Z., Ward, M., Randall, A. D., Hutton, M. L., Isaac, J. T., O'Neill, M. J., and Ashby, M. C. (2017). Altered synapse stability in the early stages of tauopathy. *Cell Reports*, 18(13):3063 – 3068.
- Jadhav, S. P., Kemere, C., German, P. W., and Frank, L. M. (2012). Awake hippocampal sharp-wave ripples support spatial memory. *Science*, 336(6087):1454–1458.
- Kang, J., Lemaire, H.-G., Unterbeck, A., Salbaum, J. M., Masters, C. L., Grzeschik, K.-H., Multhaup, G., Beyreuther, K., and Müller-Hill, B. (1987). The precursor of alzheimer's disease amyloid a4 protein resembles a cell-surface receptor. *Nature*, 325(6106):733.
- Karl, T., Bhatia, S., Cheng, D., Kim, W. S., and Garner, B. (2012). Cognitive phenotyping of amyloid precursor protein transgenic j20 mice. *Behavioural Brain Research*, 228(2):392 – 397.
- Kerlin, A. M., Andermann, M. L., Berezovskii, V. K., and Reid, R. C. (2010). Broadly tuned response properties of diverse inhibitory neuron subtypes in mouse visual cortex. *Neuron*, 67(5):858 – 871.
- Kohn, A. and Movshon, J. A. (2004). Adaptation changes the direction tuning of macaque mt neurons. *Nature Neuroscience*, 7:764 EP –.

- Kopeikina, K. J., Polydoro, M., Tai, H.-C., Yaeger, E., Carlson, G. A., Pitstick, R., Hyman, B. T., and Spires-Jones, T. L. (2012). Synaptic alterations in the rtg4510 mouse model of tauopathy. *Journal of Comparative Neurology*, 521(6):1334–1353.
- Krantic, S. and Torriglia, A. (2014). Retina: source of the earliest biomarkers for Alzheimer's disease? *Journal of Alzheimer's Disease*, 40(2):237–243.
- Kuchibhotla, K. V., Wegmann, S., Kopeikina, K. J., Hawkes, J., Rudinskiy, N., Andermann, M. L., Spires-Jones, T. L., Bacskai, B. J., and Hyman, B. T. (2014). Neurofibrillary tangle-bearing neurons are functionally integrated in cortical circuits in vivo. *Proceedings of the National Academy of Sciences*, 111(1):510–514.
- Kunz, L., Schröder, T. N., Lee, H., Montag, C., Lachmann, B., Sariyska, R., Reuter, M., Stirnberg, R., Stöcker, T., Messing-Floeter, P. C., Fell, J., Doeller, C. F., and Axmacher, N. (2015a). Reduced grid-cell-like representations in adults at genetic risk for alzheimer's disease. *Science*, 350(6259):430–433.
- Kunz, L., Schröder, T. N., Lee, H., Montag, C., Lachmann, B., Sariyska, R., Reuter, M., Stirnberg, R., Stöcker, T., Messing-Floeter, P. C., Fell, J., Doeller, C. F., and Axmacher, N. (2015b). Reduced grid-cell-like representations in adults at genetic risk for Alzheimer's disease. *Science*, 350(6259):430–433.
- Laakso, M. P., Soininen, H., Partanen, K., Helkala, E.-L., Hartikainen, P., Vainio, P., Hallikainen, M., Hänninen, T., and Sr, P. J. R. (1995). Volumes of hippocampus, amygdala and frontal lobes in the MRI-based diagnosis of early Alzheimer's disease: Correlation with memory functions. *Journal of Neural Transmission - Parkinson's Disease and Dementia Section*, 9(1):73–86.
- Laczó, J., Vlček, K., Vyhnálek, M., Vajnerová, O., Ort, M., Holmerová, I., Tolar, M., Andel, R., Bojar, M., and Hort, J. (2009). Spatial navigation testing discriminates two types of amnesic mild cognitive impairment. *Behavioural Brain Research*, 202(2):252–259.

- Lalonde, R. (2002). The neurobiological basis of spontaneous alternation. *Neuroscience Biobehavioral Reviews*, 26(1):91 – 104.
- Lambert, J.-C., Ibrahim-Verbaas, C. A., Harold, D., Naj, A. C., Sims, R., Bellenguez, C., Jun, G., DeStefano, A. L., Bis, J. C., Beecham, G. W., et al. (2013). Meta-analysis of 74,046 individuals identifies 11 new susceptibility loci for alzheimer's disease. *Nature genetics*, 45(12):1452.
- Larson, J., Lynch, G., Games, D., and Seubert, P. (1999). Alterations in synaptic transmission and long-term potentiation in hippocampal slices from young and aged pdapp mice. *Brain research*, 840(1-2):23–35.
- Lewis, D. A., Campbell, M. J., Terry, R. D., and Morrison, J. H. (1987). Laminar and regional distributions of neurofibrillary tangles and neuritic plaques in Alzheimer's disease: a quantitative study of visual and auditory cortices. *The Journal of Neuroscience*, 7(6):1799–1808.
- Lewis, J., Dickson, D. W., Lin, W.-L., Chisholm, L., Corral, A., Jones, G., Yen, S.-H., Sahara, N., Skipper, L., Yager, D., et al. (2001). Enhanced neurofibrillary degeneration in transgenic mice expressing mutant tau and app. *Science*, 293(5534):1487–1491.
- Lewis, J., McGowan, E., Rockwood, J., Melrose, H., Nacharaju, P., Van Slegtenhorst, M., Gwinn-Hardy, K., Murphy, M. P., Baker, M., Yu, X., et al. (2000). Neurofibrillary tangles, amyotrophy and progressive motor disturbance in mice expressing mutant (p301l) tau protein. *Nature genetics*, 25(4):402.
- Liebscher, S., Keller, G. B., Goltstein, P. M., Bonhoeffer, T., and Hübener, M. (2016). Selective Persistence of Sensorimotor Mismatch Signals in Visual Cortex of Behaving Alzheimer's Disease Mice. *Current Biology*.
- Liu, L., Drouet, V., Wu, J. W., Witter, M. P., Small, S. A., Clelland, C., and Duff, K. (2012). Trans-synaptic spread of tau pathology in vivo. *PloS one*, 7(2):e31302.

- McKhann, G. M., Knopman, D. S., Chertkow, H., Hyman, B. T., Jack Jr., C. R., Kawas, C. H., Klunk, W. E., Koroshetz, W. J., Manly, J. J., Mayeux, R., Mohs, R. C., Morris, J. C., Rossor, M. N., Scheltens, P., Carrillo, M. C., Thies, B., Weintraub, S., and Phelps, C. H. (2011). The diagnosis of dementia due to Alzheimer's disease: Recommendations from the National Institute on Aging-Alzheimer's Association workgroups on diagnostic guidelines for Alzheimer's disease. *Alzheimer's & Dementia*, 7(3):263–269.
- Mehta, D., Jackson, R., Paul, G., Shi, J., and Sabbagh, M. (2017). Why do trials for alzheimers disease drugs keep failing? a discontinued drug perspective for 2010-2015. *Expert opinion on investigational drugs*, 26(6):735–739.
- Menkes-Caspi, N., Yamin, H. G., Kellner, V., Spires-Jones, T. L., Cohen, D., and Stern, E. A. (2015). Pathological tau disrupts ongoing network activity. *Neuron*, 85(5):959 – 966.
- Mitra, P. (2007). *Observed Brain Dynamics*. Oxford University Press.
- Mondragn-Rodriguez, S., Basurto-Islas, G., Santa-Maria, I., Mena, R., Binder, L. I., Avila, J., Smith, M. A., Perry, G., and Garca-Sierra, F. (2008). Cleavage and conformational changes of tau protein follow phosphorylation during alzheimers disease. *International Journal of Experimental Pathology*, 89(2):81–90.
- Morris, J. C., Roe, C. M., Xiong, C., Fagan, A. M., Goate, A. M., Holtzman, D. M., and Mintun, M. A. (2010). Apoe predicts amyloid-beta but not tau alzheimer pathology in cognitively normal aging. *Annals of Neurology*, 67(1):122–131.
- Mucke, L., Masliah, E., Yu, G. Q., Mallory, M., Rockenstein, E. M., Tatsuno, G., Hu, K., Kholodenko, D., Johnson-Wood, K., and McConlogue, L. (2000). High-level neuronal expression of abeta 1-42 in wild-type human amyloid protein precursor transgenic mice: synaptotoxicity without plaque formation. *Journal of Neuroscience*, 20(11):4050–4058.
- Mullan, M., Crawford, F., Axelman, K., Houlden, H., Lilius, L., Winblad, B., and

- Lannfelt, L. (1992). A pathogenic mutation for probable alzheimer's disease in the app gene at the n-terminus of β -amyloid. *Nature genetics*, 1(5):345.
- Murrell, J., Farlow, M., Ghetti, B., and Benson, M. D. (1991). A mutation in the amyloid precursor protein associated with hereditary alzheimer's disease. *Science*, 254(5028):97–99.
- Naka, K. I. and Rushton, W. A. H. (1966). S-potentials from luminosity units in the retina of fish (cyprinidae). *The Journal of Physiology*, 185(3):587–599.
- Nedelska, Z., Andel, R., Lacz , J., Vlcek, K., Horinek, D., Lisy, J., Sheardova, K., Bure , J., and Hort, J. (2012). Spatial navigation impairment is proportional to right hippocampal volume. *Proceedings of the National Academy of Sciences*, 109(7):2590–2594.
- Niell, C. M. and Stryker, M. P. (2008). Highly Selective Receptive Fields in Mouse Visual Cortex. *The Journal of Neuroscience*, 28(30):7520–7536.
- Niell, C. M. and Stryker, M. P. (2010). Modulation of visual responses by behavioral state in mouse visual cortex. *Neuron*, 65(4):472–479.
- Nienborg, H., Hasenstaub, A., Nauhaus, I., Taniguchi, H., Huang, Z. J., and Callaway, E. M. (2013). Contrast dependence and differential contributions from somatostatin- and parvalbumin-expressing neurons to spatial integration in mouse v1. *Journal of Neuroscience*, 33(27):11145–11154.
- Oakley, H., Cole, S. L., Logan, S., Maus, E., Shao, P., Craft, J., Guillozet-Bongaarts, A., Ohno, M., Disterhoft, J., Van Eldik, L., Berry, R., and Vassar, R. (2006). Intra-neuronal -amyloid aggregates, neurodegeneration, and neuron loss in transgenic mice with five familial alzheimer's disease mutations: Potential factors in amyloid plaque formation. *Journal of Neuroscience*, 26(40):10129–10140.
- O'Brien, R. J. and Wong, P. C. (2011). Amyloid precursor protein processing and alzheimer's disease. *Annual review of neuroscience*, 34:185–204.

- Oddo, S., Caccamo, A., Kitazawa, M., Tseng, B. P., and LaFerla, F. M. (2003). Amyloid deposition precedes tangle formation in a triple transgenic model of alzhaimers disease. *Neurobiology of aging*, 24(8):1063–1070.
- Ohki, K. and Reid, R. C. (2007). Specificity and randomness in the visual cortex. *Current opinion in neurobiology*, 17(4):401–407.
- O’Keefe, J. and Dostrovsky, J. (1971). The hippocampus as a spatial map. Preliminary evidence from unit activity in the freely-moving rat. *Brain Research*, 34(1):171–175.
- Olson, M. I. and Shaw, C.-M. (1969). Presenile dementia and alzheimer’s disease in mongolism. *Brain*, 92(1):147–156.
- Olsson, B., Lautner, R., Andreasson, U., hrfelt, A., Portelius, E., Bjerke, M., Hlitt, M., Rosn, C., Olsson, C., Strobel, G., Wu, E., Dakin, K., Petzold, M., Blennow, K., and Zetterberg, H. (2016). Csf and blood biomarkers for the diagnosis of alzheimer’s disease: a systematic review and meta-analysis. *The Lancet Neurology*, 15(7):673 – 684.
- Onslow, A. C. E., Bogacz, R., and Jones, M. W. (2011). Quantifying phase–amplitude coupling in neuronal network oscillations. *Progress in Biophysics and Molecular Biology*, 105(1–2):49–57.
- Palop and Mucke (2009). Epilepsy and cognitive impairments in Alzheimer Disease. *Archives of Neurology*, 66(4):435–440.
- Palop, J. J., Chin, J., Roberson, E. D., Wang, J., Thwin, M. T., Bien-Ly, N., Yoo, J., Ho, K. O., Yu, G.-Q., Kreitzer, A., and others (2007). Aberrant excitatory neuronal activity and compensatory remodeling of inhibitory hippocampal circuits in mouse models of Alzheimer’s disease. *Neuron*, 55(5):697–711.
- Palop, J. J., Jones, B., Kekoni, L., Chin, J., Yu, G.-Q., Raber, J., Masliah, E., and Mucke, L. (2003). Neuronal depletion of calcium-dependent proteins in the dentate gyrus is tightly linked to Alzheimer’s disease-related cognitive deficits.

- Proceedings of the National Academy of Sciences of the United States of America*, 100(16):9572–9577.
- Palop, J. J. and Mucke, L. (2010). Amyloid-[beta]-induced neuronal dysfunction in Alzheimer's disease: from synapses toward neural networks. *Nature neuroscience*, 13(7):812–818.
- Paquet, C., Boissonnot, M., Roger, F., Dighiero, P., Gil, R., and Hugon, J. (2007). Abnormal retinal thickness in patients with mild cognitive impairment and Alzheimer's disease. *Neuroscience Letters*, 420(2):97–99.
- Pettersen, K. H., Devor, A., Ulbert, I., Dale, A. M., and Einevoll, G. T. (2006). Current-source density estimation based on inversion of electrostatic forward solution: Effects of finite extent of neuronal activity and conductivity discontinuities. *Journal of Neuroscience Methods*, 154(1):116 – 133.
- Polich, J., Ladish, C., and Bloom, F. E. (1990). P300 assessment of early alzheimer's disease. *Clinical Neurophysiology*, 77(3):179–189.
- Ramirez, J. J. and Stein, D. G. (1984). Sparing and recovery of spatial alternation performance after entorhinal cortex lesions in rats. *Behavioural Brain Research*, 13(1):53 – 61.
- Ramsden, M., Kotilinek, L., Forster, C., Paulson, J., McGowan, E., SantaCruz, K., Guimaraes, A., Yue, M., Lewis, J., Carlson, G., Hutton, M., and Ashe, K. H. (2005). Age-dependent neurofibrillary tangle formation, neuron loss, and memory impairment in a mouse model of human tauopathy (p301l). *Journal of Neuroscience*, 25(46):10637–10647.
- Ravassard, P., Kees, A., Willers, B., Ho, D., Aharoni, D., Cushman, J., Aghajan, Z. M., and Mehta, M. R. (2013). Multisensory control of hippocampal spatiotemporal selectivity. *Science*, 340(6138):1342–1346.
- Reisel, D., Bannerman, D. M., Schmitt, W. B., Deacon, R. M. J., Flint, J., Borchardt,

- T., Seeburg, P. H., and Rawlins, J. N. P. (2002). Spatial memory dissociations in mice lacking GluR1. *Nature Neuroscience*, 5(9):868–873.
- Roberson, E. D., Halabisky, B., Yoo, J. W., Yao, J., Chin, J., Yan, F., Wu, T., Hamto, P., Devidze, N., Yu, G.-Q., and others (2011). Amyloid- β /Fyn-induced synaptic, network, and cognitive impairments depend on tau levels in multiple mouse models of Alzheimer's disease. *The Journal of Neuroscience*, 31(2):700–711.
- Saganich, M. J., Schroeder, B. E., Galvan, V., Bredesen, D. E., Koo, E. H., and Heinemann, S. F. (2006). Deficits in synaptic transmission and learning in amyloid precursor protein (app) transgenic mice require c-terminal cleavage of app. *Journal of Neuroscience*, 26(52):13428–13436.
- Saleem, A. B., Ayaz, A., Jeffery, K. J., Harris, K. D., and Carandini, M. (2013). Integration of visual motion and locomotion in mouse visual cortex. *Nature Neuroscience*, 16(12):1864–1869.
- Saleem, A. B., Diamanti, E. M., Fournier, J., Harris, K. D., and Carandini, M. (2018). Coherent encoding of subjective spatial position in visual cortex and hippocampus. *Nature*, 562(7725):124–127.
- Saleem, A. B., Lien, A. D., Krumin, M., Haider, B., Rosón, M. R., Ayaz, A., Reinhold, K., Busse, L., Carandini, M., and Harris, K. D. (2017). Subcortical source and modulation of the narrowband gamma oscillation in mouse visual cortex. *Neuron*, 93(2):315 – 322.
- SantaCruz, K., Lewis, J., Spires, T., Paulson, J., Kotilinek, L., Ingelsson, M., Guimaraes, A., DeTure, M., Ramsden, M., McGowan, E., Forster, C., Yue, M., Orne, J., Janus, C., Mariash, A., Kuskowski, M., Hyman, B., Hutton, M., and Ashe, K. H. (2005). Tau suppression in a neurodegenerative mouse model improves memory function. *Science*, 309(5733):476–481.
- Savonenko, A., Xu, G. M., Melnikova, T., Morton, J. L., Gonzales, V., Wong, M. P., Price, D. L., Tang, F., Markowska, A. L., and Borchelt, D. R. (2005). Episodic-

- like memory deficits in the appsw/ps1de9 mouse model of alzheimer's disease: Relationships to -amyloid deposition and neurotransmitter abnormalities. *Neurobiology of Disease*, 18(3):602 – 617.
- Scheff, S. W., Price, D. A., Schmitt, F. A., DeKosky, S. T., and Mufson, E. J. (2007). Synaptic alterations in cal in mild alzheimer disease and mild cognitive impairment. *Neurology*, 68(18):1501–1508.
- Scheuner, D., Eckman, C., Jensen, M., Song, X., Citron, M., Suzuki, N., Bird, T., Hardy, J., Hutton, M., Kukull, W., et al. (1996). Secreted amyloid β -protein similar to that in the senile plaques of alzheimer's disease is increased in vivo by the presenilin 1 and 2 and app mutations linked to familial alzheimer's disease. *Nature medicine*, 2(8):864.
- Scott, L., Kiss, T., Kawabe, T. T., and Hajós, M. (2016). Neuronal network activity in the hippocampus of tau transgenic (tg4510) mice. *Neurobiology of Aging*, 37:66 – 73.
- Scoville, W. B. and Milner, B. (1957). Loss of recent memory after bilateral hippocampal lesions. *Journal of neurology, neurosurgery, and psychiatry*, 20(1):11.
- Seabrook, T. A., Burbridge, T. J., Crair, M. C., and Huberman, A. D. (2017). Architecture, function, and assembly of the mouse visual system. *Annual review of neuroscience*, 40:499–538.
- Self, M. W., Lorteije, J. A., Vangeneugden, J., van Beest, E. H., Grigore, M. E., Lev-elt, C. N., Heimel, J. A., and Roelfsema, P. R. (2014). Orientation-tuned surround suppression in mouse visual cortex. *Journal of Neuroscience*, 34(28):9290–9304.
- Selkoe, D. J. (2002). Alzheimer's Disease Is a Synaptic Failure. *Science*, 298(5594):789–791.
- Shankar, G. M., Leissring, M. A., Adame, A., Sun, X., Spooner, E., Masliah, E., Selkoe, D. J., Lemere, C. A., and Walsh, D. M. (2009). Biochemical and immunohistochemical analysis of an Alzheimer's disease mouse model reveals the

- presence of multiple cerebral A β assembly forms throughout life. *Neurobiology of Disease*, 36(2):293–302.
- Shankar, G. M., Li, S., Mehta, T. H., Garcia-Munoz, A., Shepardson, N. E., Smith, I., Brett, F. M., Farrell, M. A., Rowan, M. J., Lemere, C. A., Regan, C. M., Walsh, D. M., Sabatini, B. L., and Selkoe, D. J. (2008). Amyloid- β protein dimers isolated directly from Alzheimer's brains impair synaptic plasticity and memory. *Nature Medicine*, 14(8):837–842.
- Sigurdsson, T., Stark, K. L., Karayiorgou, M., Gogos, J. A., and Gordon, J. A. (2010). Impaired hippocampal–prefrontal synchrony in a genetic mouse model of schizophrenia. *Nature*, 464(7289):763–767.
- Skaggs, W. E., McNaughton, B. L., Gothard, K. M., and Markus, E. J. (1993). An information-theoretic approach to deciphering the hippocampal code. In *In. Citeseer*.
- Solomon, S. and Kohn, A. (2014). Moving sensory adaptation beyond suppressive effects in single neurons. *Current Biology*, 24(20):R1012 – R1022.
- Spires, T. L., Orne, J. D., SantaCruz, K., Pitstick, R., Carlson, G. A., Ashe, K. H., and Hyman, B. T. (2006). Region-specific dissociation of neuronal loss and neurofibrillary pathology in a mouse model of tauopathy. *The American Journal of Pathology*, 168(5):1598–1607.
- Stewart, S., Cacucci, F., and Lever, C. (2011). Which memory task for my mouse? A systematic review of spatial memory performance in the Tg2576 Alzheimer's mouse model. *Journal of Alzheimer's disease: JAD*, 26(1):105–126.
- Stothart, G., Kazanina, N., Näätänen, R., Haworth, J., and Tales, A. (2015). Early visual evoked potentials and mismatch negativity in alzheimer's disease and mild cognitive impairment. *Journal of Alzheimer's Disease*, 44(2):397–408.
- Strittmatter, W. J., Saunders, A. M., Schmechel, D., Pericak-Vance, M., Enghild, J., Salvesen, G. S., and Roses, A. D. (1993). Apolipoprotein e: high-avidity

- binding to beta-amyloid and increased frequency of type 4 allele in late-onset familial alzheimer disease. *Proceedings of the National Academy of Sciences*, 90(5):1977–1981.
- Sullivan, D., Csicsvari, J., Mizuseki, K., Montgomery, S., Diba, K., and Buzsáki, G. (2011). Relationships between hippocampal sharp waves, ripples, and fast gamma oscillation: Influence of dentate and entorhinal cortical activity. *Journal of Neuroscience*, 31(23):8605–8616.
- Tamaoka, A., Odaka, A., Ishibashi, Y., Usami, M., Sahara, N., Suzuki, N., Nukina, N., Mizusawa, H., Shoji, S., and Kanazawa, I. (1994). App717 missense mutation affects the ratio of amyloid beta protein species (a beta 1-42/43 and a beta 1-40) in familial alzheimer’s disease brain. *Journal of Biological Chemistry*, 269(52):32721–32724.
- The National Institute on Aging and Reagan Institute Working Group on Diagnostic Criteria for the Neuropathological Assessment of Alzheimer’s Disease (1997). Consensus Recommendations for the Postmortem Diagnosis of Alzheimer’s Disease. *Neurobiology of Aging*, 18(4, Supplement 1):S1–S2.
- Uhlhaas, P. J. and Singer, W. (2006). Neural Synchrony in Brain Disorders: Relevance for Cognitive Dysfunctions and Pathophysiology. *Neuron*, 52(1):155–168.
- Van Dam, D., D’Hooge, R., Staufenbiel, M., Van Ginneken, C., Van Meir, F., and De Deyn, P. P. (2003). Age-dependent cognitive decline in the app23 model precedes amyloid deposition. *European Journal of Neuroscience*, 17(2):388–396.
- Van den Bergh, G., Zhang, B., Arckens, L., and Chino, Y. M. (2010). Receptive-field properties of v1 and v2 neurons in mice and macaque monkeys. *Journal of Comparative Neurology*, 518(11):2051–2070.
- Vanderwolf, C. (1969). Hippocampal electrical activity and voluntary movement in the rat. *Electroencephalography and Clinical Neurophysiology*, 26(4):407 – 418.

- Verret, L., Mann, E. O., Hang, G. B., Barth, A. M. I., Cobos, I., Ho, K., Devidze, N., Masliah, E., Kreitzer, A. C., Mody, I., Mucke, L., and Palop, J. J. (2012). Inhibitory Interneuron Deficit Links Altered Network Activity and Cognitive Dysfunction in Alzheimer Model. *Cell*, 149(3):708–721.
- Wang, X., Zhang, C., Szábo, G., and Sun, Q.-Q. (2013). Distribution of camkii expression in the brain in vivo, studied by camkii-gfp mice. *Brain Research*, 1518:9 – 25.
- Weingarten, M. D., Lockwood, A. H., Hwo, S. Y., and Kirschner, M. W. (1975). A protein factor essential for microtubule assembly. *Proc Natl Acad Sci U S A*, 72(5):1858–1862.
- Witton, J., Staniaszek, L. E., Bartsch, U., Randall, A. D., Jones, M. W., and Brown, J. T. (2014). Disrupted hippocampal sharp-wave ripple-associated spike dynamics in a transgenic mouse model of dementia. *The Journal of Physiology*, 594(16):4615–4630.
- Wright, A. L., Zinn, R., Hohensinn, B., Konen, L. M., Beynon, S. B., Tan, R. P., Clark, I. A., Abdipranoto, A., and Vissel, B. (2013). Neuroinflammation and neuronal loss precede a plaque deposition in the happ-j20 mouse model of alzheimers disease. *PLOS ONE*, 8(4):1–14.
- Wszolek, Z. K., Tsuboi, Y., Ghetti, B., Pickering-Brown, S., Baba, Y., and Cheshire, W. P. (2006). Frontotemporal dementia and parkinsonism linked to chromosome 17 (ftdp-17). *Orphanet Journal of Rare Diseases*, 1(1):30.
- Wyble, B. P., Hyman, J. M., Rossi, C. A., and Hasselmo, M. E. (2004). Analysis of theta power in hippocampal eeg during bar pressing and running behavior in rats during distinct behavioral contexts. *Hippocampus*, 14(5):662–674.
- Youngstrom, I. A. and Strowbridge, B. W. (2012). Visual landmarks facilitate rodent spatial navigation in virtual reality environments. *Learning & memory (Cold Spring Harbor, N.Y.)*, 19(3):84–90.